INSIGHTS DERIVED FROM STUDIES ON THE INTERACTION OF WALL JETS WITH AN ELEVATED HUMP WAKE

by

Sean M. Sehman

A thesis submitted to the faculty of
The University of North Carolina at Charlotte
in partial fulfillment of the requirements
for the degree of Master of Science in
Mechanical Engineering

Charlotte

2020

Approved by:

_____
Dr. Mesbah Uddin

_____
Dr. Russell Keanini

_____
Dr. Jun Xu

ABSTRACT

SEAN M. SEHMAN. Insights Derived from Studies on the Interaction of Wall Jets with an Elevated Hump Wake (Under the Direction of DR. MESBAH UDDIN)

Underneath a travelling road vehicle, a channel flow develops between the road and the undertray. This channel flow discharges behind the vehicle as a wall jet. Additionally, flow over the top of the vehicle almost always separates at some point along the body, creating a separated-flow region over and a wake region behind the vehicle, with which the underbody wall jet interacts. While this is a well-known flow configuration, the effects of varying wall jet parameters on the configuration have yet to be studied. This work employs Computational Fluid Dynamics (CFD) to model a traveling vehicle as a simple canonical flow, referred to herein as the wall-jet hump-wake, incorporating a wall jet discharging under the NASA hump wake. These wall-jet hump-wake simulations will be carried out in 2D using Reynolds-Averaged Navier-Stokes (RANS) turbulence modeling approaches. In order to accurately model the flow, validation case studies are carried out for a wall jet, a wall jet in a co-flowing stream, and the NASA hump wake based on previously published experimental works. Based on these validation case studies, a best fit turbulence model is identified, which proves to predict the defining characteristics of each flow to the highest degree of accuracy amongst all other models. The best fit model is then applied to the wall-jet hump-wake flow configuration for a total of nine different cases, each one varying either the wall jet slot height or the wall jet discharge velocity. Results are compiled and compared to shape the defining mean flow and turbulence characteristics of the wall-jet hump-wake. These defining quantities will be compared for the different cases run to determine the effects of wall jet slot height and wall jet discharge velocity on the wake flow. The overall objective of this thesis is to provide a detailed analysis on the interaction of wall jets with

the hump induced wake and resultant drag parameters along the top of the body, in hopes that it will provide insight on the wall jet effects on the wake evolution and overall aerodynamic performance for further works. Results and findings can be later applied to vehicle models to investigate the potential of the readily available wall jet of a vehicle to improve aerodynamic performance.

DEDICATION

To my parents, for all of the strength and support they have given me, which got me to where I am today

To my grandfather, who I hope is looking down to see how far I have followed in his footsteps

ACKNOWLEDGEMENTS

I would like to thank Dr. Mesbah Uddin, my advisor, not only for his help in formulating and completing this thesis, but also for his guidance over the past few years in shaping my career path and his flexibility in helping me juggle my tight school and work schedules. I would also like to thank Spencer Owen for his help early on in showing me the basics of Star CCM+ outside of the classroom and Vincent Lee for providing a second set of eyes when I ran into troubles with this thesis. Finally, I would like to thank my employer and Uncle, Rick Wirth, for his seemingly endless support and flexibility in helping me earn my degree.

TABLE OF CONTENTS

NOMENCLATURE

Symbol	Description	Symbol	Description
x	Streamwise Coordinate	$v+$	Wall-Normal Velocity Scaled by Friction Velocity
y	Wall-Normal Coordinate	$y+$	Wall Distance Scaled by Friction Velocity
t	Time	$-\overline{u_i u_j}$	Reynolds Stresses
U	Streamwise Mean Velocity	$\overline{uv}+uv+$	Reynolds Stresses Scaled by Friction Velocity
V	Wall-Normal Mean Velocity	$u*$	Friction Velocity
u	Streamwise Local Velocity	$Y_{1/2}$	Jet Half-Width
v	Wall-Normal Local Velocity	Re	Reynolds Number
P	Pressure	C_P	Pressure Coefficient
U_{Ref}	Reference Streamwise Velocity	C_f	Skin Friction Coefficient
U_{Inf}, U_∞	Freestream Streamwise Velocity	C_D	Drag Coefficient
P_{Ref}	Reference Pressure	τ_w	Wall Shear Stress
h	Jet Slot Height	ρ	Density
h_b	Baseline Jet Slot Height	ν	Kinematic Viscosity
$h_{splitter}$	Jet/Stream Splitter Plate Thickness	μ	Dynamic Viscosity
c	Chordlength	*Overbar*	Denotes Time Averaged Quantity
U_S	External Stream Velocity	*Subscript i, j*	Tensor notation for x and y components
U_J	Jet Velocity	μ_T	Turbulent Dynamic Viscosity
$U_{J,b}$	Baseline Jet Velocity	ν_T	Turbulent Dynamic Viscosity

Symbol	Description	Symbol	Description
$U_{h,max}$	Max Jet Inlet Velocity	k	Kinetic Energy
$u+$	Streamwise Velocity Scaled by Friction Velocity	ε	Dissipation
W	Intermediate Modeling Parameter (Realizable k-ε)	S	Rate of Strain
A_S	Intermediate Modeling Parameter (Realizable k-ε)	B_{ij}	Intermediate Modeling Parameter (k-ε with Elliptic Blending)
φ	Intermediate Modeling Parameter (Realizable k-ε)	ω	Specific Dissipation
$U^{(*)}$	Intermediate Modeling Parameter (Realizable k-ε)	Ω	Rate of Rotation
R_{ij}, $R_{ii,}$ R_{jj}.	Reynolds Stresses (Tensor Notation)	F_1	Blending Function
$\overline{v}^2$	Time-Averaged Normal Reynolds Stresses	F_2	Blending Function
kf	pressure strain term	$CD_{k\omega}$	Intermediate Modeling Parameter (SST)
∇	Del Operator	γ	Turbulence Intermittency
L	Turbulent Length Scale (V^2F k-ε)	P_γ	Transition Source Term
f	Elliptic Relaxation Term	E_γ	Relaminarization Source Term
T	Turbulent Time Scale (V^2F k-ε)	F_{onset1}	Trigger Function
P_k	Turbulent Energy Production	F_{onset2}	Trigger Function
ϕ_{ii}	Wall-Normal Pressure Strain	F_{onset3}	Trigger Function
ε_{ii}	Wall-Normal Dissipation	F_{onset}	Trigger Function
ϕ_{ij}^*	Redistribution Term	F_{turb}	Trigger Function
n	Wall-Normal Unit Vector	R_T	Modeling Parameter (γ Transition)

Symbol	Description	Symbol	Description
Φ_{ij}^{w}	Redistribution Term (Near Wall)	Re_v	Vorticity Reynolds Number
Φ_{ij}^{h}	Redistribution Term (Away From Wall)	$Re_{\theta c}$	Critical Reynolds Number
A	Lumley's Flatness Parameter	Tu_L	Local Turbulence Intensity
δ	Boundary Layer Thickness	$\lambda_{\theta L}$	Pressure Gradient Parameter

LIST OF TABLES

LIST OF FIGURES

CHAPTER 1: INTRODUCTION

Due to the many unknowns and technological constraints in the field of turbulence, predicting turbulent flow is currently a challenging process in which many steps must be taken to achieve acceptable results. However, a certain framework has been laid out for current researchers. A large part of this framework consists of starting from a simple flow configuration, or canonical flow, and building upon the fundamental characteristics of the simple configuration all the way down to predicting realistic and complex flow. This is especially relevant when turbulence prediction is carried out via simulation rather than experiment, as the simulation must be well developed to provide accurate results and generally becomes more constrained as the simulation detail grows. A good example of this framework is the 2016 work of Fu et al. [14], who started with a simple wall jet flow to validate and compare various turbulence models and experiment with mesh and simulation setup parameters then used the results to develop and execute simulations of a wall jet flow exerted by a racetrack jet dryer. Within the work presented herein, this framework will be followed in developing a simplified model for a newly defined flow configuration, the wall-jet hump-wake (Figure 1.1).

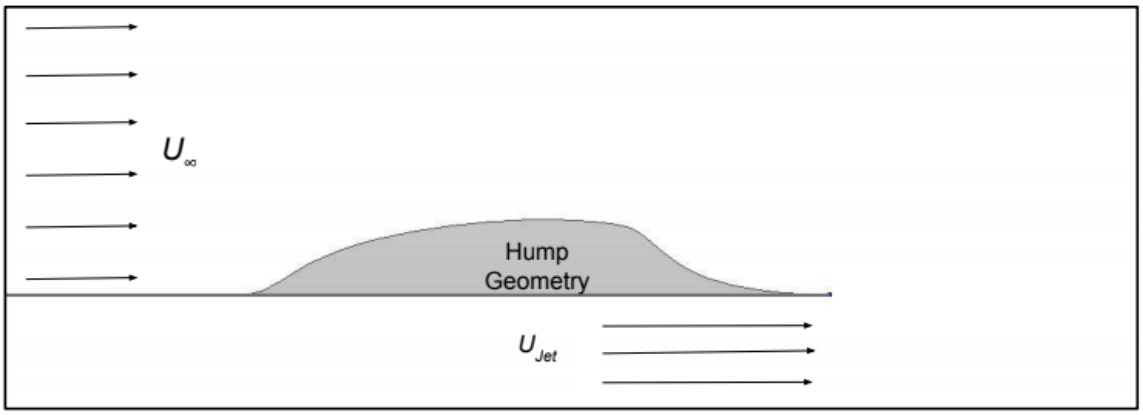

Figure 1.1: Wall-Jet Hump-Wake Flow Configuration

The focus of this thesis is to explore the resultant flow obtained when combining a wall jet with an elevated hump wake and an external free stream, as shown in Figure 1.1, where U_∞ (also referred to as U_S) and U_{Jet} represent the free stream and jet velocities, respectively. While the wall-jet hump-wake flow configuration can be found in literature, this work is among the first to explicitly acknowledge and study the flow combination as a canonical flow.

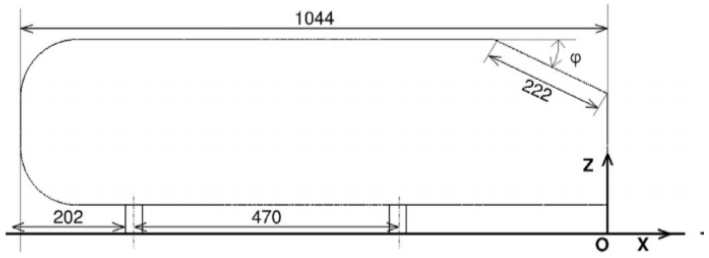

Figure 1.2: Ahmed Vehicle Body Geometry [18]

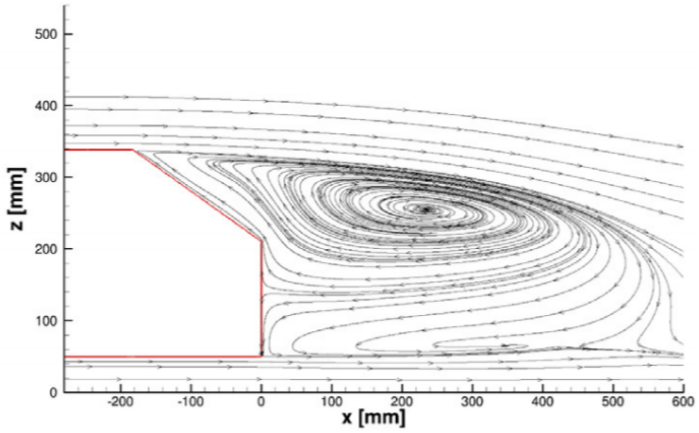

Figure 1.3: Ahmed Vehicle Body Velocity Flow Field at 40 *m/s* [18]

Consider a two-dimensional centerline cut plane of the Ahmed body (Figures 1.2 & 1.3 above). It can be seen here that the streamwise velocity between the underbody of a vehicle and

the road differs from the free stream velocity, forming a wall jet flow exiting from under the rear of the vehicle. The vehicle body in motion creates a wake that interacts with the wall jet at the rear of the vehicle. By understanding and exploring the effect of the wall jet on the vehicle's wake, a new perspective can be obtained for the vehicle model as a whole, and the wall jet may prove to be a useful and available tool for separation control and, in turn, road vehicle aerodynamics.

1.1: The Importance of Canonical Flows

Throughout the history of research and development in the field of turbulence, a dedicated focus has been placed on defining and understanding canonical flows. Canonical flows are specific flow configurations with generic defining characteristics. Examples include wakes, boundary layers, mixing layers, and jets. Canonical flows are basic flow configurations used to explore the fundamental principles governing each classification. For example, while the turbulent jet produced from a vehicle's exhaust gases projecting into the atmosphere is entirely different than the turbulent jet produced from a square HVAC duct entering a room through a vent, the basic principle of a stream of fluid entering an environment via a nozzle (known as a free shear jet) can be used to relate principle flow characteristics of the two. Canonical flows are also combined amongst themselves and with other flow parameters to further refine and model real flows. For example, a turbulent jet can be combined with a boundary layer flow, such as a jet dryer blowing air across the ground as seen in the 2016 work of Fu et al. [14] to create a wall jet. Another example is a turbulent wake generated from a wall mounted hump, as seen in the 2006 work of Greenblatt et al. [16], which combines a wake flow with a boundary layer flow.

In the case of the wall-jet hump-wake, multiple canonical flows are combined to define a new and unique canonical flow. The first layer of this flow is the wall jet. The next layer of the wall-jet hump-wake is the external free stream. Last, a hump induced wake is introduced. The

overall resultant flow can be used as a tool to experiment with the interaction of wall jets with the separation region and the downstream velocity deficit created by a wake.

1.2: Introduction to the Wall-Jet Hump-Wake Flow Configuration

The wall-jet hump-wake is a specific combination of simple flows applicable to real life flow configurations, such as certain wake generating geometries in the vicinity of a wall. The direct interest in studying this flow configuration is to study the interaction of the hump generated wake and the external stream with the underlying wall jet before, at, and beyond the trailing edge of the geometry seen in Figure 1.1 above. The flow configuration is a simple and direct way of representing a traveling vehicle, with the hump wake being generated by the vehicle body and the wall jet being generated by the air channel between the vehicle's body and the driving surface. This representation can be better visualized in Figures 1.2 & 1.3 above. It is seen here that the leading edge geometry of the Ahmed vehicle body centerline splits the incoming flow stream into two parts: a wake flow over the vehicle and a channel flow under the vehicle. Since the most frontward point of the vehicle's geometry is above the lower boundary of the body, part of the incoming flow is funneled under the vehicle, causing the channel flow under the vehicle to accelerate to a higher velocity than that of the external free stream because of the pressure drop of the air as it is constricted (ground effect). At the trailing edge of the vehicle, this channel flow discharges back into the environment as a wall jet, where it interacts with both the external free stream and the vehicle body wake in a wall-jet hump-wake flow configuration. None of this information is new. In fact, an abundance of literature on ground effects can be found (browse [9] and accompanying references for more information).

The novelty in this work is the focus of the wall jet put directly on the recirculation zone and drag contributions due to the recirculation zone. The specific interaction of all three flows has not yet been notably explored in the proposed context. The major question proposed during the

initial stages of this thesis is the effect of the wall jet velocity on the wake. Specifically, the velocity of the wall jet may have significant effects on the downstream distance of flow reattachment in the recirculation zone, as well as significant effects seen upstream along the top of the body. Historically, the typical focus on vehicle aerodynamics with respect to drag reduction has been focused on creating more streamlined vehicle bodies. In turn, a dedicated focus of drag reduction is put on flow separation reduction and control. In regards to the undertray of a vehicle, much focus is on reducing drag due to complex geometries underneath the vehicle. (see [19] for example). Additionally, past work has focused on the channel flow under the vehicle and the flowstream exiting from underneath the vehicle at the rear (See [9]). The proposed work within this thesis also is to focus on flow separation at the rear of the vehicle, but the underlying wall jet will be explored as a potential separation control device, bringing the focus of the recirculation bubble from the top of the vehicle to the undertray.

Since the leading edge and trailing edge geometry of a vehicle can be modified to allow more or less airflow to be funneled into the vehicle underbody resulting in different discharge velocities, the proposed work entailed within this thesis can provide valuable insight into drag reduction and overall aerodynamic improvement of a vehicle's body by tailoring the development of the wall jet in addition to the typical way of modifying the way air flows over a vehicle. The two major characteristics of the wall jet are the slot height and the jet velocity. The slot height is the simpler of the two to modify, as it only requires alteration in the vehicle's ride height. The wall jet velocity is slightly more complicated, but still feasible. The velocity of the discharging jet is largely dependent on the vehicle speed, leading edge geometry, and trailing edge geometry. While vehicle speed is not controllable by the vehicle's geometry, the inlet and outlet geometries of the vehicle's underside channel flow can be modified using principles of ground effects. Thus,

taking into consideration the ability to control the wall jet characteristics of a vehicle, the effects of the wall jet on vehicle aerodynamic performance becomes a valuable study.

1.3: Scope of this Thesis

In order to develop a successful prediction of the wall-jet hump-wake flow, many steps must be taken. The first part of this work will use various RANS (Reynolds-Averaged Navier-Stokes) turbulence models in the commercial Computational Fluid Dynamics (CDF) package STAR-CCM+ to develop flow simulations based on previously published literature for wall jets, wall jets with an external co-flowing stream, and the NASA hump wake. These flow simulations will be set up to match the literature, which will be used as validation cases for each flow, and to refine mesh parameters for the wall jet with and without an external stream and the NASA hump wake until simulation results are satisfactory.

Following the successful simulation of each flow validation case, the various turbulence models used will be compared amongst themselves and against the experimental data in order to determine a best fit model for the wall-jet hump-wake flow configuration. The final wall-jet hump-wake configuration mesh and geometry will be set up using the three validation cases for reference, and multiple simulations are to be run, varying wall jet slot height and discharge velocity.

Various mean flow and turbulence quantities for the wall jet -hump wake will be explored to form an understanding of this configuration. Additionally, the variations in slot height and jet velocity will be compared to each other to form an understanding of each parameter. Finally, a detailed analysis on the formation of the separation bubble as well as the effects of slot height and jet velocity on separation and drag will be conducted.

CHAPTER 2: REVIEW OF LITERATURE

Since the proposed wall-jet hump-wake is a largely unexplored flow configuration, review of literature on this flow is limited. However, in order to study the wall-jet hump-wake, an understanding must be formed of the wall jet with and without an external stream as well as the wake. Thus, a thorough review of literature is to be conducted in this chapter. In addition to a literature review on the three flows that compose the wall-jet hump-wake, a literature review is also in order for the RANS turbulence models selected for the simulations.

2.1: Wall Jets

wall jets are a well documented flow configuration in which a high speed stream of fluid is discharged into an environment along a wall. Two types of wall jets are commonly seen in literature: one in which the jet discharges from a nozzle near a wall and one in which the jet discharges from a slot extending from the wall. With a nozzle wall jet, the fluid does not immediately interact with the wall when entering the environment, allowing for the flow to develop as a free jet for some downstream distance before interacting with the wall. An example of this is the 2005 work of Dejoan and Leschziner [6]. A slot wall jet (see [32]), in contrast, has an immediate boundary layer development at the point where the fluid enters the environment. For this work, the slot jet will be studied, as it more closely resembles the wall jet flow discharged from underneath a moving vehicle.

The wall jet is a combination of a free jet and a boundary layer flow. As a result, the major characteristics of a wall jet can be separated into two regions. Near the wall, the wall jet acts as a boundary layer flow, whereas in the outer layer, the wall jet acts as a free shear jet [24]. Much of the literature available on wall jets is aimed at understanding and quantifying turbulence characteristics relating to them. For example, Eriksson et al. [10] studied the resultant flow fields and turbulence characteristics of a slot type wall jet via experiment. Additionally, Uddin et al.

[41] studied the near field of a turbulent wall jet, investigating the large scale turbulent structures formed. More recent applications, such as the 2016 work of Fu et al [14], begin to direct the focus of wall jets to real applications. In this work, the turbulent wall jet was applied to a jet dryer for a race track.

2.2: Wall Jets in a Co-flowing Stream

Another flow parameter in wall jet flows is the effect of an external stream. With an external stream, the free shear layer of the wall jet can be seen as a mixing layer [3]. In regard to the wall jet's downstream growth, three regions were outlined by Bradshaw and Gee [3]. First, there exists a region where the wall jet velocity profile displays near-true wall jet characteristics, meaning the wall jet velocity is separated into the boundary layer region and the free jet region, with a maximum velocity higher than that of the free stream. In the intermediate region, the wall jet outer layer's velocity excess becomes the same order of the freestream velocity. Last, there exists a region (loosely referred to as a wall-wake by [21]) where a velocity deficit is formed by the wall jet, similar to a simple boundary layer flow over a flat plate.

While this flow configuration has not been studied as much as the simple wall jet in an otherwise quiescent environment, there is still a fair amount of work on the topic. For example, Kacker and Whitelaw [21] experimented with the wall jet and external stream, using different co-flowing stream to jet velocity ratios and different lip to jet thickness ratios (the lip is a small flat plate separating the jet from the co-flowing stream). In this study, different flow features such as resultant velocity flow fields and various turbulence quantities were studied. In 1975, J. Campbell performed significant work to develop a theoretical model for a wall jet issuing into a co-flowing stream [5]. Further on, Ayech et al. developed multiple direct numerical simulations to study the effects of the co-flowing stream as well as effects of Grashof number [2]. More recently, Naqavi and Tucker applied an LES turbulence model to the same wall jet and co-flowing

stream configuration used by Kacker and Whitelaw [21] and studied the coherent turbulent structures in the near field [31].

2.3: The NASA Hump Wake

In general, the major characteristic of any wake is the velocity deficit formed downstream of the wake generator. In the case of a turbulent wake, the velocity deficit is large enough to create separation and recirculation behind the generator.This is a major area of focus in vehicle aerodynamics as well as turbulence studies as a whole, as flow separation is a major contributor to overall drag and reduction of separation is typically desired for the streamlining of a wake generator.

The selected hump geometry for this thesis is the NASA hump (seen in Figure 1.1), which is a modified version of the Glauert-Goldschmied body [16]. This hump was selected both because it has resemblance to a vehicle body and because an immensely large library of literature is available for the geometry.

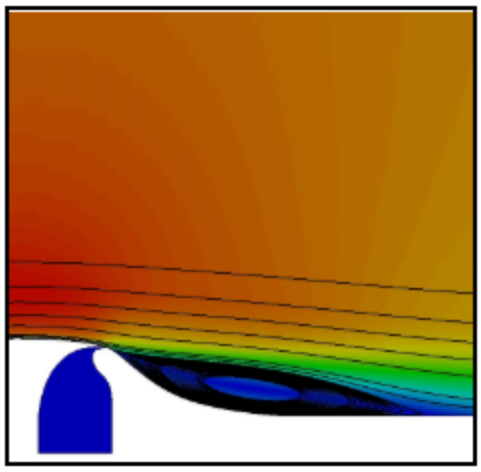

Figure 2.1: NASA Hump Velocity Flow Field [22]

The major focus (see [12], [16], [13], and [26]) of this hump is it's unique ability to create massive flow separation and a large, defined recirculation bubble (seen in F*i*gure 2.1), desirable for studies on flow separation control. While much of the work done on this hump is directed toward separation control via a suction-control plenum located on the aft portion of the geometry, flow characteristics are also available for this hump without the active plenum both within the works noted above and on the NASA CFD Evaluation website [22]. With the hump wake flow configuration, a well defined and simple recirculation bubble is generated, which makes this hump a desirable geometry to use, as it is both simple (having no complex geometric features) and it is able to generate the recirculation zone experienced behind a moving vehicle.

2.4: RANS Turbulence Modeling

For this work, all simulations are carried out with RANS eddy viscosity turbulence models, which only solve for turbulence directly at the integral scales, then model the turbulence for all lower scales using characteristic transport equations to describe the turbulence. The RANS equations can be seen below as Equation (2.1) and Equation (2.2). RANS Turbulence models separate the instantaneous components of the Navier-Stokes Equations into time averaged and fluctuating components, resulting in the last term of (2.2), the Reynolds stresses, which introduce the closure problem. Reynolds stresses can be approximated using the Boussinesq hypothesis (Equation (2.3) below), which closes the RANS equations. To close these equations with two equation models, two turbulence quantities are calculated to describe the turbulence of the flow, and said two quantities are then used to solve for turbulent viscosity, which then allows for Equation (2.3) to be solved.

$$\frac{\partial \overline{U_i}}{\partial x_i} = 0 \tag{2.1}$$

$$\frac{\partial \overline{U_i}}{\partial t} + \overline{U_j}\frac{\partial \overline{U_i}}{\partial x_j} = \frac{1}{\rho}\frac{\partial \bar{p}}{\partial x_i} + \frac{\partial}{\partial x_j}\{\nu(\frac{\partial \overline{U_i}}{\partial x_j} + \frac{\partial \overline{U_j}}{\partial x_i}) - \overline{u_i u_j}\} \tag{2.2}$$

$$-\rho\overline{u_i u_j} = \mu_T(\frac{\partial U}{\partial y} + \frac{\partial V}{\partial x}) \tag{2.3}$$

The major drawback of RANS modeling is undoubtedly the sacrifice of accuracy in turn of computational ease. Thus, some degree of simulation validation must be carried out in order to determine the overall quality of the simulations. A significant part of the validation process is turbulence model selection. There is no best model for turbulent flow prediction, but rather a number of models, all with their own respective strengths and weaknesses. For this thesis, four different validation cases are required before the wall-jet hump-wake can be investigated. Therefore, six models are selected to be applied to each validation case. All models will be compared to each other as well as experimental data for each case, and the overall best fit model or models will be selected for the final wall-jet hump-wake simulations. The forthcoming sections in this chapter are provided as a literature review of each model, presenting a description of each model as well as relevant equations and model constants for each.

2.4.1: The Standard k-ε Turbulence Model

The first model selected in the k-ε turbulence family is the standard k-ε model of Launder and Jones [20]. The two transport terms for this model are kinetic energy and dissipation rate, and the equation for each is can be seen below as Equations (2.4) & (2.5), respectively.

$$\rho u\frac{\partial k}{\partial x} + \rho v\frac{\partial k}{\partial y} = \frac{\partial}{\partial y}[(\mu + \frac{\mu_T}{\sigma_k})\frac{\partial k}{\partial y}] + \mu_T(\frac{\partial u}{\partial y})^2 - \rho\varepsilon - 2\mu(\frac{\partial k}{\partial y})^2 \tag{2.4}$$

$$\rho u\frac{\partial \varepsilon}{\partial x} + \rho v\frac{\partial \varepsilon}{\partial y} = \frac{\partial}{\partial y}[(\mu + \frac{\mu_T}{\sigma_\varepsilon})\frac{\partial \varepsilon}{\partial y}] + C_1\frac{\varepsilon}{k}\mu_T(\frac{\partial u}{\partial y})^2 - C_2\frac{\rho\varepsilon^2}{k} - 2\frac{\mu\mu_T}{\rho}(\frac{\partial^2 u}{\partial y^2})^2 \tag{2.5}$$

The turbulent viscosity is calculated as seen in Equation (2.6) below.

$$\mu_T = C_\mu \rho \frac{k^2}{\varepsilon} \tag{2.6}$$

The model constants, derived empirically, are shown below in Table 2.1.

Table 2.1: Standard k-ε Model Constants [20]

C_μ	C_1	C_2	σ_k	σ_ε
0.09	1.45	2.0	1.0	1.3

2.4.2: The Realizable k-ε Turbulence Model

The second member of the k-ε family selected for this work is the Realizable k-ε model of Shih et al [38] & [37]. The equations for kinetic energy and rate of dissipation are the same as Equations (2.4) & (2.5) for the standard k-ε model. Turbulent viscosity is calculated with Equation (2.6) as well. The major difference of the Realizable k-ε model is that C_μ in Equation (2.6) is not constant, but rather determined using Equation (2.7), which is based on mean strain and rotation rates [35].

$$C_\mu = \frac{1}{A_0 + A_s U^{(*)} \frac{k}{\varepsilon}} \tag{2.7}$$

where

$$U^{(*)} = \sqrt{S_{ij} S_{ij} + (\Omega_{ij} - 2\varepsilon_{ijk}\omega_k)(\Omega_{ij} - 2\varepsilon_{ijk}\omega_k)} \tag{2.8}$$

$$A_S = \sqrt{6}cos(\varphi) \tag{2.9}$$

$$\varphi = \frac{1}{3}arccos(\sqrt{6}W) \tag{2.10}$$

$$W = \frac{S_{ij}S_{jk}S_{ki}}{S_{ij}S_{ij}} \tag{2.11}$$

The term 'realizable' refers to realizability of Reynolds stresses. As opposed to some k-ε models, the Realizable k-ε model ensures real values of Reynolds stresses, which must satisfy three major criteria. First, the normal Reynolds stresses (R_{ii}) must be positive. Second, the Reynolds stress tensor must satisfy the criteria $R_{ij}^2 \geq R_{ii}R_{jj}$. Third, the tensor is to be positive semi-definite [36]. In addition to the added realizability parameters, the model constants are adjusted, as seen in Table 2.2 below.

Table 2.2: Realizable k-ε Model Constants [35]

C_1	C_2	σ_k	σ_ε	A_0
1.44	1.9	1.0	1.2	6.5

2.4.3: The V^2F k-ε Turbulence Model

The V^2F k-ε model of P. Durbin [7] is a boundary layer focused model in the The k-ε family. As with the other models, the equations for turbulent kinetic energy and rate of dissipation are Equations (2.4) & (2.5) above. Additionally, a transport equation for normal Reynolds

stresses, v^2, is introduced (Equation (2.12)), which is used to replace the traditional damping functions near the wall and to account for wall blocking of energy redistribution [25].

$$\frac{D\bar{v}^2}{Dt} = kf - \bar{v}^2\frac{\varepsilon}{k} + \nabla_j[(\nu + \frac{\nu_t}{\sigma_k})\nabla_j\bar{v}^2] \tag{2.12}$$

Here, kf is the pressure strain term, defined as seen in Equation (2.13),

$$kf = \phi_{ii} - \varepsilon_{ii} + \frac{\bar{v}^2}{k}\varepsilon \tag{2.13}$$

where Φ_{ii} and ε_{ii} are normal components of pressure strain and dissipation terms to the wall [25]. An elliptic relaxation equation, Equation (2.14), is used to solve for f,

$$L^2\nabla^2 f - f = \frac{1}{T}(C_1 - 1)[\frac{\bar{v}^2}{k} - \frac{2}{3}] - C_2\frac{P_k}{k} \tag{2.14}$$

where

$$T = max[\frac{k}{\varepsilon}, 6\sqrt{\frac{\nu}{\varepsilon}}] \tag{2.15}$$

$$L = C_L max[\frac{k^{\frac{3}{2}}}{\varepsilon}, C_\eta\frac{\nu^{\frac{3}{4}}}{\varepsilon^{\frac{1}{4}}}] \tag{2.16}$$

Turbulent viscosity is now defined as seen in Equation (2.17).

$$\nu_t = C_\mu\bar{v}^2 T \tag{2.17}$$

The model constants can be seen below in Table 2.3.

Table 2.3: V^2F k-ε Model Constants [25]

C_μ	σ_k	σ_ε	$C_{\varepsilon 1}$	$C_{\varepsilon 2}$	C_1	C_2	C_L	C_μ
0.19	1	1.3	$1.4[1+0.045\sqrt{\frac{k}{\overline{v^2}}}]$	1.9	1.4	0.3	0.3	70

2.4.4: The k-ε Turbulence Model with Elliptic Blending

The k-ε model with elliptic blending [27] was also formulated to focus on the struggles of the standard k-ε model near the wall. This model was formulated to reduce the complexity of Durbin's Reynolds stress model [7]. Here, the transport equations for Reynolds stresses and dissipation rate can be seen below as Equations (2.18) & (2.19), respectively.

$$\frac{D\overline{u_i u_j}}{D_t} = P_{ij} + D_{ij}^T + \Phi_{ij}^* - \varepsilon_{ij} \tag{2.18}$$

$$\frac{D\varepsilon}{Dt} = \frac{C_{\varepsilon 1}P - C_{\varepsilon 2}\varepsilon}{T} + \frac{\partial}{\partial x_j}\left(\frac{C_\mu}{\sigma_\varepsilon}\overline{u_l u_m} T \frac{\partial_\varepsilon}{\partial x_m}\right) + \nu\frac{\partial^2\varepsilon}{\partial x_k \partial x_k} + C_{\varepsilon 3}\nu\frac{k}{\varepsilon}\overline{u_j u_k}\left(\frac{\partial^2 U_i}{\partial x_j \partial x_l}\right)\left(\frac{\partial^2 U_i}{\partial x_k \partial x_l}\right) \tag{2.19}$$

In the two equations above,

$$D_{ij}^T = \frac{\partial}{\partial x_j}\left(\frac{C_\mu}{\sigma_k}\overline{u_l u_m} T \frac{\partial \overline{u_i u_i}}{\partial x_m}\right) \tag{2.20}$$

and the redistribution term is seen below in Equation (2.21).

$$\Phi_{ij}^* = (1 - k\alpha)\Phi_{ij}^w + k\alpha\Phi_{ij}^h \tag{2.21}$$

Dissipation is modeled as

$$\varepsilon_{ij} = (1 - Ak\alpha)\frac{\overline{u_i u_j}}{k}\varepsilon + Ak\alpha\frac{2}{3}\varepsilon\delta_{ij} \tag{2.22}$$

where Lumley's flatness parameter, A, is

$$A = \frac{9}{8}(\alpha_{ij}\alpha_{ij} - \alpha_{ij}\alpha_{jk}\alpha_{ki}) \tag{2.23}$$

$$\alpha_{ij} = \frac{\overline{u_i u_j}}{k} - \frac{2}{3}\delta_{ij} \tag{2.24}$$

The elliptic relaxation model is now

$$\alpha - L^2\nabla^2\alpha = \frac{1}{\varepsilon T} \tag{2.25}$$

$$L = C_L max(\frac{k^{3/2}}{\varepsilon}, C_\eta\frac{\nu^{3/4}}{\varepsilon^{1/4}}) \tag{2.26}$$

$$T = max(\frac{k}{\varepsilon}, C_T(\frac{\nu}{\varepsilon})^{1/2}) \tag{2.27}$$

and the near wall redistribution term is

$$\Phi_{ij}^{w} = -5\frac{\varepsilon}{k}(\overline{u_i u_k}n_j n_k + \overline{u_j u_k}n_i n_k - \frac{1}{2}\overline{u_k u_l}n_k n_l(n_i n_j - \delta_{ij})) \tag{2.28}$$

$$n = \frac{\nabla \alpha}{||\nabla \alpha||} \tag{2.29}$$

Away from the wall,

$$\Phi_{ij}^{h} = -(g_1 + g_1^* \frac{P}{\varepsilon})\varepsilon b_{ij} + g_2 \varepsilon (b_{ik}b_{ki} - \tfrac{1}{3} b_{kl}b_{kl}\delta_{ij}) + (g_3 - g_3^* \sqrt{b_{kl}b_{kl}})kS_{ij} + g_4 k(b_{ik}S_{jk} + b_{jk}S_{ik} - \tfrac{2}{3} b_{lm}S_{lm}\delta_{ij}) + g_5 k(b_{ik}\Omega_{jk} + b_{jk}\Omega_{ik}) \tag{2.30}$$

$$b_{ij} = \frac{\overline{u_i u_j}}{2k} - \tfrac{1}{3}\delta_{ij} \tag{2.31}$$

Rate of strain and rotation are seen below in Equations (2.32) & (2.33), respectively.

$$S_{ij} = \tfrac{1}{2}(\frac{\partial U_i}{\partial x_j} + \frac{\partial U_j}{\partial x_i}) \tag{2.32}$$

$$\Omega_{ij} = \tfrac{1}{2}(\frac{\partial U_i}{\partial x_j} - \frac{\partial U_j}{\partial x_i}) \tag{2.33}$$

The model constants for the k-ε model with elliptic blending are seen below in Table 2.4.

Table 2.4: Model Constants for the k-ε Model with Elliptic Blending [27]

$C_{\varepsilon 1}$	$C_{\varepsilon 2}$	$C_{\varepsilon 3}$	C_{μ}	σ_{ε}	σ_k	C_L	C_{η}	C_T	g_1	g_1^*	g_2	g_3	g_1^*	g_4	g_5
1.4	1.85	0.55	0.22	1.22	1	0.45	80	6	3.4	1.8	4.2	0.8	1.9	1.25	0.4

2.4.5: The SST k-ω Turbulence Model

In contrast to the k-ε turbulence models, the k-ω turbulence models use specific turbulent dissipation rate as the second transport equation. The SST (Shear Stress Transport) k-ω turbulence model of F. Menter [29], [28] is an extension of the wilcox k-ω model that was developed to break the strong dependence of the model on the freestream specific turbulent dissipation rate in boundary layer flows by blending the model with the k-ε model outside of the shear layer [28]. The equations for turbulent kinetic energy and specific dissipation rate are given below as Equations (2.34) & (2.35), respectively.

$$\frac{\partial(\rho k)}{\partial t} + \frac{\partial(\rho U_i k)}{\partial x_i} = \tilde{P}k - \beta^*\rho k\omega + \frac{\partial}{\partial x_i}[(\mu + \sigma_k \mu_T)\frac{\partial k}{\partial x_i}] \tag{2.34}$$

$$\frac{\partial(\rho\omega)}{\partial t} + \frac{\partial(\rho U_i \omega)}{\partial x_i} = \alpha\frac{1}{\nu_T}\tilde{P}k - \beta\rho\omega^2 + \frac{\partial}{\partial x_i}[(\mu + \sigma_\omega \mu_T)\frac{\partial \omega}{\partial x_i}] + 2(1 - F_1)\rho\sigma_{\omega 2}\frac{1}{\omega}\frac{\partial k}{\partial x_i}\frac{\partial \omega}{\partial x_i} \tag{2.35}$$

Here, turbulent viscosity is calculated as Equation (2.36),

$$\nu_T = \frac{a_1 k}{max(a_1\omega, SF_2)} \tag{2.36}$$

Where S is the invariant measure of the strain rate, calculated in Equation (2.37),

$$S = \sqrt{2S_{ij}S_{ij}} \tag{2.37}$$

and

$$\tilde{P}k = \mu_T \frac{\partial U_i}{\partial x_j}\left(\frac{\partial U_i}{\partial x_j} + \frac{\partial U_j}{\partial x_i}\right) \tag{2.38}$$

$$\tilde{P}k = min(P_k, 10 * \beta^* \rho k\omega) \tag{2.39}$$

In the above equations, F_1 and F_2 are blending functions only applied inside the shear layer, where

$$F_1 = tanh\{\{min[max(\frac{\sqrt{k}}{\beta^* \omega y}, \frac{500\nu}{y^2\omega}), \frac{4\rho\sigma_{\omega 2}k}{CD_{k\omega}y^2}]\}^4\} \tag{2.40}$$

$$F_2 = tanh[[max(\frac{2\sqrt{k}}{\beta^* \omega y}, \frac{500\nu}{y^2\omega})]^2] \tag{2.41}$$

and

$$CD_{k\omega} = max(2\rho\sigma_{\omega 2}\frac{1}{\omega}\frac{\partial k}{\partial x_i}\frac{\partial \omega}{\partial x_i}, 10^{-10}) \tag{2.42}$$

The model constants are shown below in Table 2.5.

Table 2.5: Model Constants for the SST k-ω Model [29]

α_1	α_1	β_1	β_1	β^*	σ_{k1}	σ_{k2}	$\sigma_{\omega 1}$	$\sigma_{\omega 2}$
5/9	0.44	3/40	0.0828	0.09	0.85	1	0.5	0.856

2.4.6: The γ Transitional Model

Used in conjunction with the SST k-ω model, transitional models can be applied in Star CCM+ to aid in modeling the transition to turbulent flow. The transitional model used in this work is the γ transition of Menter et al. [30]. This is a one equation model that solves an additional transport equation (Equation (2.43) below) for turbulence intermittency, γ, in the developing regime of a boundary layer flow.

$$\frac{\partial(\rho\gamma)}{\partial t} + \frac{\partial(\rho U_j \gamma)}{\partial x_j} = P_\gamma - E_\gamma + \frac{\partial}{\partial x_j}\left[\left(\mu + \frac{\mu_T}{\sigma_\gamma}\right)\frac{\partial \gamma}{\partial x_j}\right] \tag{2.43}$$

Here, the transition source term P_γ is defined as

$$P_\gamma = F_{length}\rho S\gamma(1-\gamma)F_{onset} \tag{2.44}$$

And the relaminarization source term E_γ is defined as

$$E_\gamma = C_{a2}\rho\Omega\gamma F_{turb}(C_{e2}\gamma - 1) \tag{2.45}$$

The “trigger functions” [30] that control the model and their dependencies can be seen below in the following equations.

$$F_{onset1} = \frac{Re_v}{2.2Re_{\theta c}} \tag{2.46}$$

$$F_{onset2} = min(F_{onset1}, 2.0) \tag{2.47}$$

$$F_{onset3} = max(1 - (\frac{R_T}{3.5})^3, 0) \tag{2.48}$$

$$F_{onset} = max(F_{onset2} - F_{onset3}, 0) \tag{2.49}$$

$$F_{turb} = e^{-(\frac{Re_T}{2})^4} \tag{2.50}$$

$$R_T = \frac{\rho k}{\mu \omega} \tag{2.51}$$

$$Re_v = \frac{\rho d_\omega^2 S}{\mu} \tag{2.52}$$

$$Re_{\theta c} = f(Tu_L, \lambda_{\theta L}) \tag{2.53}$$

Here,

$$Tu_L = min(100\frac{\sqrt{2k/3}}{\omega d_\omega}, 100) \tag{2.54}$$

$$\lambda_{\theta L} = -7.57 \cdot 10^{-3} \frac{dV}{dy} \frac{d_\omega^2}{\nu} + 0.0128 \tag{2.55}$$

The model constants are shown below in Table 2.6.

Table 2.6: Model Constants for the γ Transition Model [30]

F_{length}	C_{e2}	C_{a2}	σ_γ
100	50	0.06	1.0

2.4.7: Wall Treatment for all Models

Since all models used in this work will be employing all *y*+ treatment, discussion on the all *y*+ treatment option in Star CCM+ is required. All *y*+ treatment refers to a combination of low *y*+ treatment and high *y*+ treatment near the wall. This treatment is generally always recommended, as it accounts for both fine and coarse meshes at once. The low *y*+ treatment is applied where the mesh is fine enough (*y*+~1) that the viscous sublayer can be resolved without modeling or use of wall functions [39]. The high *y*+ treatment accounts for higher *y*+ values by applying standard wall functions in the logarithmic region [14]. The all *y*+ approach either applies the high *y*+ or low *y*+ approaches along a wall based on *y*+ values.

Additionally, the Standard k-ε and Realizable k-ε models used in this work employ two layer wall treatment, proposed in 1991 by W. Rodi [34]. With two layer treatment, the viscous sublayer and the buffer layer can be resolved. In the near wall layer, dissipation rate and turbulent viscosity are solely functions of wall distance in a one equation model. Further away from the wall, the standard wall functions of Launder and Jones [20] are employed.

CHAPTER 3: FLOW VALIDATION CASE SIMULATION SETUP

As previously discussed, in order to produce quality results using RANS turbulence modeling and simulation, a degree of flow validation must first be carried out against published experimental data to ensure that the simulations are able to accurately reproduce results. For the wall-jet hump-wake, four validation cases are carried out; a plane wall jet, a wall jet with an external stream (both with $U_J/U_S > 1$ and $U_J/U_S < 1$), and the NASA hump wake. Considering the large number of simulations presented in this work and the computational size and time constraints of turbulence modeling and simulation, it was decided that the simulations are to be carried out in only two dimensions. This allows for the mesh for each simulation to be further refined while remaining conscious of cell count and thus computational demand. For each simulation, mesh parameters were adjusted over a series of simulations until a quality, grid independent refined mesh was tailored for each case. The following sections describe the simulation setup for each flow case in detail.

3.1: The Wall Jet

For the wall jet, the 1998 experimental investigation of Eriksson et al. [10] was chosen as the reference. Additionally, the 2016 work of Fu et al. [14] was used as a starting reference for the initial meshing parameters, since the 1998 work of Eriksson et al. [10] was also used as the validation case for their work and results were acceptable. In reference to jet slot height h=9.6mm, the domain length extended 729h downstream from the jet inlet and was 153h high. This domain size matches both the experimental water tank size of [10] and the domain size used by [14]. The boundary conditions for each of the boundaries can be found in the appendix in Table A.1.

The final mesh contained 1,270,393 cells, a base size of 1.25h, and a number of refinements. Five conical refinements were created that extended from the domain inlet to x/h=

10, 50, 100, 200, and 729, each one containing cells 25% smaller than the preceding refinement. The first refinement extended 5*h* in the wall normal direction at the upstream edge and each following refinement was 5*h* higher than the preceding. The angle of the cone for all refinements followed the angle of the jet spread rate. The nearest conical refinement can be seen in Figure 3.1 below. Additionally, a refined zone was created along the shear layer of the jet, with cell sizes 12.5% of the base size. Prism layers were grown on the bottom wall, with a near wall thickness of 0.001*h* and a total number of 34 layers, spanning approximately 1/3 of the boundary layer height at x/h=50. The calculated stretch factor for these prism layers was 1.176.

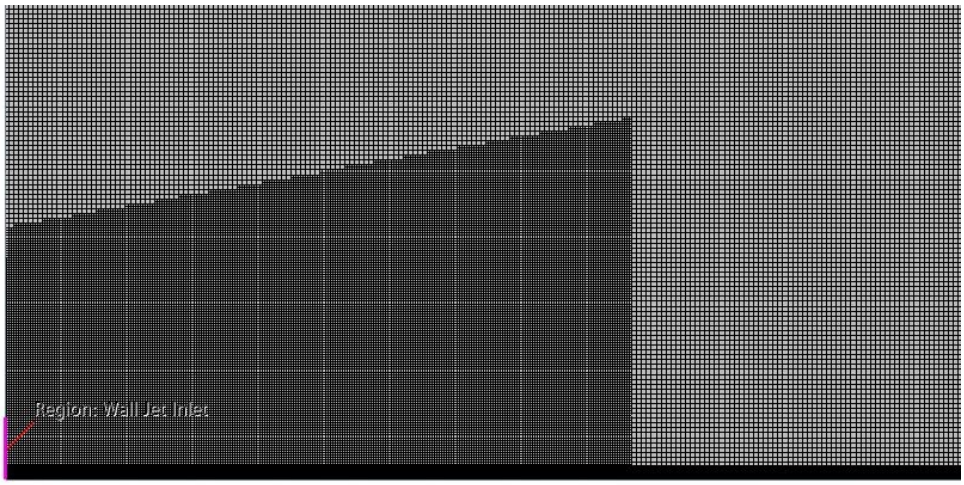

Figure 3.1: Wall Jet Validation Case Near-Jet Refinement

The working fluid for these simulations was water, in accordance with the experiment of Eriksson et al. [10], and the jet inlet velocity was set to 1*m/s*, yielding a Reynolds number based on slot height of $Re=hU_J/\nu$ =9,600. Additionally, turbulence intensity was set to 0.1% in reference to the intensity of the experimental tank [10]. As a quality check for the simulations, the wall $y+$ value was calculated along the bottom wall at each measurement point (Table 3.1).

Table 3.1: Wall $y+$ Values for Wall Jet Validation Case

Model	SST k-ω	Standard k-ε	SST k-ω w/ γ Transport	k-ε with Elliptic Blending	Realizable k-ε	V^2F k-ε
x/h	Wall $y+$	Wall $y+$	Wall $y+$	Wall $y+$	Wall $y+$	Wall $y+$
10	0.2582	0.2747	0.1708	0.1700	0.2724	0.2209
20	0.2405	0.2544	0.1425	0.1419	0.2446	0.2463
40	0.2101	0.1942	0.1824	0.2558	0.2028	0.2219
70	0.1552	0.1407	0.1605	0.1732	0.1447	0.1629
100	0.1255	0.1143	0.1302	0.1374	0.1169	0.1309
150	0.0978	0.0901	0.1012	0.1065	0.0921	0.1021
200	0.0821	0.0762	0.0848	0.0896	0.0780	0.0856

It can be seen from the table that all wall $y+$ values are within a suitable range of $0.5<y+<0.05$. Once the final mesh was generated and initial results were found suitable, the simulation was run for each of the six turbulence models outlined in chapter 2.

3.2: The Wall Jet in a Co-flowing Stream

The simulation setups for both wall jet in a co-flowing stream simulations were constructed in reference to the 1971 work of Kacker and Whitelaw [21] as well as the simulation setup for the wall jet. Again, in reference to jet slot height, h=0.006274m, the domain extended 730h downstream from the jet inlet and was 152h high. The boundary conditions, seen in the appendix in Table A.2, were set up according to the experiment, which used a splitter plate of $h_{splitter}$=0.125h to separate the stream flow and the jet flow at the inlet. Additionally, rather than using a pressure outlet at the top of the domain as with the wall jet simulations, a symmetry plane

was used since the wind tunnel height was not provided and it was assumed that the free flowing stream was to extend past the top boundary.

The mesh for the two wall jet in a co-flowing stream validation cases was generated with the wall jet validation case used for reference. The final mesh contained 1,150,637 cells with a base size of 1h. As with the wall jet, five conical refinements extending to x/h= 10, 50, 100, 200, and 730 were created, each 25% smaller than the preceding refinement. However, considering the effects of the external stream, the wall normal height was extended to 6h at the upstream edge of the nearest refinement with each proceeding refinement 6h higher. A cylindrical refinement on the shear layer was also created with a cell size 12.5% of the base size. The near wall prism layer thickness was 0.00023h, with a total number of 38 layers extending ~⅓ of the boundary layer thickness at x/h=50 for the U_J/U_S=2.3 case. The stretch factor was calculated as 1.140

The working fluid for the wall jet in a co-flowing stream simulations was air, in accordance with Kacker and Whitelaw [21]. The inlet velocities for the jet and co-flowing stream were curve fitted to the experimental data for inlet flow conditions, as the flow was developed before the end of the splitter plate and not constant across the jet slot and stream inlet boundaries. Curve fit data for both cases can be seen below in Figure 3.2. For the U_J/U_S=2.3 case, Reynolds number based on slot height and mean jet inlet velocity (44.197m/s for U_J/U_S=2.3 and 14.412m/s for U_J/U_S=0.75) was 17,700, and for the U_J/U_S=0.75 case, Re=5,770. Turbulence intensity was set to 0.5%.

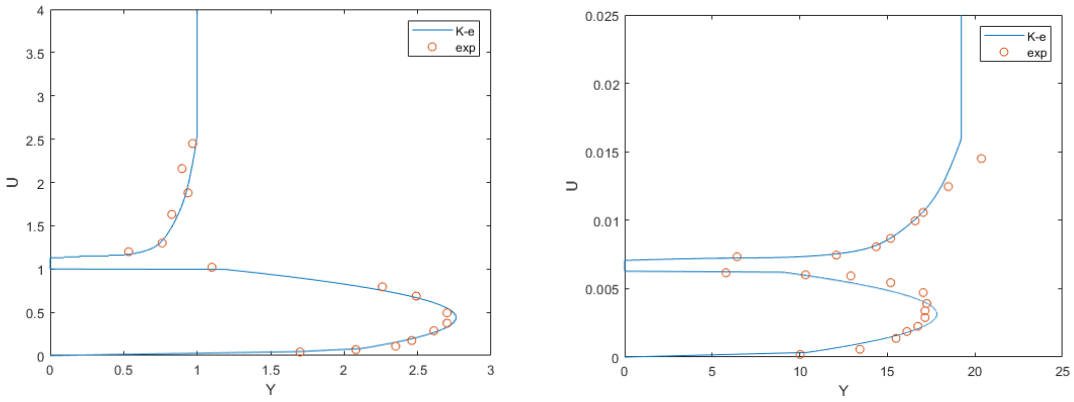

(a) (b)

Figure 3.2: Inlet Velocity Profiles; (a) U_J/U_S=2.3, (b) U_J/U_S=0.75

As with the wall jet simulations, wall *y*+ values at measurement points downstream of the jet inlet were calculated and found to be in an acceptable range (Tables 3.2 & 3.3).

Table 3.2: Wall *y*+ Values for Wall Jet in Co-Flowing Stream (U_J/U_S=2.3) Validation Case

Model	SST k-ω	Standard k-ε	SST k-ω w/ γ Transport	k-ε with Elliptic Blending	Realizable k-ε	V^2F k-ε
x/h	Wall *y*+	Wall *y*+	Wall *y*+	Wall *y*+	Wall *y*+	Wall *y*+
10	0.0939	0.1075	0.0473	0.1095	0.1015	0.1045
20	0.0976	0.1024	0.0426	0.1081	0.1018	0.1060
50	0.0860	0.0786	0.0911	0.0857	0.0824	0.0850
100	0.0633	0.0620	0.0687	0.0670	0.0627	0.0659
150	0.0577	0.0547	0.0595	0.0586	0.0547	0.0575

Table 3.3: Wall $y+$ Values for Wall Jet in Co-Flowing Stream (U_J/U_S=0.75) Validation Case

Model	SST k-ω	Standard k-ε	SST k-ω w/ γ Transport	k-ε with Elliptic Blending	Realizable k-ε	V^2F k-ε
x/h	Wall *y+*	Wall *y+*	Wall *y+*	Wall *y+*	Wall *y+*	Wall *y+*
10	0.0802	0.1104	0.0597	0.0650	0.1064	0.0945
20	0.0934	0.1037	0.0524	0.1085	0.1043	0.1041
50	0.0932	0.0923	0.0452	0.0916	0.0855	0.0905
100	0.0850	0.0959	0.0895	0.0912	0.0839	0.0907
150	0.0874	0.0964	0.0892	0.0959	0.0911	0.0954

Wall $y+$ results for the wall jet in a co-flowing steam cases show that for both velocity ratios all wall $y+$ values are within a suitable range of $0.5<y+<0.05$ with the exception of one point for both cases and the SST k-ω model with γ transition, for which the wall $y+$ value is slightly lower than 0.05. Once the final mesh was generated and initial results were found suitable, the simulation was run for each of the six turbulence models outlined in chapter 2.

3.3: The NASA Hump Wake

The validation case simulation for the NASA hump wake was constructed largely in conformance with the NASA cfdeval workshop guidelines [22]. Using a reference parameter of the hump's chordlength ($c=0.420m$), the domain extended $70c$ downstream of the hump's trailing edge, $7.15c$ upstream of the leading edge, and was approximately $0.91c$ high. The maximum height of the hump was $0.0537m$. Since a test section height was given and noted to be relatively close to the hump, the top boundary of the hump was modelled as a wall. The hump was split into

fore and aft sections, with the fore section extending to the inlet of the domain and the aft section starting at 0.475*c* and extending to the outlet of the domain (*x/c*=0 is located at the leading edge of the hump). Boundaries can be seen in the appendix (Table A.3).

The final mesh contained 1,944,138 cells with a base size of 0.01875*c*. The mesh for this case contained three refinements. The first contained cells 50% of the base size and spanned streamwise from one end of the domain to the other. The height of this refinement was 0.66*c.* The second refinement (25% of base size) spanned from -3.12*c* upstream from the hump's leading edge to 4.93*c* downstream from the trailing edge and was 0.48*c* high. The nearest refinement, targeted at the recirculation zone, started 0.45*c* downstream from the leading edge and was 2.14*c* long and 0.24*c* high. Cells in this zone were only 6.25% of the base size. Additionally, a surface control was employed along the hump surface, with cells only 4% of the base size. The near wall prism layer thickness upstream of the hump and along the top wall was 1.19E-5*c*, and 88 layers were extruded with a stretch factor of 1.1. Starting at *x/c*=0.45 and going downstream, a total of 92 prism layers were extruded with a near wall thickness of 2.38E-5*c*. The stretch factor for these prism layers was 1.086. A zoomed view of the final mesh, highlighting prism layer extrusions along the hump wall and the finest refinement, can be seen below in Figure 3.3.

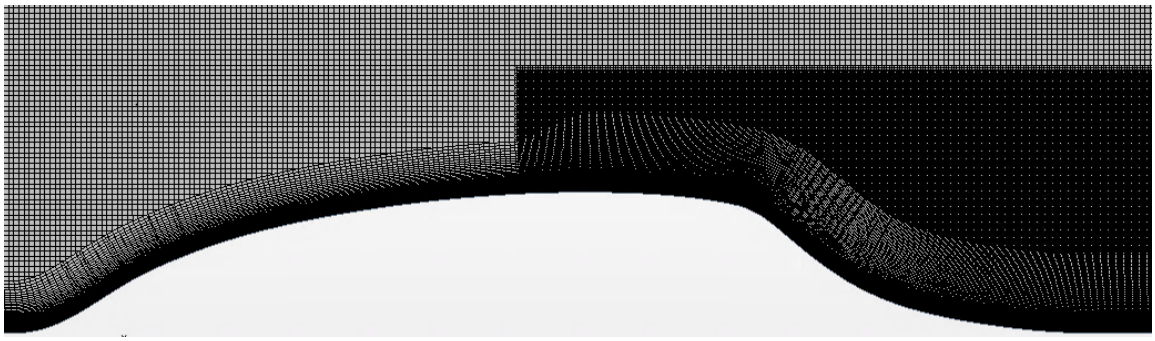

Figure 3.3: Zoomed Mesh Scene for the Hump Wake Validation Case

The simulation was run with air as the working fluid and an inlet velocity of 33.96*m/s*. The flow conditioning of the incoming stream was such that the boundary layer was fully developed with a height of approximately 0.078*c* at *x/c*=-2.14 upstream of the hump's leading edge. The inlet velocity is slightly lower than the inlet velocity used in [16] as well as the prescribed inlet value in [22] (34.6*m/s*), but this was found to be suitable for the boundary layer development. Comparison for the inlet boundary layer profile for the simulations against experimental data are seen below in Figure 3.4. Thus, the Reynolds number based on inlet velocity and chordlength for the presented simulations is 910,000, whereas the Reynolds number for the experimental work [16] was 936,000. Turbulence intensity was 0.9%.

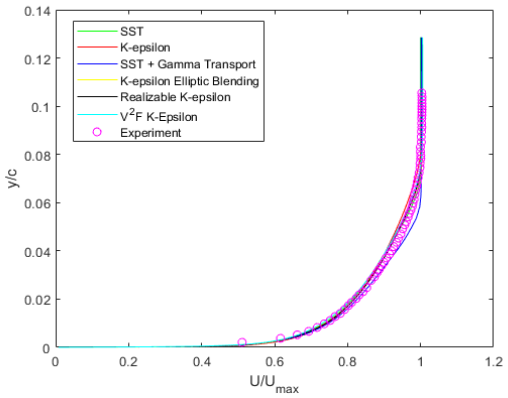

Figure 3.4: Hump Wake Validation Case Incoming Boundary Layer at *x/c*=-2.14

As with the preceding two cases, the wall *y+* value along the bottom wall of the domain was calculated. Results are seen below in Table 3.4.

Table 3.4: Wall $y+$ Values for Hump Wake Validation Case

Model	SST k-ω	Standard k-ε	SST k-ω w/ γ Transport	k-ε with Elliptic Blending	Realizable k-ε	V^2F k-ε
x/c	Wall *y+*	Wall *y+*	Wall *y+*	Wall *y+*	Wall *y+*	Wall *y+*
-2.14	0.2109	0.2053	0.2099	0.2118	0.2038	0.2101
0	0.0596	0.0539	0.0743	0.1045	0.0620	0.0860
0.65	0.4828	0.2300	0.2101	0.2651	0.4322	0.3505
0.8	0.1659	0.1322	0.1506	0.1388	0.1329	0.1523
0.9	0.2443	0.2166	0.2160	0.2252	0.2084	0.2392
1.0	0.2612	0.2727	0.2551	0.2829	0.2792	0.3163
1.1	0.1653	0.2813	0.2805	0.2894	0.3173	0.3458
1.2	0.1637	0.2287	0.2233	0.2336	0.2976	0.3017
1.3	0.2709	0.0806	0.0614	0.0655	0.1598	0.1505

It can be seen from the above table that wall $y+$ values are satisfactory ($0.5<y+<0.05$). As with the other three cases, the hump wake validation case was run for all six validation cases once the final mesh was generated.

CHAPTER 4: FLOW VALIDATION CASE RESULTS

Overall, results were relatively accurate for the wall jet and wake simulations, while the results for the wall jet in a co-flowing stream cases were lacking in agreeance with experimental data. For each case, results were generated and compared for all data of interest in each case. From the results, a best fit model was selected to be used for the final wall-jet hump-wake simulations, based on its performance relative to the other five models in all four cases. This chapter covers results for all three cases as well as a detailed analysis and selection of the best fit model.

4.1: The Wall Jet

Results for the wall jet validation case, based on the experimental work of Eriksson et al. [10], were overall very satisfactory. The experimental data mainly consisted of numerous streamwise velocity profiles, but also included Reynolds stresses and wall-normal velocities. Streamwise velocities were plotted in both inner and outer scaling. Essentially, the inner scaling plots focused on the velocity profiles near the wall while the outer scaling plots focused on the mean flow profiles. The equations for $u+$ and $y+$, inner scaled velocities, can be found below in Equations (4.1) & (4.2), respectively.

$$u+ = \frac{U}{u^*} \tag{4.1}$$

$$y+ = \frac{u^* y}{\nu} \tag{4.2}$$

Inner scaled streamwise velocity profiles at *x/h*=10, 20, & 40, (Figure 4.1) show the initial development of the wall jet, along with wall normal velocity profiles (Figure 4.2) and Reynolds stress profiles (Figure 4.3) at these locations.

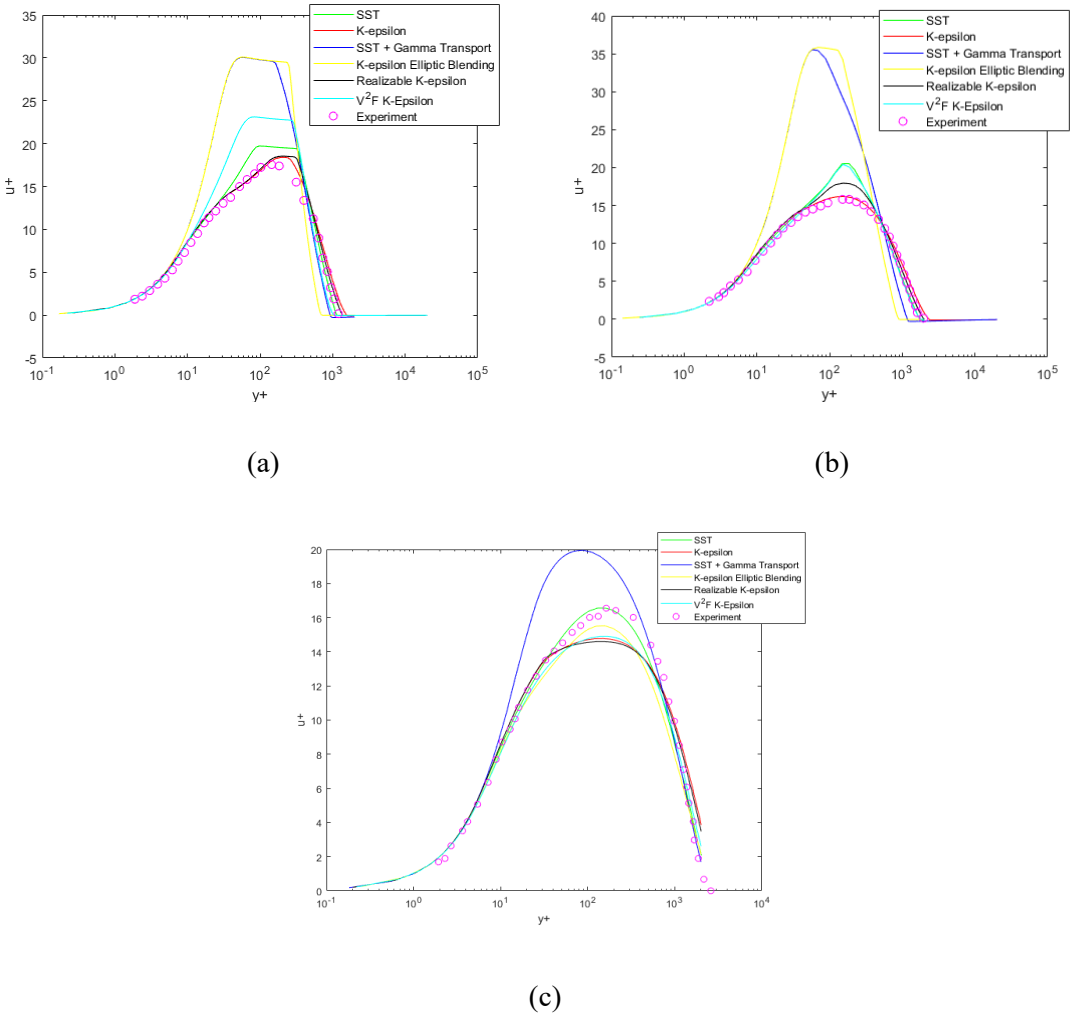

(a) (b)

(c)

Figure 4.1: Wall Jet Streamwise Velocity Profiles in Inner Scaling; (a) *x/h*=10, (b) *x/h*=20, (c) *x/h*=40

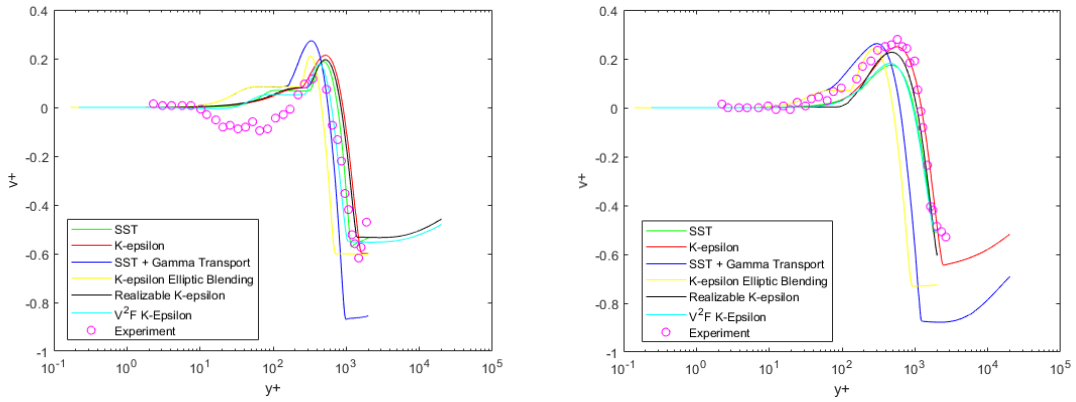

(a) (b)

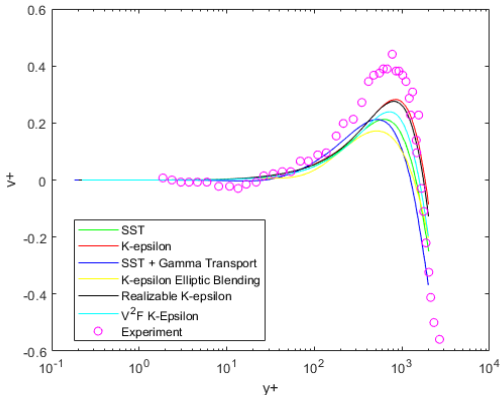

(c)

Figure 4.2: Wall Jet Wall-Normal Velocity Profiles in Inner Scaling; (a) *x/h*=10, (b) *x/h*=20, (c) *x/h*=40

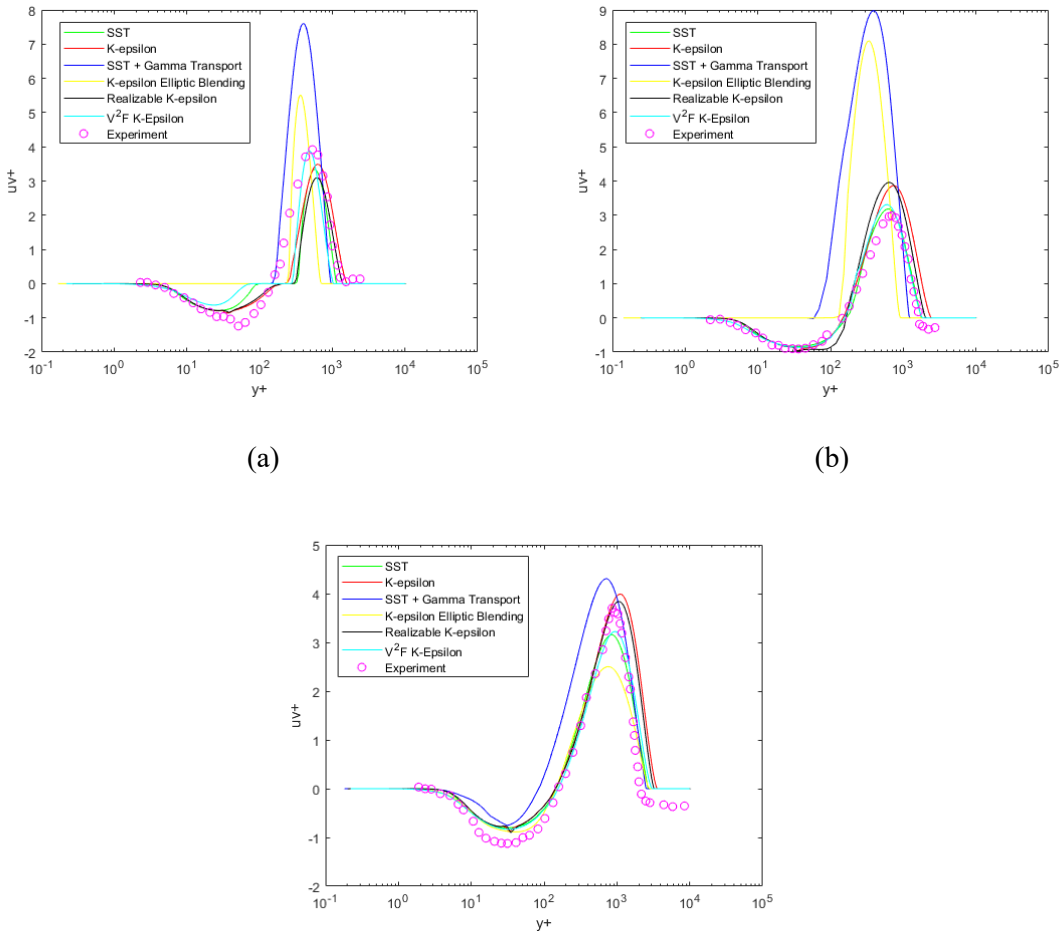

Figure 4.3: Wall Jet Reynolds Stress Profiles in Inner Scaling; (a) *x/h*=10, (b) *x/h*=20, (c) *x/h*=40

According to the experimental data [10], the wall jet enters the transitional regime around *x/h*=10 and begins to enter the fully turbulent regime at *x/h*=20, becoming a well defined fully turbulent flow at *x/h*=40. Overall, the simulation data appears to be underdeveloped. At *x/h*=10, the plateau in the streamwise velocity profile for all six models is very well defined, whereas it is not for the experimental data, which indicates underdevelopment in the CFD predictions. At *x/h*=20, the plateau in streamwise velocity has faded (the start of the fully turbulent regime) in all models except for the k-ε with elliptic blending model, which sheds this plateau at *x/h*=40. The

wall normal velocity profile at x/h=10 shows a negative dip in velocity near the wall for the experimental data, indicating the onset of the transitional regime, whereas the profiles for all of the RANS models (with the exception of the SST k-ω model, which becomes slightly negative in this region) do not become negative near the wall. The Reynolds stresses are also in agreement with underdevelopment, with overall lower predictions near the wall than what is observed in the experimental data.

In regard to the best fit model for the wall jet initial development, it is clear that the k-ε with elliptic blending model and the SST k-ω with γ transition model both performed very poorly. The remaining four models were at the very least acceptable in their predictions. Looking at the streamwise velocity profiles, the standard k-ε model performed the best in the transitional regime (x/h=10 & 20), while the SST k-ω model performed the best in the well defined fully turbulent regime (x/h=40). None of the models accurately predicted the wall-normal velocity profiles well until x/h=20, after which the standard k-ε model was the best fit. Regarding Reynolds stress predictions, the standard and realizable k-ε models and the SST k-ω model all produced the best results.

Velocity profiles were scaled with both outer and inner variables in the fully developed regime for the experimental data [10]. As stated above, outer variables were useful in comparing the mean velocity profiles. Figure 4.4 below shows the streamwise velocity profiles at x/h=20, 40, 70, 100, 150, and 200 in outer scaling and Figure 4.5 below shows the wall-normal velocity profile at x/h=70 in outer scaling.

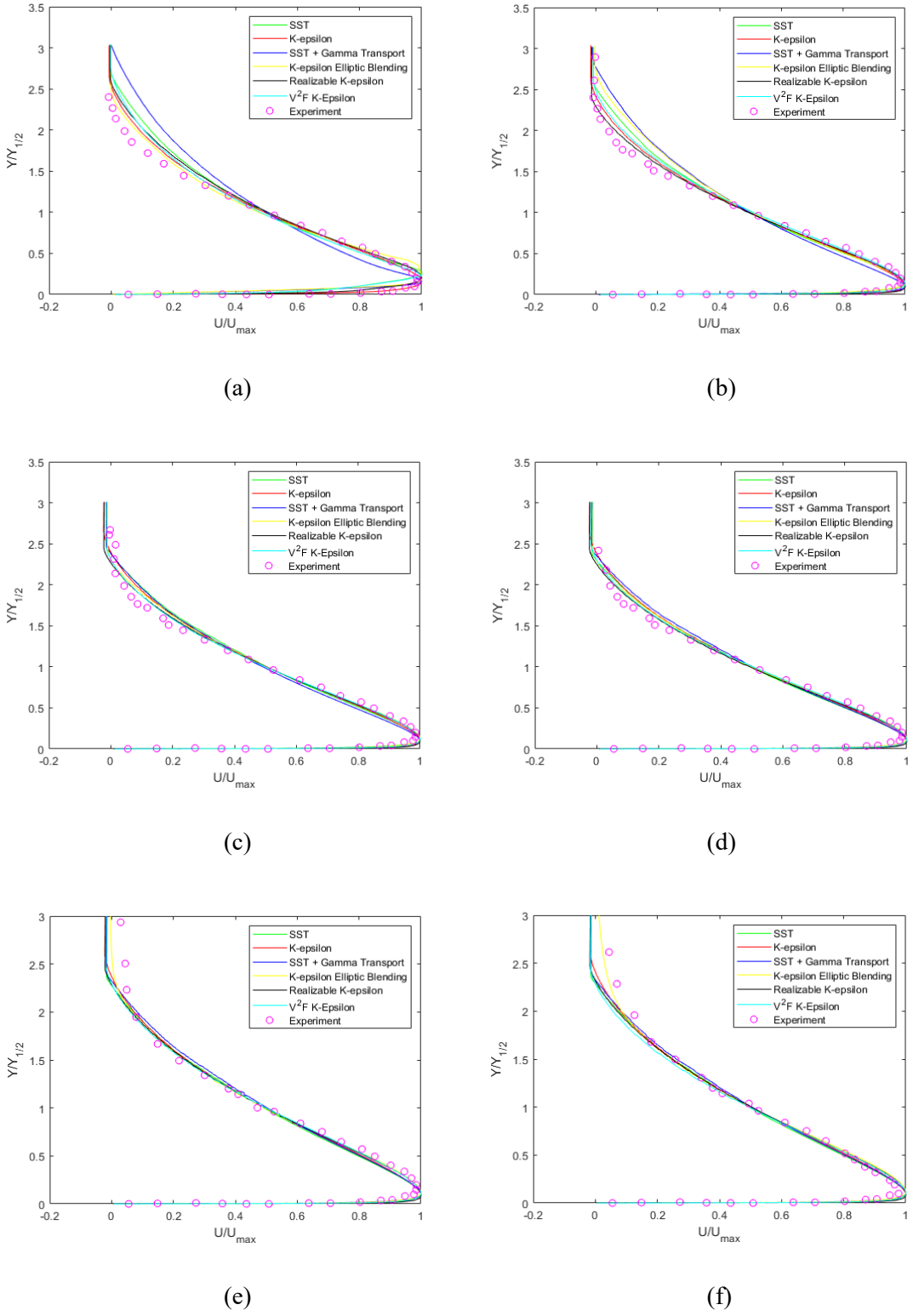

Figure 4.4: Wall Jet Streamwise Velocity Profiles in Outer Scaling; (a) *x/h*=20, (b) *x/h*=40, (c) *x/h*=70, (d) *x/h*=100, (e) *x/h*=150, (f) *x/h*=200

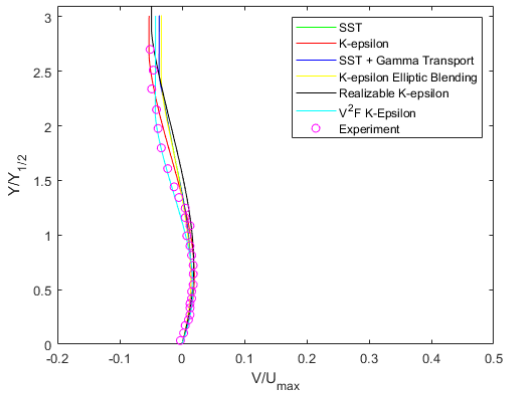

Figure 4.5: Wall Jet Wall-Normal Velocity Profiles in Outer Scaling at *x/h*=70

Noted in Figure 4.4 is the excellent collapse in data for the experimental data and the simulations, a defining characteristic of shear layer development in turbulent jets. Additionally, all RANS predictions were very close to each other in the free shear jet layer. The only outliers are the SST k-ω with γ transition in the shear layer at upstream measurement points (*x/h*=20 & 40) and the k-ε model with elliptic blending at the shear layer at *x/h*=150 & 200. However, it is noted in the original experiment [10] that return flow effects of the test section were present at *x/h*=200. In theory, using the outer scaling parameters of [10], U/U_{max} is expected to tend to zero at the same scaled height $Y/Y_{1/2}$ along the entire length of the fully turbulent jet regime. For this jet, that height is approximately $2.25<Y/Y_{1/2}<2.5$. Regarding the large deviance of all models from experimental data at *x/h*=20, it was already shown that turbulence models were all underdeveloped as well as overpredicting the peak streamwise velocity, which accounts for this overprediction of the outer edge of the jet shear layer. However, the edge of the shear layer as reported in the experimental data is seen to be well over $Y/Y_{1/2}=2.5$ at *x/h*=150 in addition to the reported overshoot at *x/h*=200, which indicated the possibility of slight return flow effects at this point. It is clear that the RANS predictions do not match the experimental data reporting the shear layer outer edge here. In respect to the best fit model, it can be seen that the standard and

realizable k-ε models overall show the best agreement, with the exception of *x/h*=70 & 100, where the SST k-ω model shows the best prediction of the free jet layer. Overall, almost all models show a remarkable degree of accuracy in this layer. The wall-normal velocity profile plot at *x/h*=70 shows the best results to be produced with the standard k-ε model.

While the above outer scaled velocity plots show generally acceptable agreeance in the scaled location of the outer edge of the shear layer between most of the RANS models, it can be seen that not all of the models agree in the exact wall-normal location of U_{max}, which can be better represented through a scaled plot of the jet half-width, or the jet growth rate (Figure 4.6).

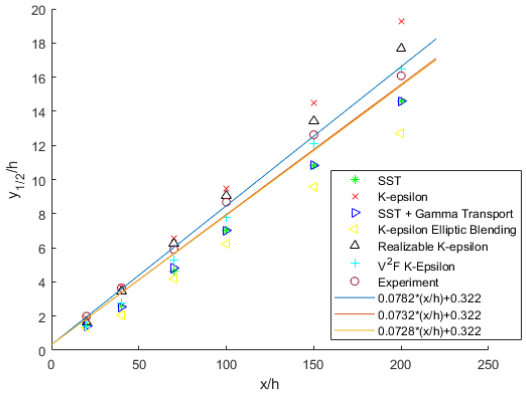

Figure 4.6: Wall Jet Growth Rate

In this plot, there are 3 solid lines. The blue line, 0.0782*(*x/h*)+0.322, represents the best linear fit to the experimental data [10]. The orange and yellow solid lines represent the expected rate of spread (0.0728*x/h* to 0.0732*x/h*) to satisfy momentum conservation, proposed by Launder and Rodi [23]. While it was shown in [10] that momentum conservation was indeed satisfied, it was interesting to also compare RANS simulation results to the original spread rate range proposed by [23]. It is seen here that the only RANS data that falls between the experimental data and the proposed rate of spread from [23] is the data of the V^2F k-ε model at *x/h*=150 & 200. Rate of

spread coefficients were calculated through curve fitting for each model and seen below in Table 4.1, which shows the two SST k-ω models to have performed the best in regard to the experimental data [10].

Table 4.1: Wall Jet Spread Rates Predicted by RANS Models

Model	SST k-ω	Standard k-ε	SST k-ω w/ γ Transport	k-ε with Elliptic Blending	Realizable k-ε	V^2F k-ε
Spread Rate	0.07178	0.09723	0.07407	0.06491	0.08944	0.08424
Deviation from [10]	8.94%	19.57%	5.58%	20.47%	12.57%	7.17%

As a veracity measurement related to skin friction predictions, the very near wall streamwise velocity profiles were plotted in inner scaling, seen below in Figure 4.7.

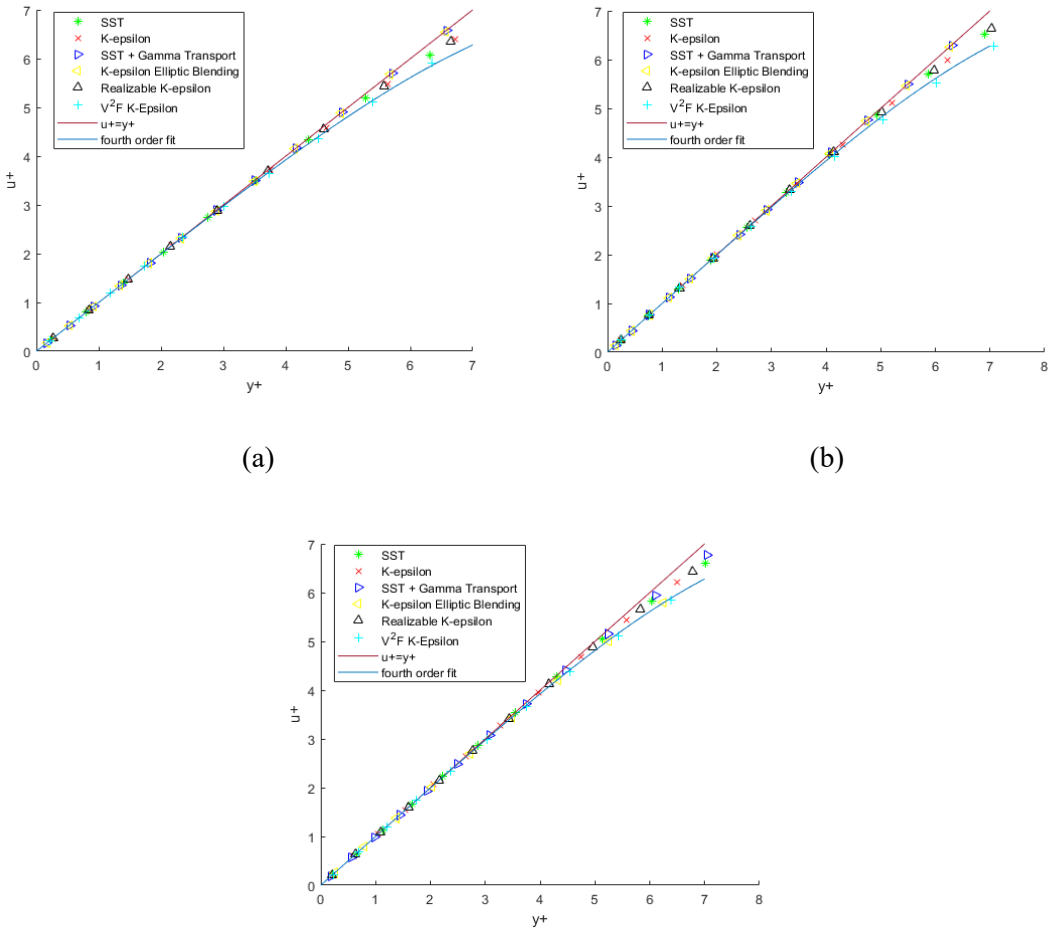

Figure 4.7: Wall Jet Near-Wall Streamwise Velocity Profiles; (a) x/h=10, (b) x/h=20, (c) x/h=40

From the above plots, the data from the RANS predictions fits the characteristic linear relation of $u+=y+$ for boundary layer flows as well as the experimental data [10]. It is noted in the experiment of Eriksson et al. [10] that the experimental data followed a fourth order fit better than the linear fit for $y+>\sim3.5$. From this point on, the V^2F k-ε model best fits the experimental data, while the Realizable k-ε model best fits the linear relationship. However, all data fits between the two for x/h=10, 20, & 40.

Traditionally, for a flat plate boundary layer flow, there is a log law region in which $u+$ is a logarithmic function of $y+$ ($u+=2.44*ln[y+]$). Figure 4.8 plots the streamwise velocity profiles at x/h=40, 70, 100, &150 with a straight line representing the log law for a flat plate boundary layer flow.

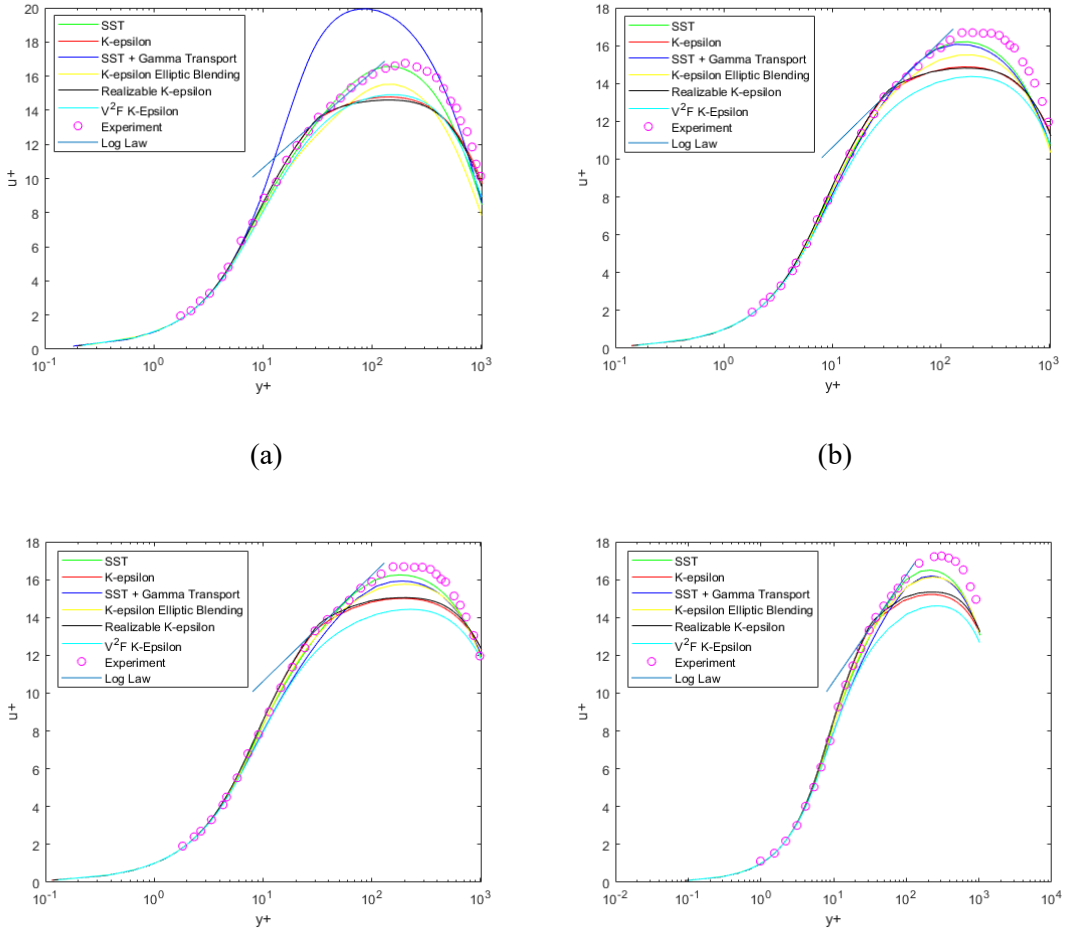

Figure 4.8: Wall Jet Streamwise Velocity Profiles in Inner Scaling with Log Law; (a) x/h=40, (b) x/h=70, (c) x/h=100, (d) x/h=150

It is seen here that none of the data, experimental or predicted, really defines the log law region. However, it is suggested by George et al. [15] that a power law relation better suits this region of the flow for wall jets.While this is worth mentioning, it is unfortunately beyond the scope of this thesis and thus will not be investigated in detail. Looking at the overall accuracy of each model, it is undoubted that the SST k-ω model predicted the best results for all measurement points in the four plots immediately above, showing that in the fully turbulent regime this model performs the best near the wall.

Reynolds stresses in the fully turbulent regime were also examined and can be seen below (Figure 4.9).

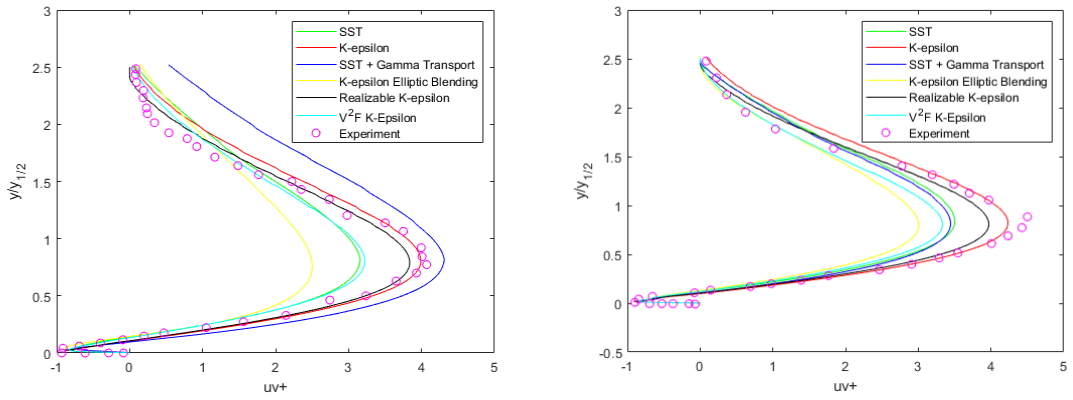

Figure 4.9: Reynolds Stresses in Outer Scaling; (a) *x/h*=40, (b) *x/h*=70, (c) *x/h*=100, (d) *x/h*=150

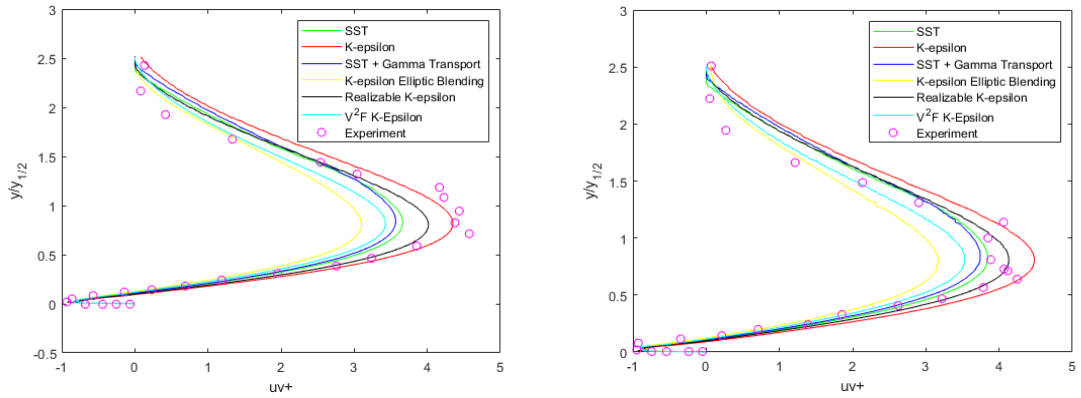

(c) (d)

Figure 4.9 (Continued): Reynolds Stresses in Outer Scaling; (a) *x/h*=40, (b) *x/h*=70, (c) *x/h*=100, (d) *x/h*=150

Consistent with what would be expected in a wall jet flow, there is a negative peak in Reynolds stresses near the wall followed by an outer positive peak between 2 and 4 times the magnitude (3 times the magnitude for [10]) due to the jet velocity. However, it is noted that there is not a very well defined collapse of data at the outer edge of the shear layer for the RANS data, whereas the experimental data shows a good collapse. The collapse of the RANS data does become more defined with downstream distance, again citing the inlet flow issues and underdevelopment as potential issues. Overall, it appears that the standard k-ε model had the best predictions for the maximum positive Reynolds stress. Seen below in Figure 4.10, the Reynolds stresses were also plotted using inner scaling, showing the negative Reynolds stress profile at the wall in more detail.

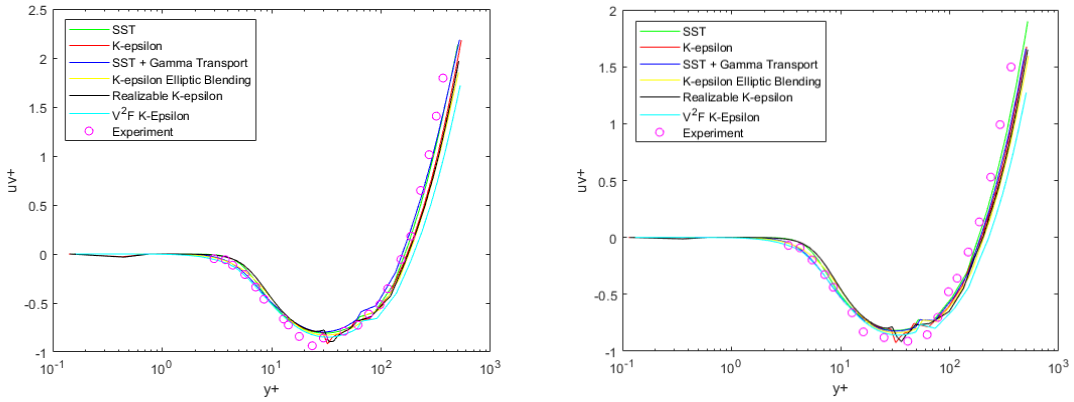

(a) (b)

Figure 4.10: Reynolds Stresses in Inner Scaling; (a) *x/h*=70, (b) *x/h*=100

From the figures above, it can be seen that all models produced fairly accurate predictions in the boundary layer region of the fully turbulent wall jet. It is very difficult to determine a best model, but the SST k-ω model appears to be of best fit.

4.2: The Wall Jet in a Co-flowing Stream

The wall jet in a co-flowing stream results for the RANS validation cases were overall disappointing. This could be due to many factors, and a number of them are outlined in chapter 7. However, the results were compared to those of Kacker and Whitelaw [21], with outer scaling of wall normal distance followed according to that used by Naqavi and Tucker [31]. Results compared were streamwise velocity profiles and Reynolds stress profiles for both the U_J/U_S=2.3 & 0.75 cases. Additionally, since the velocity profile for the wall jet exceeded the freestream flow, wall jet streamwise velocity decay was also able to be compared.

Starting with velocity profiles, Figure 4.11 shows the streamwise velocity profile for the U_J/U_S=2.3 case at *x/h*=10 & 150. Additionally, Figure 4.12 shows the same profile for the U_J/U_S=0.75 case at the same locations.

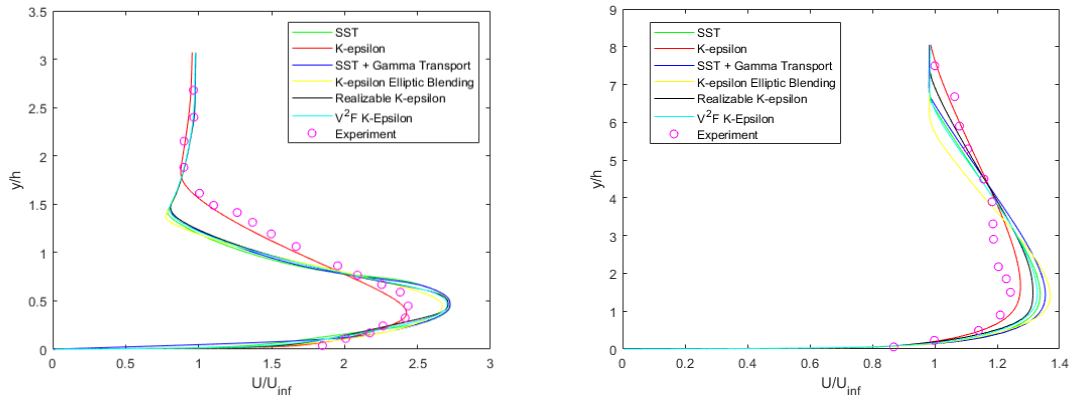

(a) (b)

Figure 4.11: Wall Jet in a Co-Flowing Stream (U_J/U_S=2.3) Streamwise Velocity Profiles; (a) *x/h*=10, (b) *x/h*=150

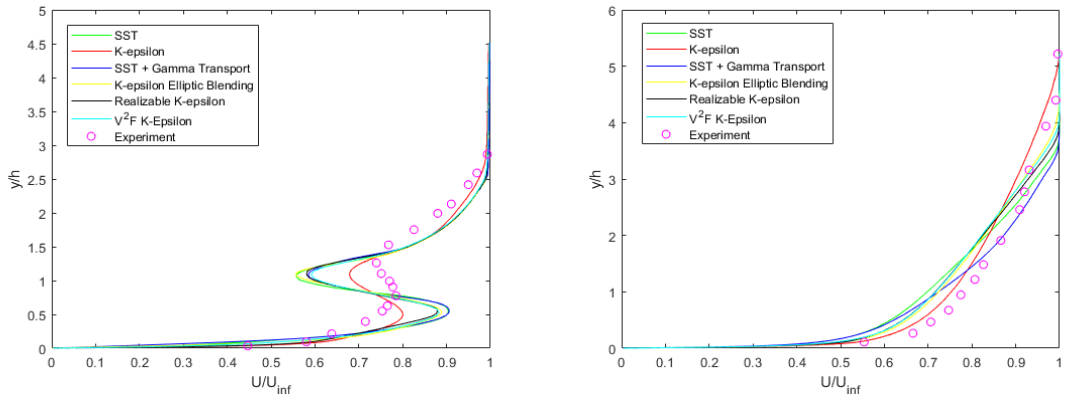

(a) (b)

Figure 4.12: Wall Jet in a Co-Flowing Stream (U_J/U_S=0.75) Streamwise Velocity Profiles; (a) *x/h*=10, (b) *x/h*=150

It is worth noting that in these results, there is no necessity to determine the laminar, transitional, and fully turbulent regimes, as outlined in section 3.2, because the wall jet and external stream flows were both fully turbulent at the inlet in [21] and modelled as such for these simulations. Looking at the streamwise profiles for the U_J/U_S=2.3 case, three major observations are made.

First, at x/h=10, the excess velocity in the wall jet is well defined, whereas at x/h=150, it is much less defined and begins to blend with the free stream flow, as expected in this type of flow configuration. Additionally, the slight wake formed from the splitter plate has only moderate effects on the profile at x/h=10 (an entire magnitude smaller than the wall jet maximum velocity), and at x/h=150, the velocity deficit is still pronounced in the experimental data, but diminished in the RANS simulations. Last, at both locations, the collapse of the wall jet profile is not very well defined. Comparing the turbulence models, it is very clear that the standard k-ε model was the best fit. The profile is almost in perfect agreement with the experimental data at x/h=10, and still very close out at x/h=150. The other models appear to overpredict the maximum velocity of the jet as well as the minimum velocity between the jet and the stream, indicative of a larger effect of the splitter plate's wake.

Turning attention to the U_J/U_S=0.75 case, the first observation made was the much more pronounced effect of the splitter plate wake at x/h=10. This is largely important because in an ideal wall jet-coflowing stream application, no splitter plate would be introduced, and the wall jet would interact with the stream at the instant both flows are combined. Thus, it is difficult to predict the exact form and characteristics of a true wall jet in an external stream, as there is a thin wake layer separating the two. However, the wake layer is almost diminished at x/h=150 for both the experimental data and the simulation data. Additionally, it is noted that the wall jet flow is also enveloped entirely into a boundary layer at x/h=150. As with the U_J/U_S=2.3 case, the standard k-ε model is clearly the best fit, although the major discrepancy between it and the experimental data is the wall-normal location of the jet velocity maximum and minimum at x/h=10. Since the major effect of the coflowing stream on the wall jet in regard to streamwise velocity is the effect on height of the mixing layer [3], [21], this height is an important factor, and it can be seen that the CFD prediction of the maximum and minimum velocities is lower than the

experimental results, suggesting that the waljet is flattened more by the external stream and the mixing layer is lower.

For the U_J/U_S=2.3 case, since the jet maximum velocity is well pronounced, it is suitable to analyze the jet decay rate as it is enveloped in the free stream, seen below in Figure 4.13.

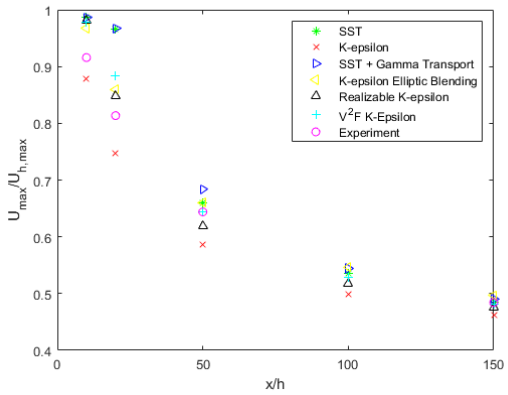

Figure 4.13: Wall Jet in a Co-Flowing Stream (U_J/U_S=2.3) Streamwise Jet Velocity Decay

The notable observation here is that the jet maximum velocity does not appear to decay linearly, as seen both in the experiment and the simulation results. The best fit model for this parameter is very difficult to derive, but it appears that upstream the standard and realizable k-ε models perform the best, and as downstream distance increases, the V^2F k-ε model begins to match the experimental data the best.

While the velocity profiles were in acceptable agreeance, the Reynolds stresses are where the validation case begins to derail. Reynolds stress profiles at x/h=10 and 150 were considered for the U_J/U_S=2.3 & 0.75 cases and can be seen below in Figures 4.14 & 4.15, respectively.

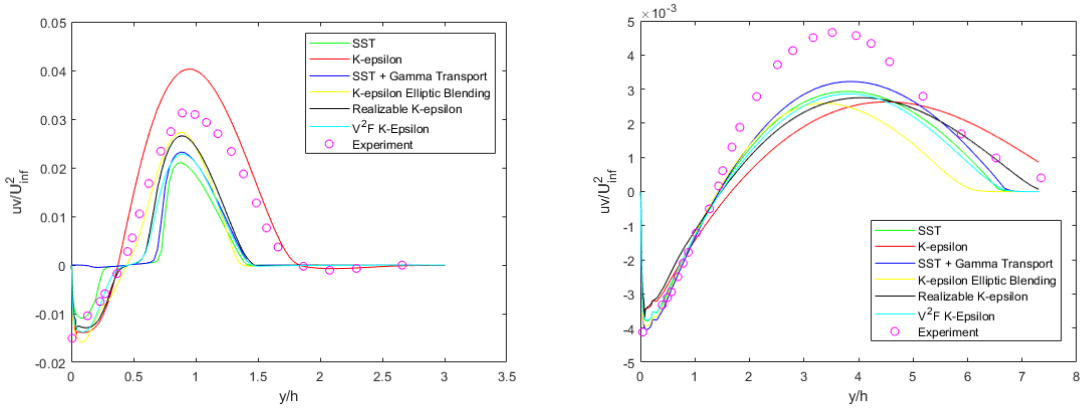

(a) (b)

Figure 4.14: Wall Jet in a Co-Flowing Stream (U_J/U_S=2.3) Reynolds Stress Profiles; (a) *x/h*=10, (b) *x/h*=150

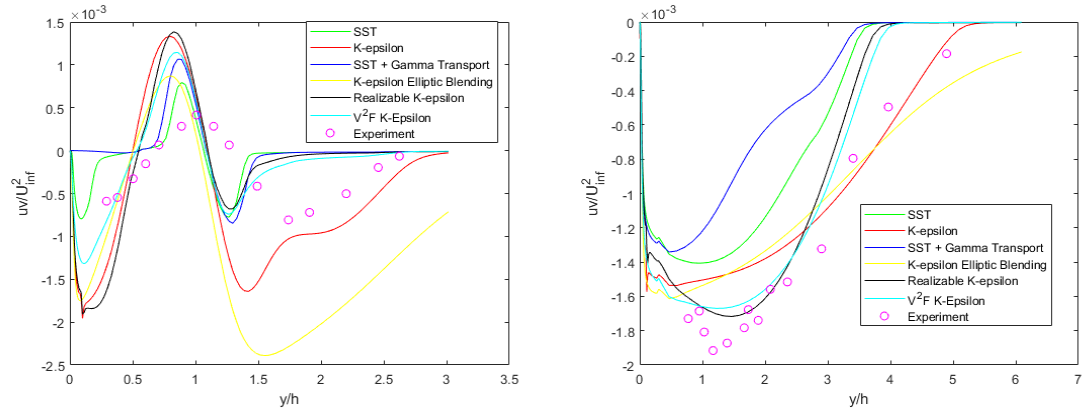

(a) (b)

Figure 4.15: Wall Jet in a Co-Flowing Stream (U_J/U_S=0.75) Reynolds Stress Profiles; (a) *x/h*=10, (b) *x/h*=150

Results for the U_J/U_S=2.3 case were as expected for this flow configuration at *x/h*=10. In accordance with the findings of Eriksson et al. [10] for the wall jet, the distinctive negative dip in Reynolds stresses near the wall followed by the much larger positive profile in the outer boundary layer flow region as well as the free jet region is very clear. However, as this measurement point

is still close to the splitter plate, at which point the external stream was a defined turbulent boundary layer flow, a slightly negative profile should be seen in the wake region caused by the splitter plate and the boundary layer of the external stream. This slight negative dip is seen in the experiment as well as the standard k-ε model, but the remaining models do not become negative again after the positive peak from the jet. At x/h=150, the effects of the splitter plate are largely diminished, and the flow takes on the form of a typical wall jet flow, with the exception of a steep collapse of data as seen in the shear layer of a wall jet. All models follow this trend, but it appears here that they all grossly underpredict the maximum. However, both of the k-ω models appear to follow the profile the best.

For the U_J/U_S=0.75 case, the results are blatantly inaccurate. The experimental data suggests what is expected at both x/h=10 & 150, a negative near-wall region, followed by a positive jet region, followed by another negative region due to the splitter plate and boundary layer profile of the external stream at x/h=10 and a solely negative profile at x/h=150 as the jet is absorbed into the free stream. Reynolds stress profiles for this case are far too misconstrued to select a best fit model at x/h=10, but at x/h=150, the experimental data at inner layer most closely aligns with the realizable k-ε model while the standard k-ε model begins to fit the profile in the outer region.

While no data was available in [21] for near wall measurements, it seemed obligatory to check the near wall behavior of each model. While these results can not be compared to experimental data, they can be compared to each other to ensure that the wall treatment of any single model did not stray from the others. Since these plots were not compared to any validated data and are only representative of model to model agreement, the plots are presented for comparison purposes only.

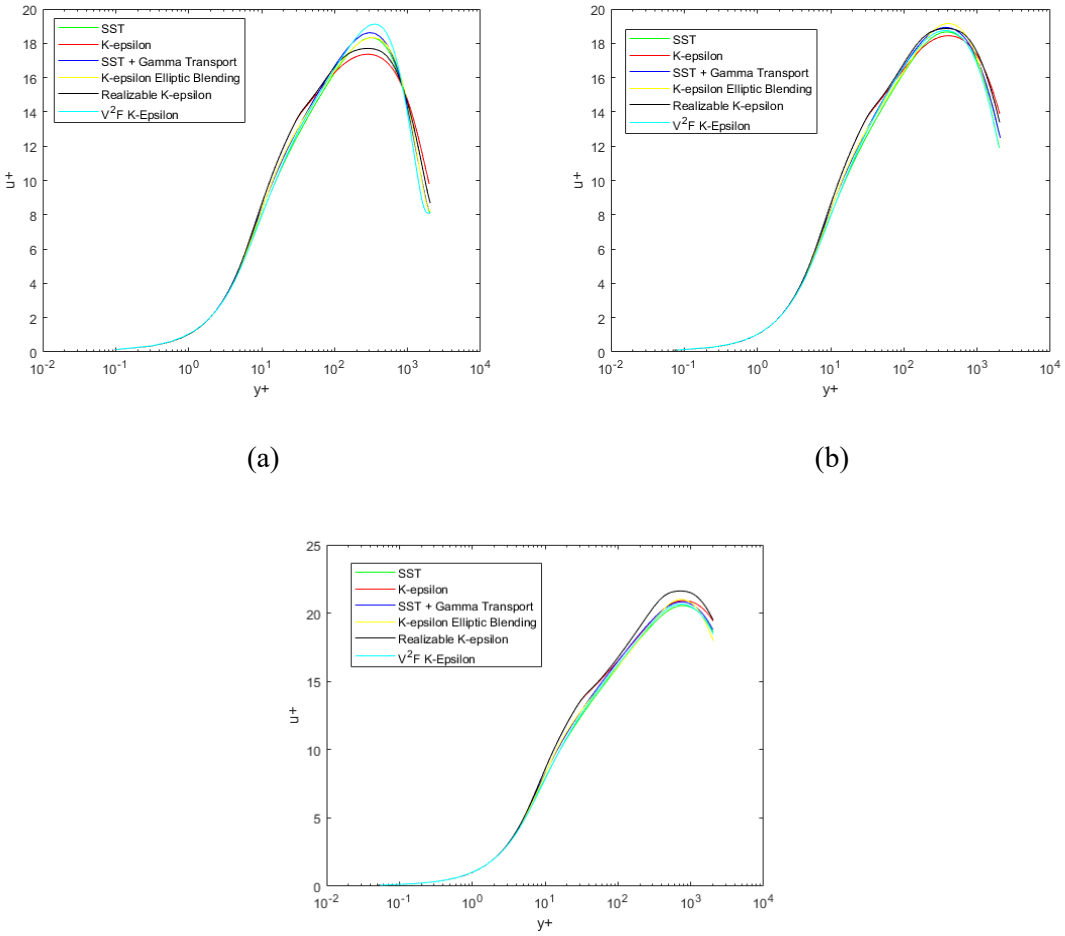

(a) (b)

(c)

Figure 4.16: Wall Jet in a Co-Flowing Stream (U_J/U_S=2.3) Streamwise Velocity Profiles in Inner Scaling; (a) *x/h*=20, (b) *x/h*=50, (c) *x/h*=150

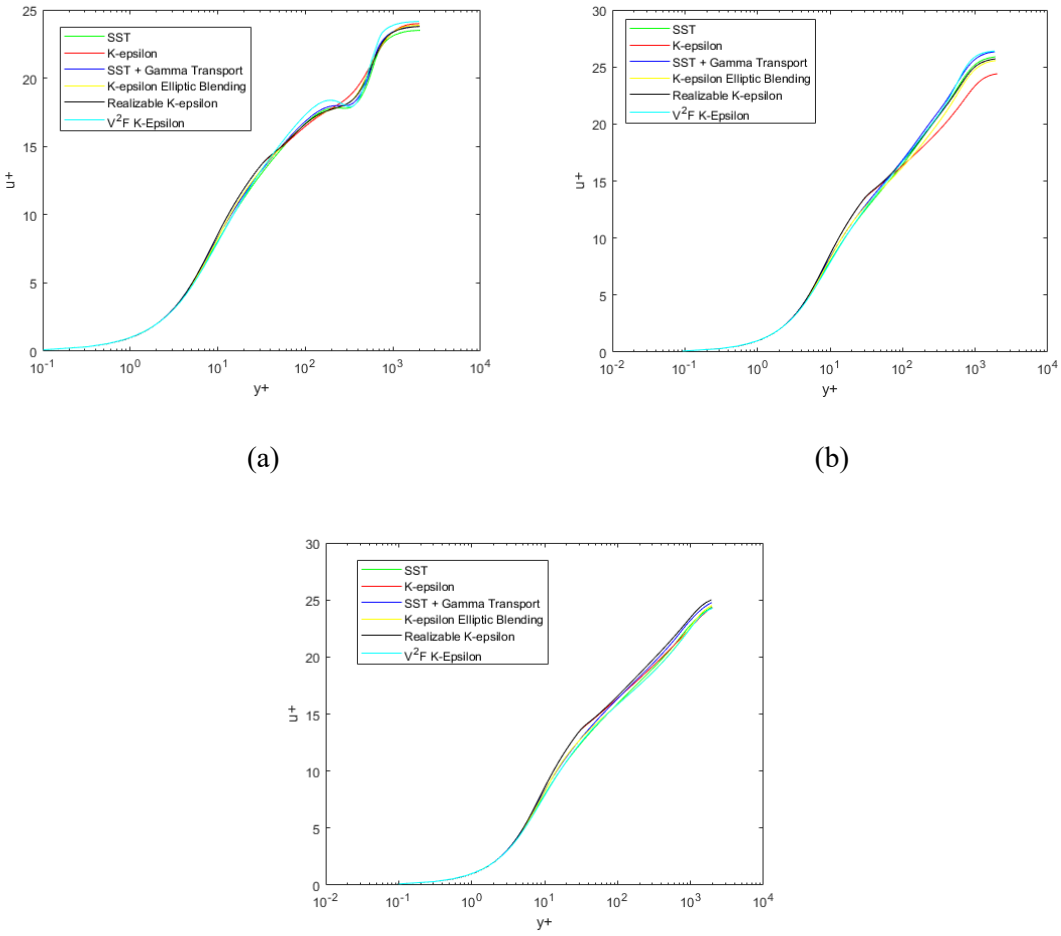

Figure 4.17: Wall Jet in a Co-Flowing Stream (U_J/U_S=0.75) Streamwise Velocity Profiles in Inner Scaling; (a) *x/h*=20, (b) *x/h*=50, (c) *x/h*=150

First, Figure 4.16 shows the inner scaled streamwise velocity profiles for the U_J/U_S=2.3 case, followed by Figure 4.17, showing the same quantity for the U_J/U_S=0.75 case, both at *x/h*=20, 50, and 150. It is seen from the figures that near the wall and extending some way into the boundary layer flow region, all RANS models are in good agreement with each other.

Additionally, the near-wall inner scaled streamwise velocity profiles at *x/h*=20, & 50 were considered (Figures 4.18 & 4.19).

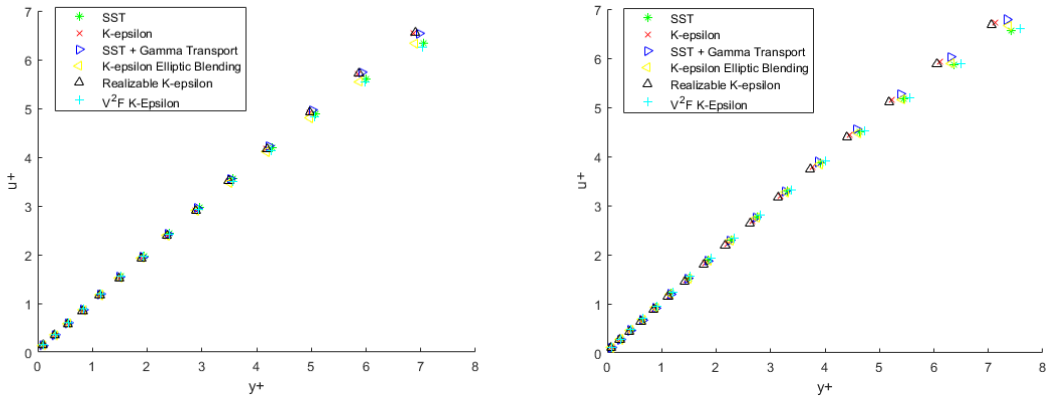

(a) (b)

Figure 4.18: Wall Jet in a Co-Flowing Stream (U_J/U_S=2.3) Near-Wall Streamwise Velocity Profiles in Inner Scaling; (a) *x/h*=20, (b) *x/h*=50

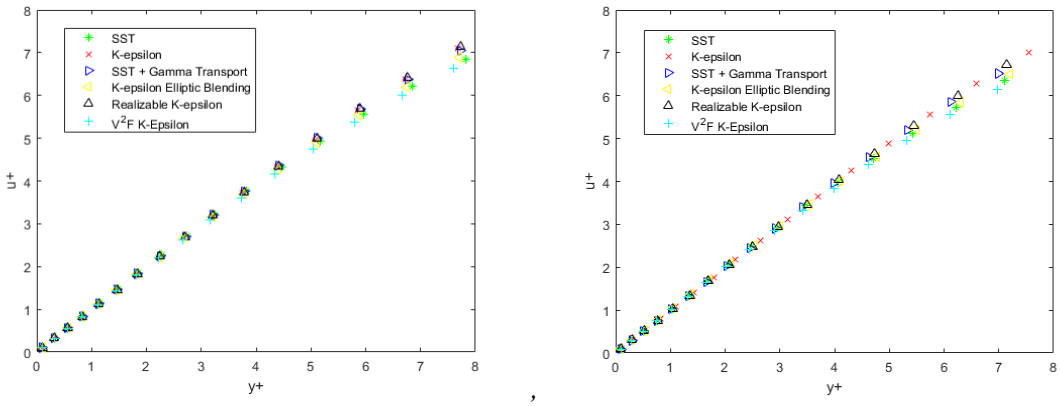

(a) (b)

Figure 4.19: Wall Jet in a Co-Flowing Stream (U_J/U_S=0.75) Near-Wall Streamwise Velocity Profiles in Inner Scaling; (a) *x/h*=20, (b) *x/h*=50

Again, for both cases, the linearity ($u+=y+$) was great up to $y+=\sim3.5$. This is a good indication that the near wall behavior predicted by the models is at least satisfactory. Last, a small log law

window can be seen in the profiles, but this window is not nearly as large as suggested by [21] (no experimental data was presented to support this claim).

4.3: The NASA Hump Wake

All results for the NASA hump wake validation case were taken with respect to [22], citing [16], [17], and [33] as references for experimental data. Data presented shows the velocity profiles across the hump and the downstream separation bubble, Reynolds stress profiles in these locations, skin friction coefficients, and the pressure distribution along the hump and downstream wall. Results for all RANS simulations for these measurements were overall very acceptable. Figure 4.20 below shows the streamwise velocity profiles at x/c=0.65, 0.8, 0.9, 1.0, 1.1, 1.2, & 1.3.

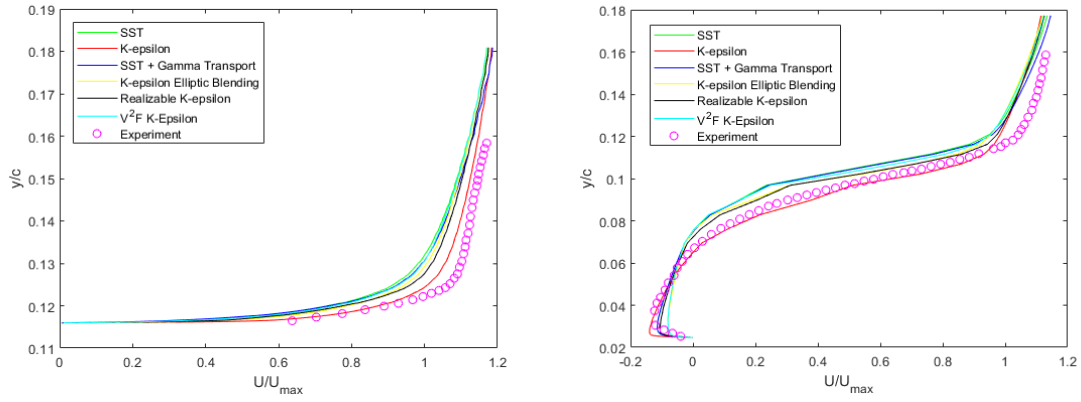

Figure 4.20: Streamwise Velocity Profiles Along the NASA Hump; (a) x/c=0.65, (b) x/c=0.8, (c) x/c=0.9, (d) x/c=1.0, (e) x/c=1.1, (f) x/c=1.2, (g) x/c=1.3

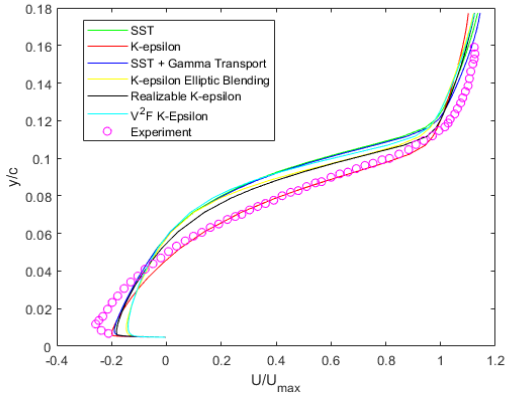

(c)

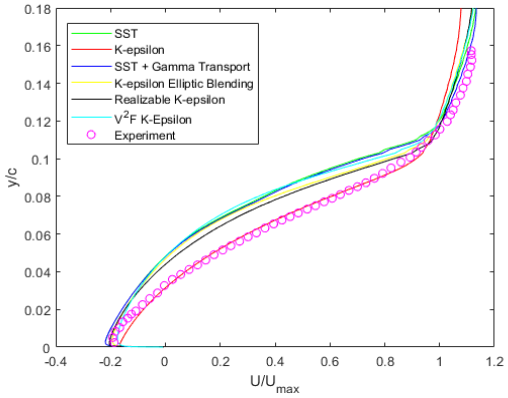

(d)

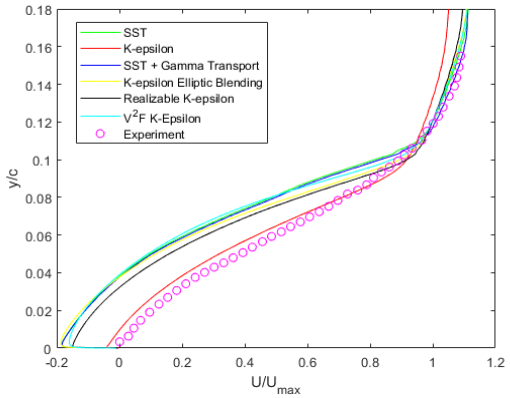

(e)

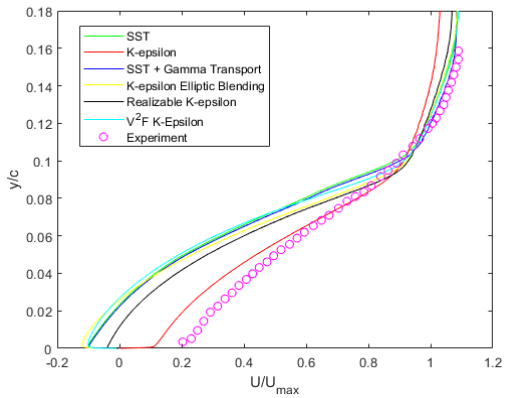

(f)

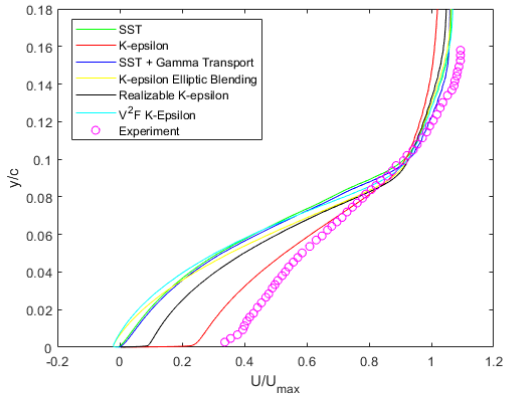

(g)

Figure 4.20 (Continued): Streamwise Velocity Profiles Along the NASA Hump; (a) *x/c*=0.65, (b) *x/c*=0.8, (c) *x/c*=0.9, (d) *x/c*=1.0, (e) *x/c*=1.1, (f) *x/c*=1.2, (g) *x/c*=1.3

Velocity profiles are largely as expected across the hump and immediately downstream. First, it is important to point out that in all plots, the maximum velocity near the free stream is greater than U/U_{inf}=1 because the reference free stream velocity is the unanimous velocity at the inlet, whereas along the hump and upstream the hump a boundary layer flow is forming, causing U_{max} to grow larger than U_{inf}. Regarding the downstream evolution of the hump wake, separation is seen to occur between *x/c*=0.65 & 0.8, as the former profile shows a boundary layer profile and the latter shows a velocity deficit, characteristic of a wake. This deficit is carried all the way to *x/c*=1.1, as shown by the experimental data [16]. The elevation of the maximum velocity deficit is seen to tend to the wall starting at the trailing edge of the hump and attaches to the wall shortly after [16]. At *x/c*=1.1, it is seen that the maximum velocity deficit is 0*m/s*, and from here on, the velocity deficit is positive and increasing toward the freestream velocity, indicating that the flow has become reattached to the wall [16]. At *x/c*=1.3, effects of the wake are still seen in the form of a deficit, but the flow is beginning to regain shape as a boundary layer flow [16]. Inspecting the predictions of the RANS simulations, it is quite clear that the standard k-ε model performed the best by far. However all models showed a higher boundary layer thickness immediately before flow separation, which reflects in the formulation of the downstream profiles, where the velocity deficit is carried higher (normal to the wall) than in the experiment. While the standard k-ε model fits the bulk of the velocity deficit profile very well along the aft side of the hump, it is seen that near the hump wall all of the maximum velocity deficits are increasing positively with respect to downstream distance much faster than the experimental data. This is reversed from the trailing edge of the hump on, as all models tend to lag behind the experimental data in making up the deficit.

Coupled with both the streamwise velocity, separation and reattachment points, determined by locations on the hump and downstream of the hump where τ_w =0, were determined

and shown below in Table 4.2, where separation and reattachment points are non-dimensionalized as *x/c*.

Table 4.2: Separation and Reattachment Points for the NASA Hump Wake

	Separation Length (*x/c*)	% Error (Separation)	Reattachment Length (*x/c*)	% Error (Reattachment)
Experiment	0.665		1.1	
SST k-ω	0.655	1.54%	1.316	19.62%
Standard k-ε	0.659	0.89%	1.147	4.28%
SST k-ω w/ γ Transport	0.655	1.43%	1.310	19.09%
k-ε with Elliptic Blending	0.659	0.89%	1.326	20.58%
Realizable k-ε	0.656	1.32%	1.255	14.08%
V^2F k-ε	0.658	0.99%	1.332	21.11%

From the table, it is seen that all models underpredict the separation point and overpredict the reattachment point, a typical struggle with RANS models [1]. However, the deviation from experimental data for the reattachment length is much further off than that of the separation point. Most notable is the excellent performance of the standard k-ε model, with an error in overprediction of reattachment less than ⅓ of that of the next best (Realizable k-ε) model.

Reynolds stresses at *x/c*=0.65, 0.8, 0.9, 1.0, 1.1, 1.2, & 1.3 were also considered and can be seen below in Figure 4.21.

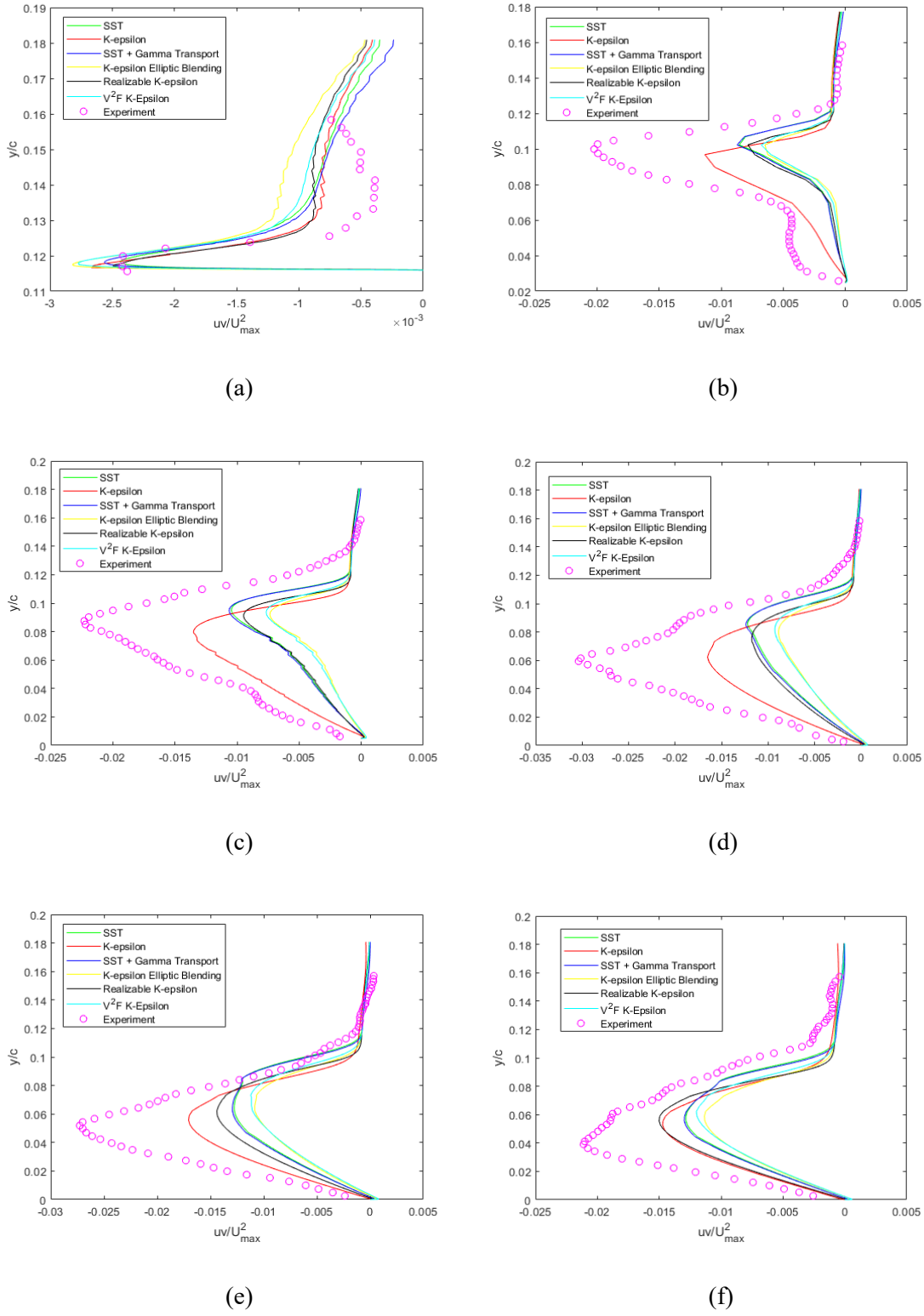

Figure 4.21: Reynolds Stress Profiles Along the NASA Hump; (a) *x/c*=0.65, (b) *x/c*=0.8, (c) *x/c*=0.9, (d) *x/c*=1.0, (e) *x/c*=1.1, (f) *x/c*=1.2, (g) *x/c*=1.3

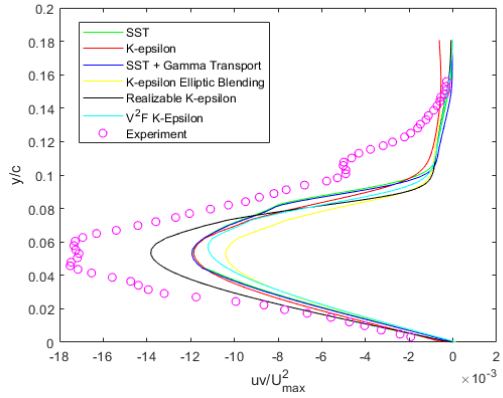

(g)

Figure 4.21 (Continued): Reynolds Stress Profiles Along the NASA Hump; (a) *x/c*=0.65, (b) *x/c*=0.8, (c) *x/c*=0.9, (d) *x/c*=1.0, (e) *x/c*=1.1, (f) *x/c*=1.2, (g) *x/c*=1.3

Reynolds stresses at *x/c*=0.65 are close to typical of those seen in a boundary layer flow for the RANS data, while the experimental data shows a defined 'hook' where the stresses increase positively with increased distance from the wall and then dip the other direction (between *y/c*=0.12 & 016). While it is not mentioned in the paper, this could be a potential effect of the pressure gradient along the hump, as suggested by Fernholz and Warnack [11] who show that the favorable pressure gradient can increase the the peak (referred to here as the hook) of the Reynolds stress profile for a flat plate boundary layer flow. Following this, the Reynolds stress profiles follow with what is expected in a wake flow, where the maximum negative Reynolds stress increases with increased velocity deficit and decreases with decreased velocity deficit. While all models underpredicted this maximum Reynolds stress deficit, the standard k-ε model appears to most closely reach this maximum across the hump and following downstream.

Pressure coefficient along the hump wall was also extracted from the experimental data and simulations. Pressure coefficient was defined as seen below in Equation (4.3).

$$C_P = \frac{(P - P_{Ref})}{0.5\rho U_{Ref}} \tag{4.3}$$

Results can be seen below in Figure 4.22.

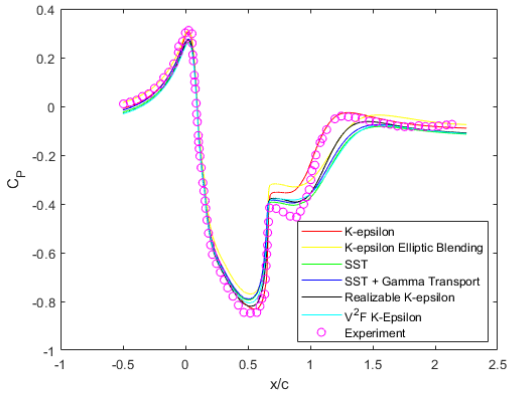

Figure 4.22: Pressure Coefficient Distribution Along the NASA Hump

The pressure distribution shows a slight adverse gradient immediately before the hump (there is a slight deceleration along the wall found here [16]), which then becomes a positive gradient all the way to about *x/c*=~0.55 to 0.65, where pressure begins to increase, shortly thereafter the flow separated. All models predicted the pressure distribution well, with the exception of an over-relaxed adverse gradient starting at the trailing edge of the hump and moving downstream to the reattachment point.

Last, the skin friction coefficient (Calculated as seen below in Equation (4.4)) was looked at for the hump wake. Results of skin friction predictions and experimental measurements can be seen below in Figure 4.23.

$$C_f = \frac{\tau_w}{0.5\rho U_{Ref}^2} \tag{4.4}$$

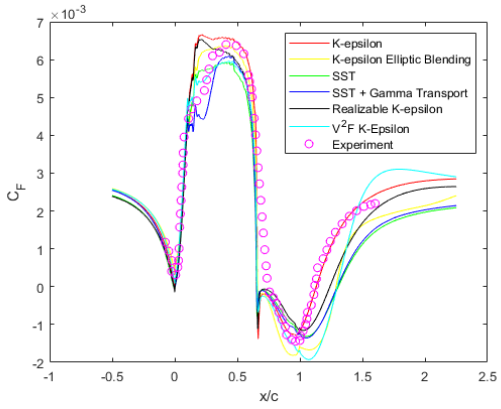

Figure 4.23: Skin Friction Along the NASA Hump

One observation is that the skin friction coefficient dips very abruptly for all models at the separation point, while the experimental data does not suggest this. However, it is seen from that point on all models seem to regroup and conform with the experiment over the rest of the hump. From the trailing edge on, the standard k-ε model fits the experimental data almost perfectly.

4.4: Selection of the Best Fit Model

The four validation cases presented numerous challenges for the models, including flow separation and reattachment (wall-wake flows), boundary layer flows, mixing layer flows, and free shear jet flows. In order for the selected turbulence model to accurately predict the wall-jet hump-wake flow configuration, the model must produce reasonable results for all of these challenging flows, as these are the expected flows that are combined in the wall-jet hump-wake. Selection of the best fit model was based on each model's ability to reproduce velocity profiles, Reynolds stresses, pressure coefficients, and skin friction coefficients for the flow conditions above. In short, the standard k-ε model was selected as the overall best fit. A detailed analysis on the selection process can be found in this section.

Perhaps the best validation case to compare the boundary layer flow, the free jet flow, and the laminar to turbulent transition is the wall jet case. From a thorough review of section 4.1, it

was clear that the standard k-ε model was most suitable for the laminar to turbulent transition. While the Reynolds stresses leaned more toward the SST k-ω model, it was decided that proper velocity distribution in the developing regime was most important, as this will be a defining factor in the evolution of the wall-jet hump-wake configuration.

In regard to the boundary layer flow, all models performed very well near the wall. Overall, the decision was between the k-ε and SST k-ω models, as the former performed almost perfect in the developing regime in respect to the streamwise velocity evolution, while the latter performed the best in the fully turbulent regime.

The free jet flow was the least important factor in this section, as the jet flow in the wall-jet hump-wake configuration will be affected largely by an adverse pressure gradient near the slot and develop more as a mixing layer than a free shear flow. However, it was determined that both the SST k-ω and standard k-ε models performed best in this category, mainly with respect to streamwise and wall-normal velocity profiles in the fully turbulent regime.

Since the wall jet in a co-flowing stream validation case in section 4.2 was overall poor, it will only be considered for the mixing layer flow configuration. Unfortunately, as discussed above, this is a very large parameter influencing the evolution of the wall jet for the wall-jet hump-wake flow configuration. For both cases, the standard k-ε model predicted the closest results for streamwise velocity profiles, but for the U_J/U_S=0.75 case, even this model could not accurately predict the wall-normal location of the jet maximum velocity and maximum wake velocity deficit, which in turn means that the position of the mixing layer was not correctly predicted. The SST k-ω model predicts the best results for the downstream Reynolds stress profiles, but other than this, the standard k-ε model was the best fit.

The obvious most important flow parameter of the hump wake validation case was the wake, and in turn the separation and reattachment, including the recirculation zone in between.

For flow separation and reattachment points, the standard k-ε model performed astoundingly well and was far better than the other models. This is also evident in the velocity profiles and Reynolds stress profiles, where the standard k-ε model outperformed the others in accuracy, making it the overall best fit model for this configuration.

CHAPTER 5: SIMULATION PARAMETERS & SETUP FOR THE WALL-JET HUMP-WAKE

Upon successful validation of the standard k-ε turbulence model for the prescribed validation cases, the wall-jet hump-wake flow configuration was set up. The variable parameters of the model were selected in accordance with the discussion for vehicle body modeling in section 1.2. It was decided that a total of nine simulations were to be constructed and executed, each varying jet slot height (vehicle ride height), jet discharge velocity, or both, with additional simulations run if deemed necessary. This chapter covers in detail parameter selection for each configuration as well as the simulation setup for all.

5.1: Parameter Selection

Simulations for the wall-jet hump-wake were set up using the NASA hump wake as the wake generator. The baseline jet slot height was chosen to be 10% of the hump height, h_b=0.00537m. Additionally, jet slot heights of 15% (0.008055m) and 5% (0.002685m) of the hump height were considered. The inlet velocity was selected as 34m/s, close to the simulation velocity for the hump wake, yielding a Reynolds number based on chordlength of 911,500. For the jet velocity, ratios of U_J/U_S=1:1 (referred to as $U_{J,b}$), 2:1, and 0.5:1 were considered.

For simplicity, each case was labeled as seen below in Table 5.1, where the letters denote the specific slot height and accompanying numbers denote the velocity ratio. Cases will be referred to as such for the duration of this work.

Table 5.1: Wall-Jet Hump-Wake Case Number Identification

Case #	A0.5	A1	A2	B0.5	B1	B2	C0.5	C1	C2
Jet Height	$0.5h_b$	$0.5h_b$	$0.5h_b$	h_b	h_b	h_b	$1.5h_b$	$1.5h_b$	$1.5h_b$
Jet Velocity	$0.5U_{J,b}$	$U_{J,b}$	$2U_{J,b}$	$0.5U_{J,b}$	$U_{J,b}$	$2U_{J,b}$	$0.5U_{J,b}$	$U_{J,b}$	$2U_{J,b}$

Reynolds number for each simulation based on jet inlet slot height and velocity are shown below in table 5.2.

Table 5.2: Reynolds Numbers for Wall-Jet Hump-Wake Simulations

Case #	A0.5	A1	A2	B0.5	B1	B2	C0.5	C1	C2
Re	2,913	5,827	11,654	5,827	11,654	23,309	8,740	17,481	34,963

5.2: Simulation Setup

For all nine simulations, the domain size, mesh refinements, and prism layer extrusions were all generated in accordance with the validation case simulations. For all hump wake related refinements, the scaling parameter is chordlength c=0.420m and for all wall jet related refinements the scaling parameter is slot height h, which varies from case to case. The domain extends 10c upstream of the hump's leading edge and 70c downstream of the trailing edge, to match the downstream length of the hump wake validation case. This downstream length is 3,650h downstream of the jet slot for the highest slot used, which is well over the domain length of 730h used for the wall jet in a co-flowing stream validation case. The wall-normal domain size is 2.9c, or 152h for the highest jet slot. This is matching the domain height for the wall jet in a co-flowing stream case, which was 152h. The incoming wall (upstream of the leading edge of the hump) was modelled as a viscous wall. The boundary conditions for the wall-jet hump-wake simulations can be seen in the appendix as Table A.4.

The mesh was generated as a blend of the meshes for the wall jet validation case and the hump wake case. The final meshes for the h=0.5h_b, h_b, & 1.5h_b cases were 2,894,404, 2,936,740, and 3,097,658 cells, respectively. The base size was 0.01875c, which is the same as the base size for the hump wake validation case. For the hump wake, the same volume source refinements and

surface control along the hump were used as with the validation case. A representative zoomed mesh scene showing the hump for case B1 can be seen below in Figure 5.1.

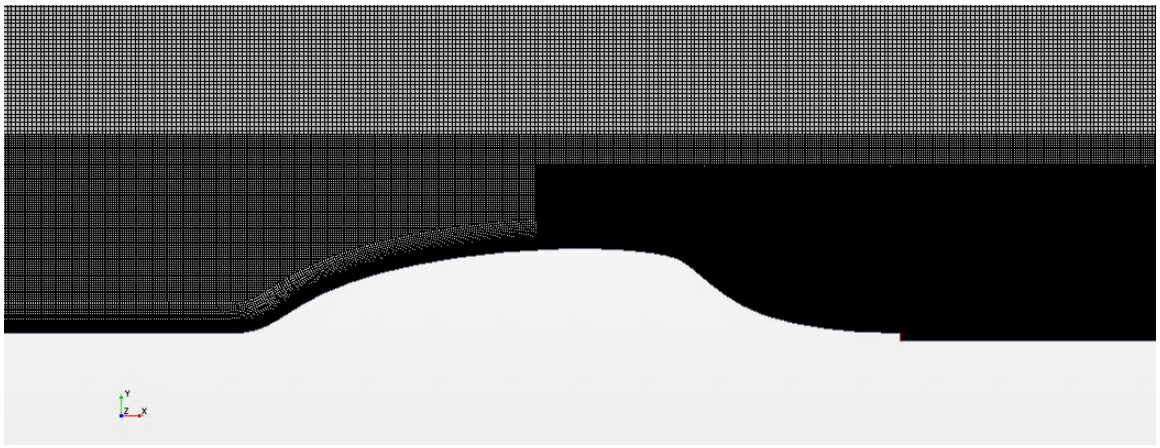

Figure 5.1: Zoomed Wall-Jet Hump-Wake Case B1 Mesh Highlighting Wake Near Refinements

For the wall jet, only two refinements were needed. The first refinement extended 10*h* downstream of the jet, 2*h* upstream, and was 5*h* high. Cells in this zone were 0.039*h,* identical in size to the nearest refinement for the wall jet validation case. The next refinement for the wall jet extended 8*h* upstream of the jet, 40*h* downstream, and 6*h* high. Cells in this zone were 0.0782*h*, matching the cell size in the refinement zone immediately after the nearest in the wall jet validation case. The other refinements in the wall jet case, including the shear layer refinement, were not included here, as it was found that all refinements were contained inside the nearest wake refinement zone, which has a smaller cell size. A representative zoomed mesh scene showing the nearest zone of the wall jet refinement for case B1 can be seen below in Figure 5.2.

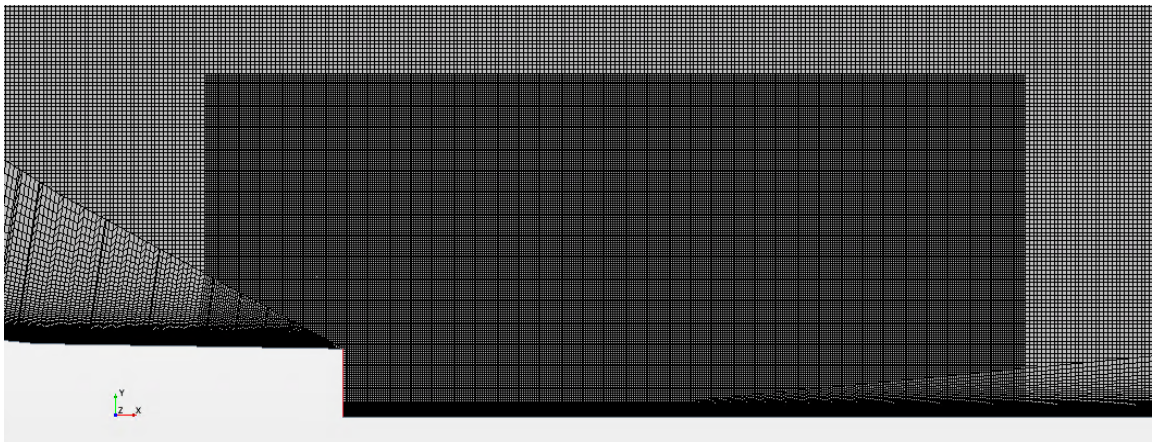

Figure 5.2: Zoomed Wall-Jet Hump-Wake Case B1 Mesh Highlighting Wall Jet Near Refinement

Prism layers were separated into 3 regions for the wall-jet hump-wake simulations. The first region started at the simulation freestream inlet and extended to x/c=0.45 downstream of the leading edge of the hump. Here, the total prism layer height was 0.0476c with a total number of 88 layers and a stretch factor of 1.12. The next set of prism layers started at x/c=0.45 and extended to x/c=1, with a total height of 0.0719c, 92 layers, and a stretch factor of 1.112. The last set of prism layers started at x/c=1 and extended to the far end of the domain. The prism layer total height for each jet slot height was 1h and all three had a total number of 60 layers. Stretch factors for cases A0.5-A2, B0.5-B2, and C0.5-C2 were 1.130, 1.143, and 1.153, respectively

All wall-jet hump-wake simulations were run with air as the working fluid and a turbulence intensity of 0.1%. After creating each simulation, an initial run of each was done to check wall $y+$ values along the entire bottom of the domain. Values at selected measurement points can be seen below in Table 5.3.

Table 5.3: Wall $y+$ Values for Wall-Jet Hump-Wake Simulations

	A0.5	A1	A2	B0.5	B1	B2	C0.5	C1	C2
x/c	Wall $y+$	Wall $y+$	Wall $y+$	Wall $y+$	Wall $y+$	Wall $y+$	Wall $y+$	Wall $y+$	Wall $y+$
0.65	0.1187	0.1168	0.1213	0.1215	0.1207	0.1234	0.1230	0.1222	0.1254
0.8	0.0405	0.0387	0.0418	0.0437	0.0433	0.0446	0.0490	0.0486	0.0503
0.9	0.0612	0.0584	0.0612	0.0616	0.0614	0.0614	0.0614	0.0614	0.0612
1.0	0.2880	0.4733	0.7802	0.2893	0.4734	0.7801	0.2881	0.4735	0.7801
1.1	0.0612	0.1136	0.2151	0.0629	0.1149	0.2164	0.0630	0.1174	0.2184
1.2	0.0766	0.0885	0.1911	0.0840	0.1124	0.2035	0.0823	0.1127	0.2052
1.3	0.0867	0.0814	0.1631	0.0916	0.1109	0.2011	0.0919	0.1112	0.1985
1.4	0.0912	0.0814	0.1465	0.0922	0.1013	0.1765	0.0912	0.1081	0.1885
1.5	0.0925	0.0824	0.1354	0.0941	0.1017	0.1766	0.0903	0.1083	0.1929
2.0	0.0897	0.0854	0.1105	0.0913	0.0934	0.1405	0.0895	0.0971	0.1618
2.5	0.0902	0.0866	0.1020	0.0903	0.0920	0.1246	0.0892	0.0930	0.1406
3.0	0.0865	0.0865	0.0965	0.0846	0.0855	0.1143	0.0843	0.0890	0.1277

While the values seen above aren't bounded as tightly as seen in the validation case meshes, values are still within a satisfactory range ($1.0<y+<0.01$). Considering the lack of validation for the wall-jet hump-wake configuration, it was inherent that a mesh sensitivity study be carried out. This study only used one configuration, case A0.5, considering the mesh for all cases was identical with the exception of larger scaled wall jet volume refinements for cases B0.5-B2 and cases C0.5-C2. This sensitivity study covered pressure coefficient variations, drag coefficient variations, skin friction coefficient variations, and variations in the streamwise velocity profiles at selected locations for three different grids: a coarse mesh containing 2,361,872

cells, a medium mesh containing 2,537,751 cells, and a fine mesh (used for the final simulations) containing 2,894,404 cells. Drag coefficient variation can be seen below in Table 5.4, followed by skin friction and pressure coefficients in Figures 5.3 and 5.4, respectively.

Table 5.4: Drag Coefficient Variation With Varying Grid Sizes

	Fine	Medium	Coarse
C_D	0.1694	0.1693	0.1693

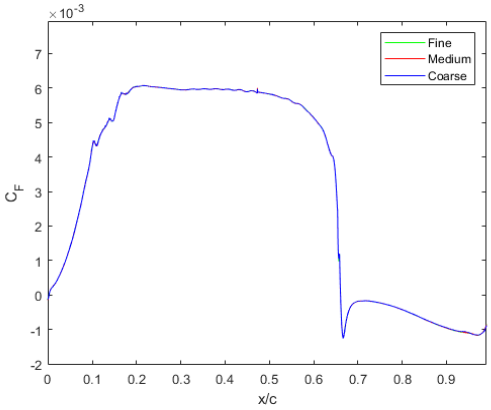

Figure 5.3: Skin Friction Coefficient Variation With Varying Grid Sizes

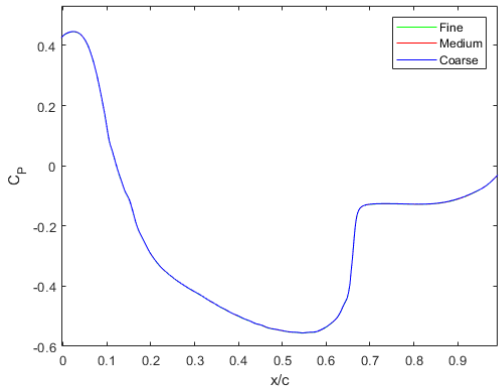

Figure 5.4: Pressure Coefficient Variation With Varying Grid Sizes

Additionally, Figure 5.5 shows variation in streamwise velocity predictions at selected critical locations.

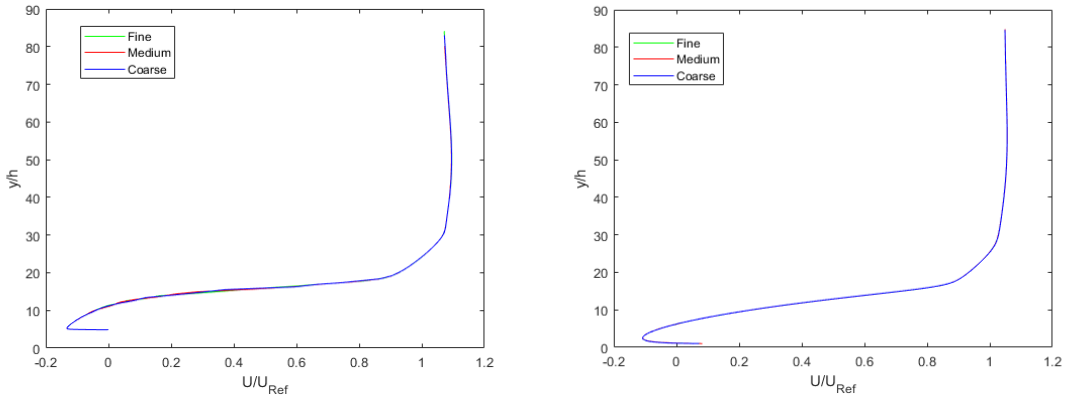

(a) (b)

Figure 5.5: Streamwise Velocity Variation With Varying Grid Sizes; (a) *x/c*=0.8, (b) *x/c*=1.0, (c) *x/c*=1.2, (d) *x/c*=1.4, (e) *x/c*=2

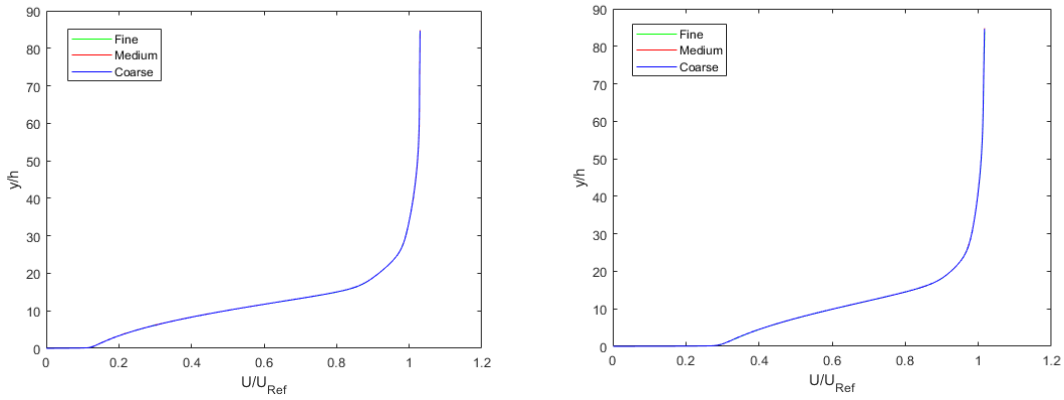

(c)

(d)

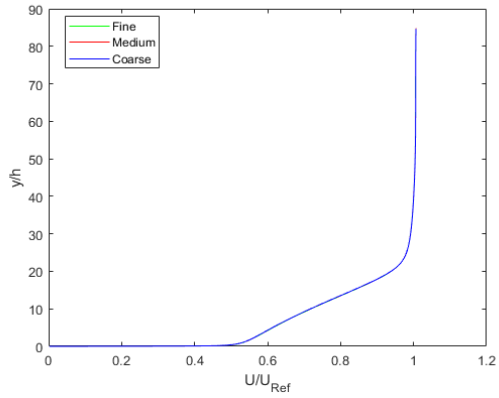

(e)

Figure 5.5 (Continued): Streamwise Velocity Variation With Varying Grid Sizes; (a) *x/c*=0.8, (b) *x/c*=1.0, (c) *x/c*=1.2, (d) *x/c*=1.4, (e) *x/c*=2

It is clear from the above plots and drag values that mesh independence has been very well achieved, as the results are all nearly identical. Considering the quality wall *y*+ values and excellent proof of mesh independence, it is assumed that the mesh has been refined to a point where numerical error due to the generated grids is expected to be low, and the accuracy of results is largely only limited by shortcomings of the standard k-ε model.

CHAPTER 6: WALL-JET HUMP-WAKE RESULTS & DISCUSSION

The wall-jet hump-wake final simulation results are reviewed and discussed in this chapter. Results include velocity profiles for all nine cases along with Reynolds stresses to provide a basic understanding of the flow field as well as to uncover basic observations and differences between cases. Additionally, an initial evaluation of the separation bubble for all nine cases will be conducted. A thorough investigation is conducted to identify sources for trends found via flow field visualization of the recirculation zone. Last, drag values for the hump body in each case are calculated along with pressure coefficient distribution and skin friction coefficient distribution. The wall-normal measurement planes, scaled by chordlength c, span from $0.65c$ to $1.5c$ in increments of $0.1c$ with additional points at $0.65c$, $2.0c$, $2.5c$, and $3.0c$ as well as select points upstream of $0.65c$ for incoming flow conditioning only. Results presented in this chapter are limited to only important figures that represent the major flow characteristics of this configuration. The remaining plots and figures can be found in the appendix.

6.1: Inflow Conditions

Before conducting a thorough review of the final wall-jet hump-wake simulations, it is important to check the incoming flow between all cases to ensure consistency and that no large discrepancies are present. For this validation, velocity profiles between all cases are checked and compared. Figure 6.1 below shows the evolution of the velocity profile from x/c= -3 to 0.

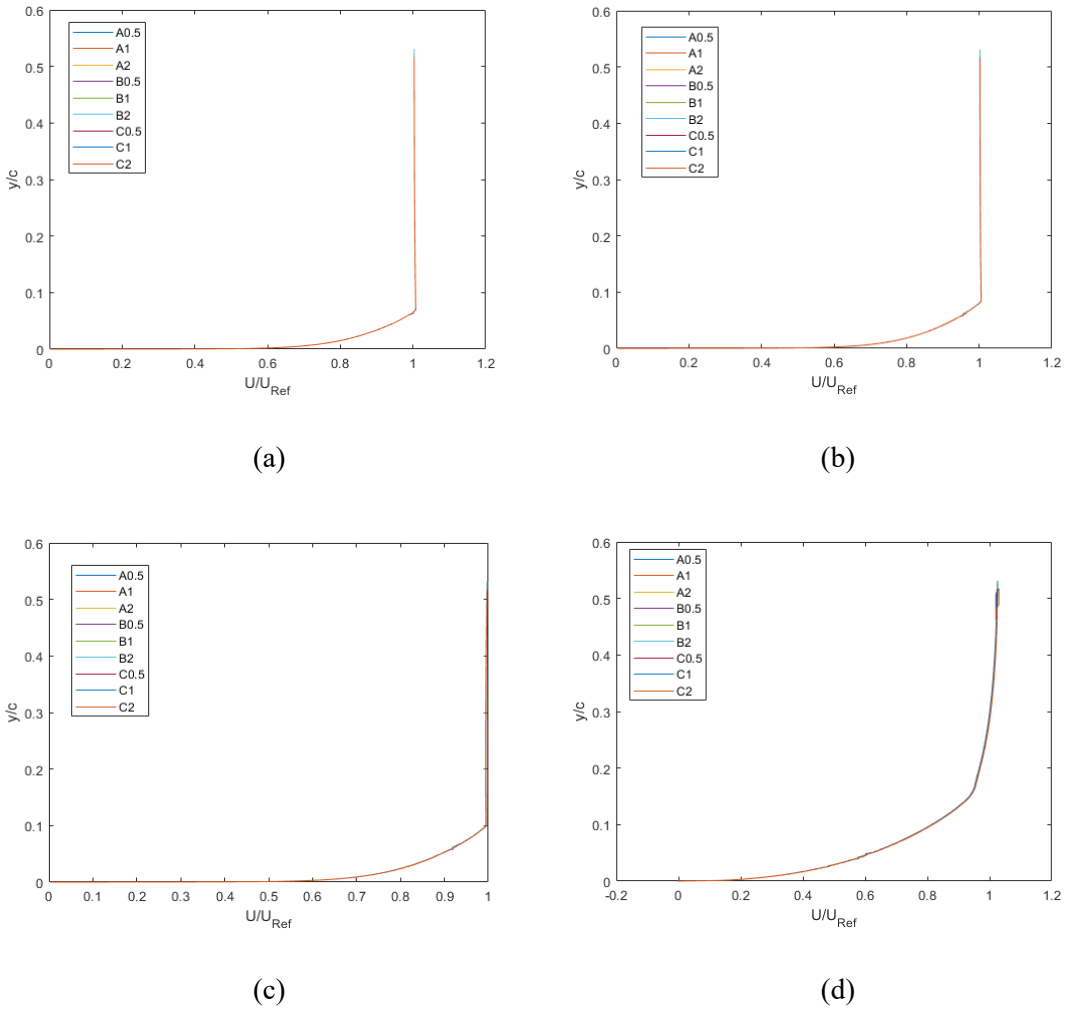

Figure 6.1: Streamwise Velocity Profiles from *x/c*= -3 to *x/c*=0; (a) *x/c*= -3, (b) *x/c*=-2, (c) *x/c*=-1, (d) *x/c*=0

The above plots show that the cases are all in good agreement with each other, which indicates near-constant predictions of inflow conditions between all simulations and eliminates sources of error due to external stream invariance for the incoming flow. Additionally, it is noted that a fully turbulent incoming boundary layer is achieved somewhere well before *x/c*= -3.

6.2: Wall-Jet Hump-Wake Velocity Profiles

To begin dissection and review of the wall-jet hump-wake flow configuration, a review of the wall-jet hump-wake velocity field is conducted in this section to provide a general picture of the flow field and effects of the wall jet variations. Since the flow was measured to be separated at x/c~0.66 for the hump wake [16], the velocity field before this point, at x/c=0.5, was checked as an early indication of whether or not the varying wall jet has any effect on the flow upstream of the separation point (Figure 6.2).

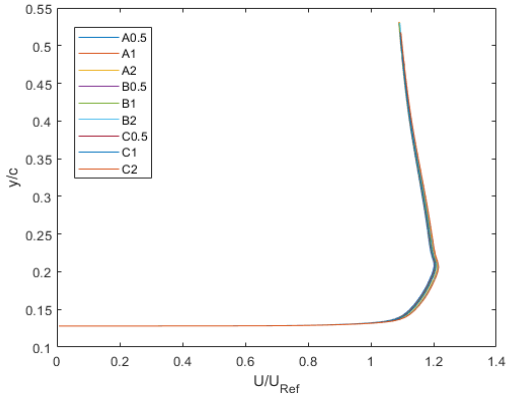

Figure 6.2: Streamwise Velocity Profiles at x/c=0.5

While the profiles are mainly consistent with each other, some deviance can be seen near the wall. Figure 6.3 shows a closer look at the flow in the boundary layer.

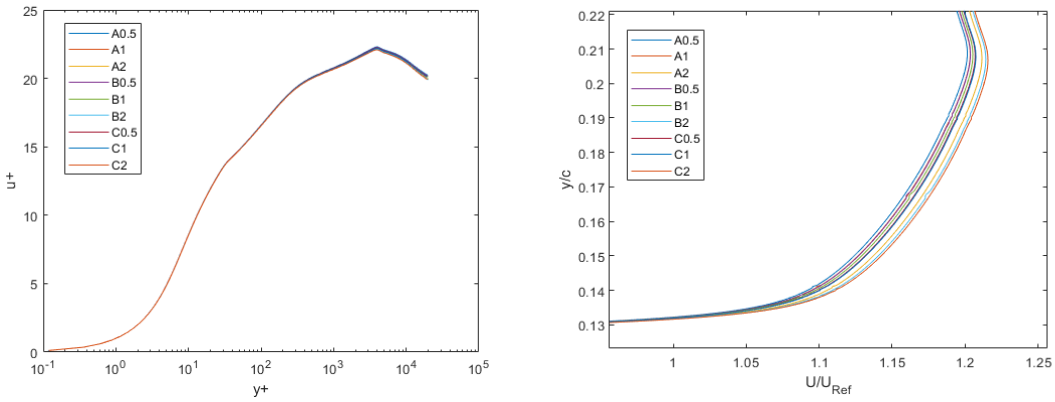

(a) (b)

Figure 6.3: Detailed Streamwise Velocity Profiles at *x/c*=0.5; (a) Inner Scaling, (b) Zoomed Outer Scaling

Two observations are made from Figure 6.3. First, it is seen that deviation is not seen until the outer wake region of the boundary layer flow (6.3a), and second it is seen that an organized trend is forming in the velocity field (6.3b). With respect to raising the jet velocity, it can be seen that a higher jet velocity increases the streamwise velocity along the top of the hump. This trend is also followed for raising the jet slot height. Both of these trends can potentially be analogous with a delayed separation point, which will be investigated later on in Section 6.3. The next measurement point is at *x/c*=0.65, immediately before the separation point measured by [16] for the hump wake. The streamwise velocity profiles here can be seen below in Figure 6.4.

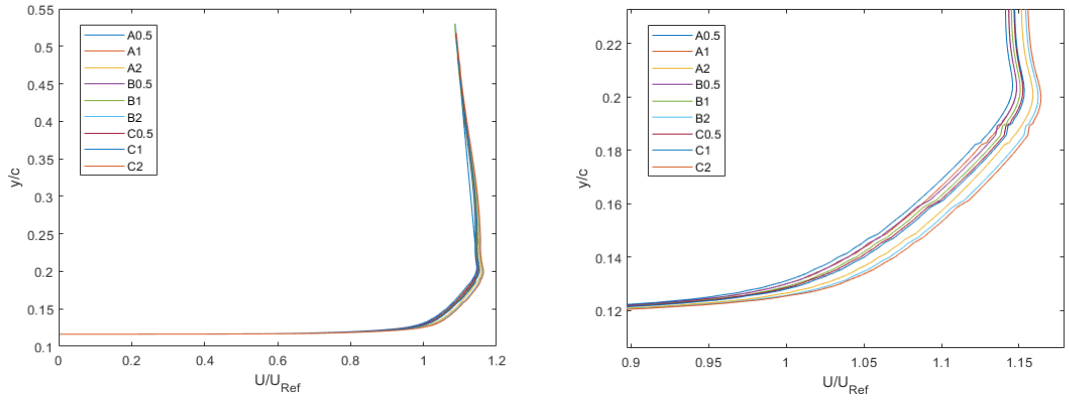

Figure 6.4: Detailed Streamwise Velocity Profiles at *x/c*=0.65; (a) Full Profile, (b) Zoomed

It can be seen at *x/c*=0.65 that the same trend is observed as at *x/c*=0.5, but the variations are becoming more distinct. Additionally noted is that the flow has not yet separated for any of the cases. Thus, it is concluded that an increase in wall jet slot height and velocity results in a higher velocity gradient across the hump leading up to the point of separation.

The next regime examined is the separated turbulent wake region along the aft portion of the hump. Velocity profiles from here to the end of the sampled domain are scaled using outer variables for all cases and separated into two categories based on wall jet slot height and wall jet velocity. For the wall jet slot height groupings, all *y* coordinates were scaled by slot height, *h*. For velocity ratio groupings, *y* coordinates were scaled by *c* and plots were offset such that *y/c*=0 coincides with the top of each wall jet slot (the *y* coordinate of the trailing edge of the hump). Figure 6.5 shows the streamwise velocity profiles at *x/c*=0.8, 0.9, and 1.0, grouped by *h* for cases B0.5-B2.

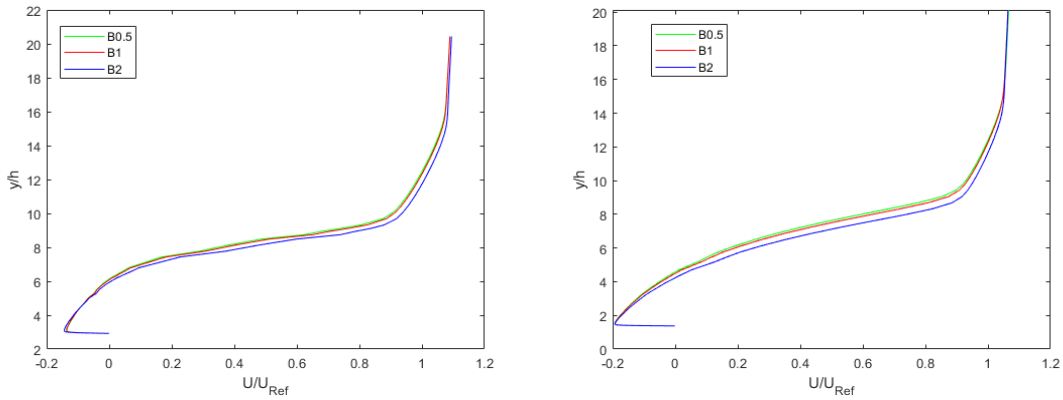

(a) (b)

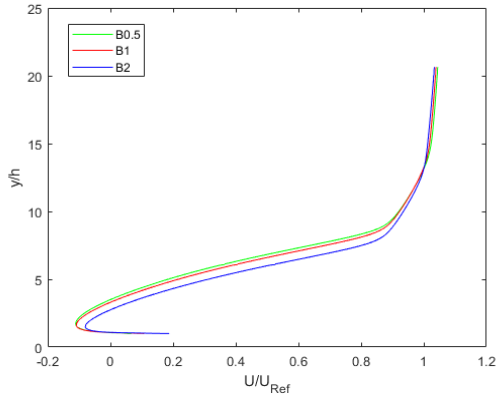

(c)

Figure 6.5: Wall-Jet Hump-Wake Velocity Profiles for Cases B0.5.-B2; (a) *x/c*=0.8, (b) *x/c*=0.9, (c) *x/c*=1.0

The plots above show very similar results, but they are not in perfect agreement. It is seen above that the outer layer of the wall-wake here becomes closer to the wall with increased wall jet velocity. This finding also becomes amplified as the wake nears the wall jet at the trailing edge.

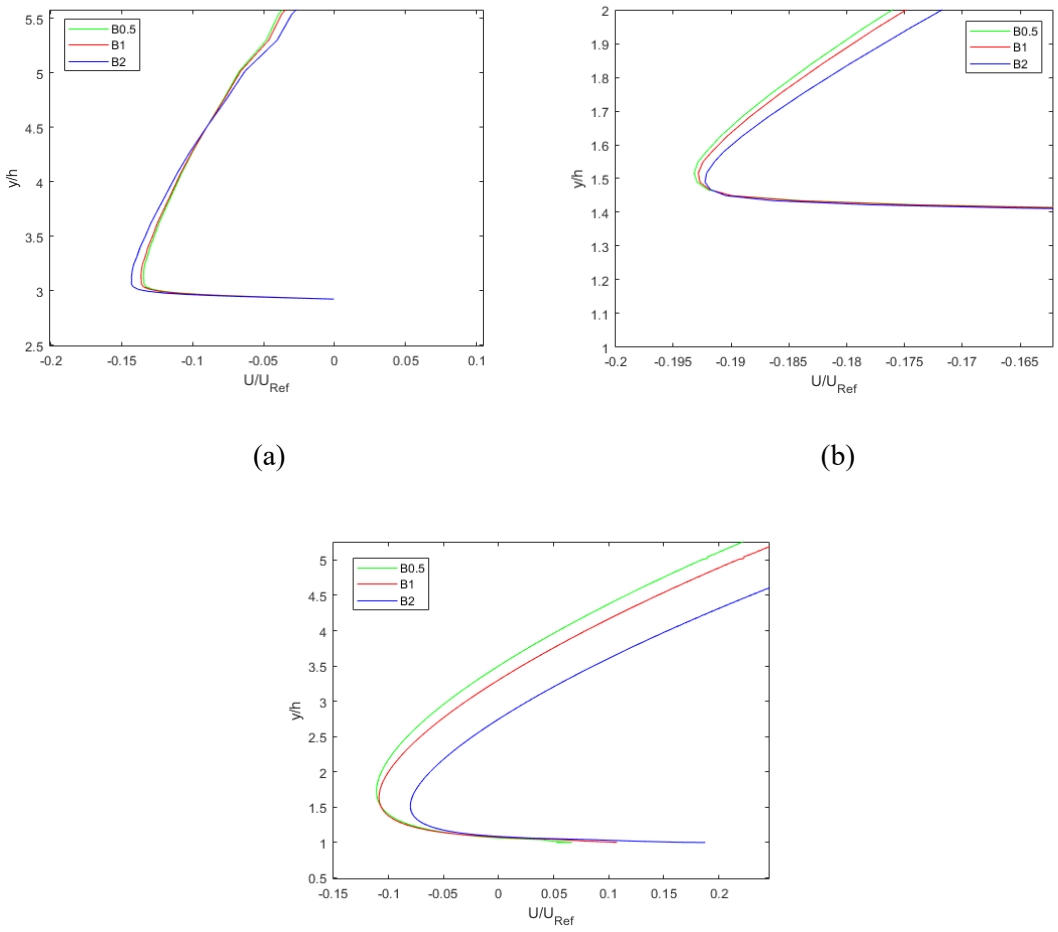

Figure 6.6: Zoomed Wall-Jet Hump-Wake Velocity Profiles Grouped by *h* for Cases B0.5-B2; (a) *x/c*=0.8, (b) *x/c*=0.9, (c) *x/c*=1.0

Another note on the wake velocity profile evolution, visualized in Figure 6.6 above, is that the wake appears to be more intense upstream but recovers faster with respect to increasing downstream distance for a higher wall jet velocity. At the trailing edge of the hump, the smallest deficit is seen with the highest wall jet velocity, while the largest deficit is seen with the lowest wall jet velocity. In regards to the effects of varying slot height, cases A1, B1, & C1 will be used.

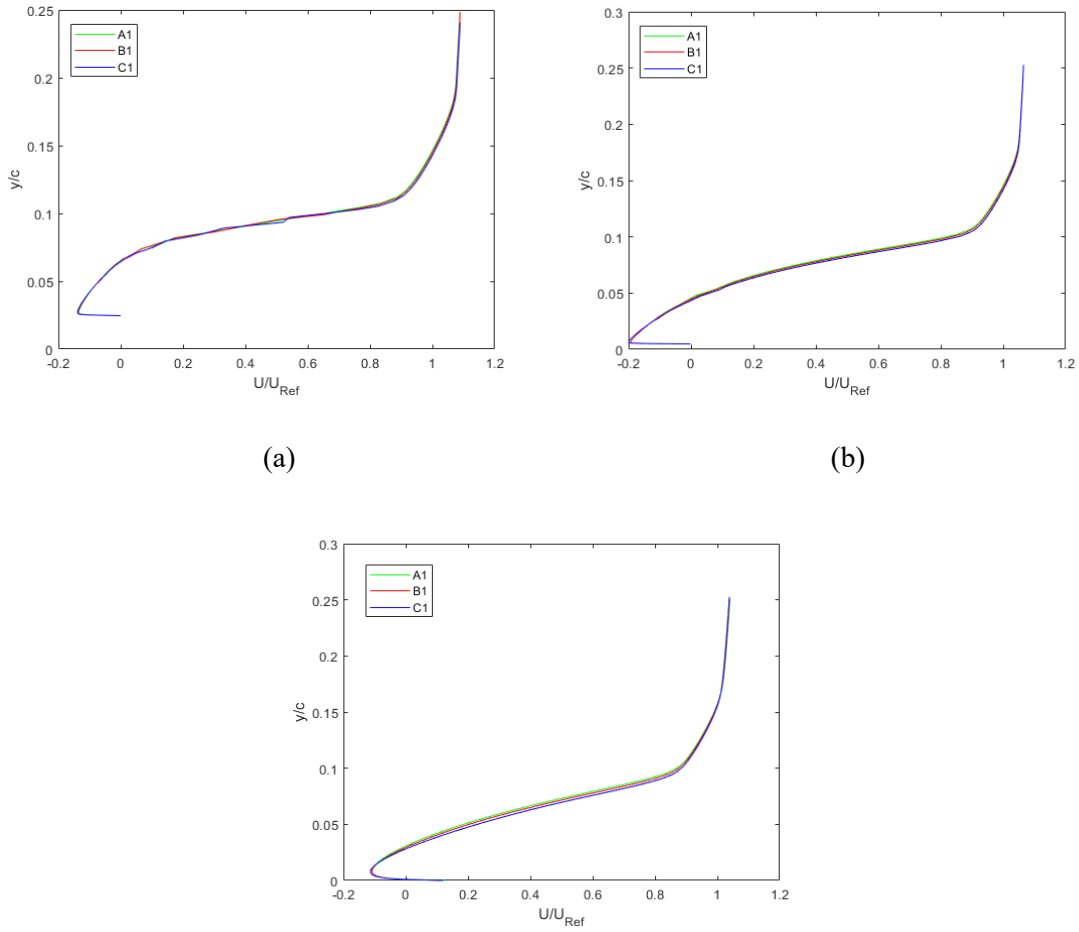

Figure 6.7: Wall-Jet Hump-Wake Velocity Profiles Grouped by U_J/U_S for Cases A1, B1, & C1; (a) x/c=0.8, (b) x/c=0.9, (c) x/c=1.0

The above plots in Figure 6.7 show the same trends for increasing wall jet slot height as seen with increase of wall jet velocity. For increasing h, the outer layer of the wake is closer to the wall, similar to increasing U_J/U_S. However, differences in the maximum velocity deficit at these points are hardly present. All of this leads to the conclusion that for an increase in slot height or an increase in the wall jet's velocity, the overall size of the recirculation zone is potentially becoming

smaller, but it is clear at this point that the recirculation zone is being shifted. This will be addressed more formally in section 6.3.

Moving further downstream from *x/c*=1, the effects of the wall jet on the evolution of the wake are largely as anticipated. Figures 6.8 & 6.9 show the downstream velocity profiles for cases B0.5-B2 and A1, B1, & C1, respectively.

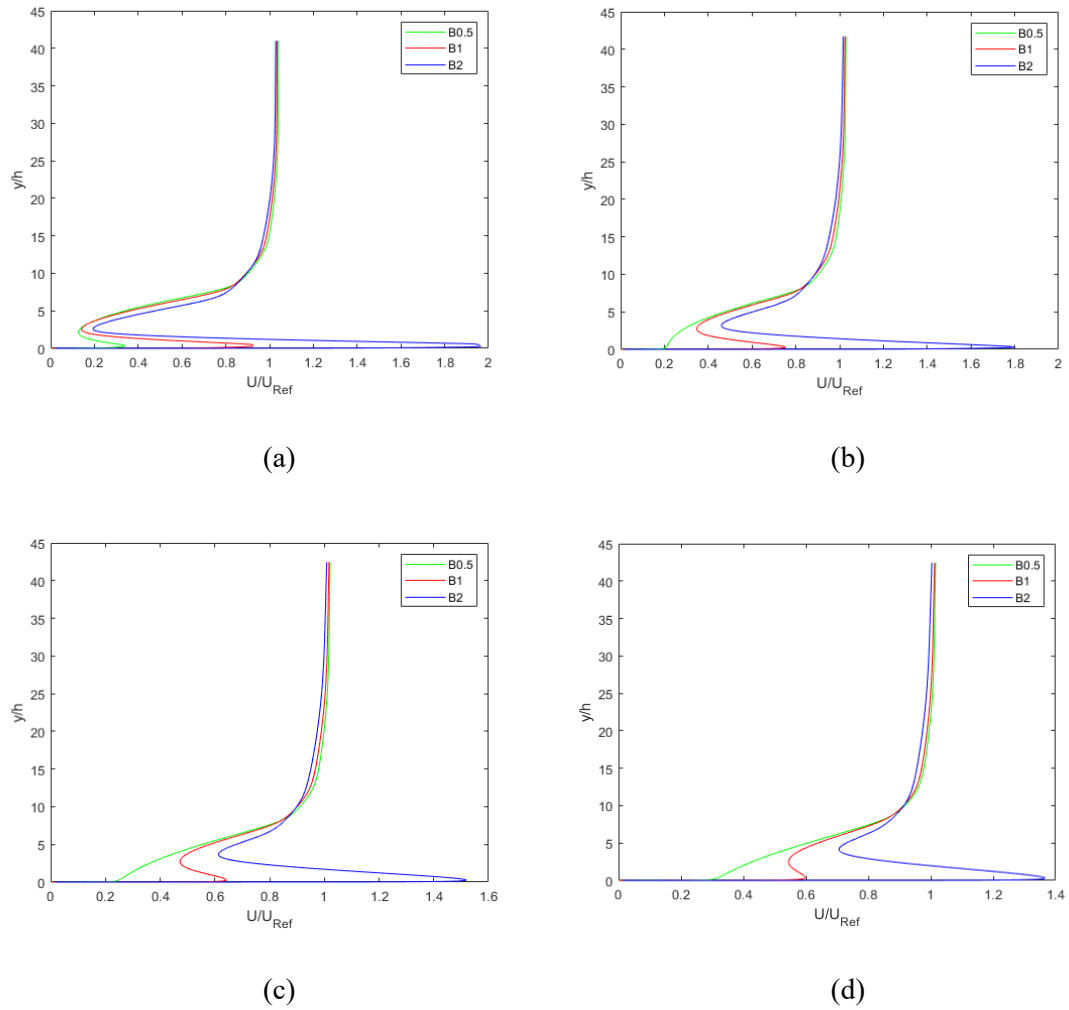

Figure 6.8: Wall-Jet Hump-Wake Downstream Velocity Profiles Grouped by *h* for Cases B0.5-B2; (a) *x/c*=1.1, (b) *x/c*=1.2, (c) *x/c*=1.3, (d) *x/c*=1.4, (e) *x/c*=1.5, (f) *x/c*=2.0, (g) *x/c*=2.5, (h) *x/c*=3.0

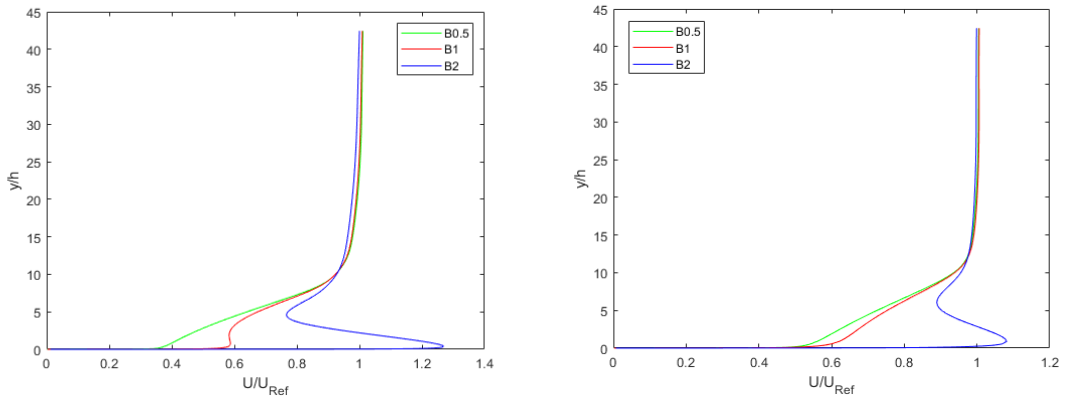

(e) (f)

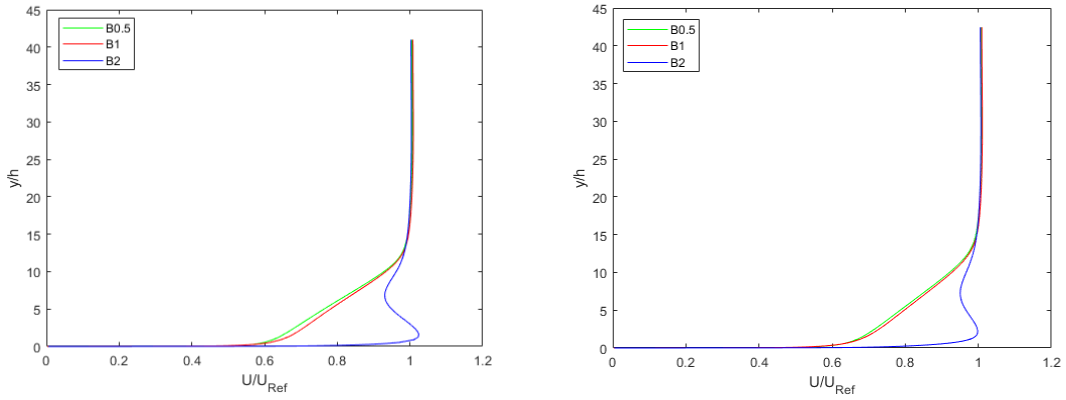

(g) (h)

Figure 6.8 (Continued): Wall-Jet Hump-Wake Downstream Velocity Profiles Grouped by *h* for Cases B0.5-B2; (a) *x/c*=1.1, (b) *x/c*=1.2, (c) *x/c*=1.3, (d) *x/c*=1.4, (e) *x/c*=1.5, (f) *x/c*=2.0, (g) *x/c*=2.5, (h) *x/c*=3.0

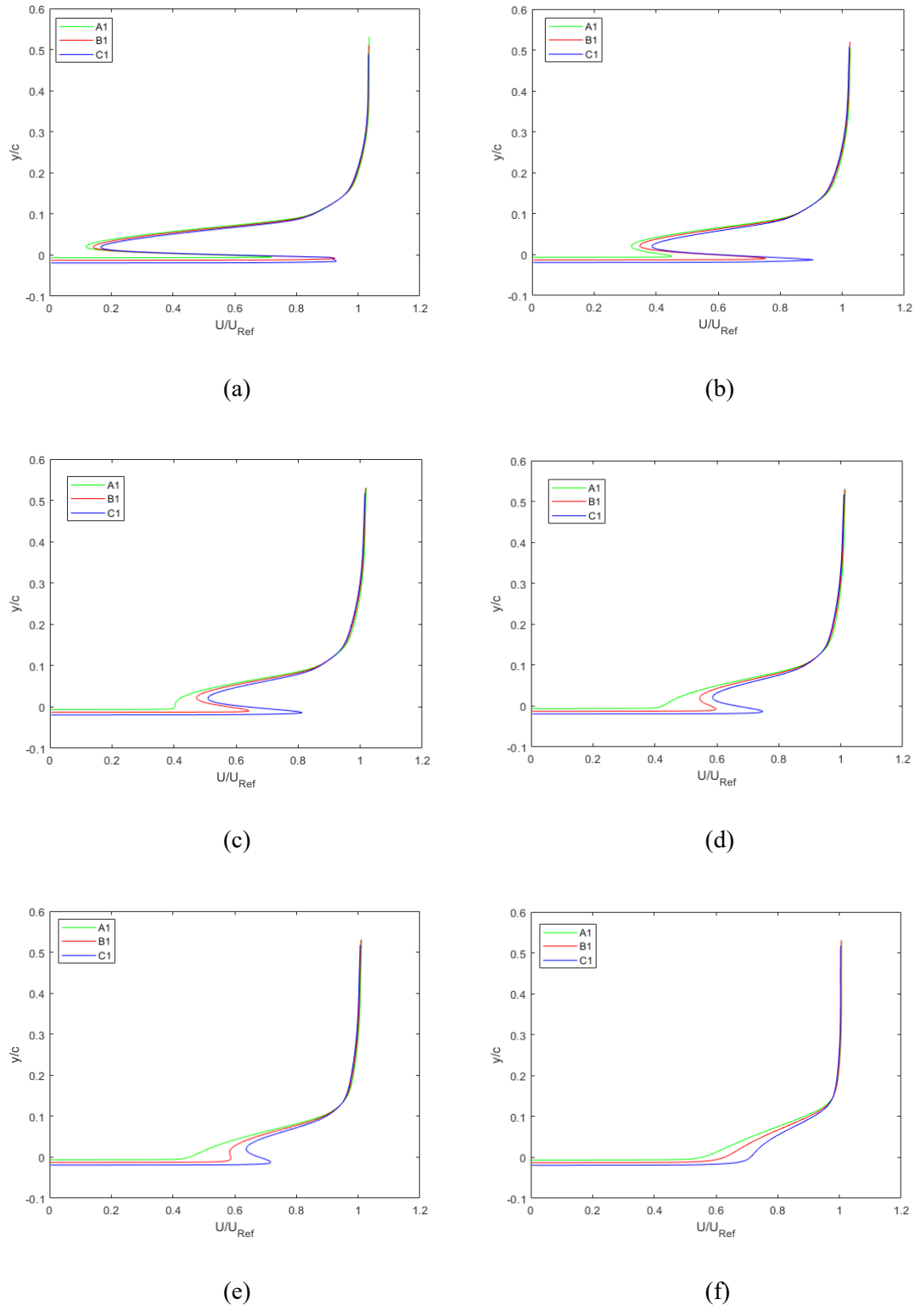

Figure 6.9: Wall-Jet Hump-Wake Downstream Velocity Profiles Grouped by U_J/U_S for Cases A1, B1, & C1; (a) x/c=1.1, (b) x/c=1.2, (c) x/c=1.3, (d) x/c=1.4, (e) x/c=1.5, (f) x/c=2.0, (g) x/c=2.5, (h) x/c=3.0

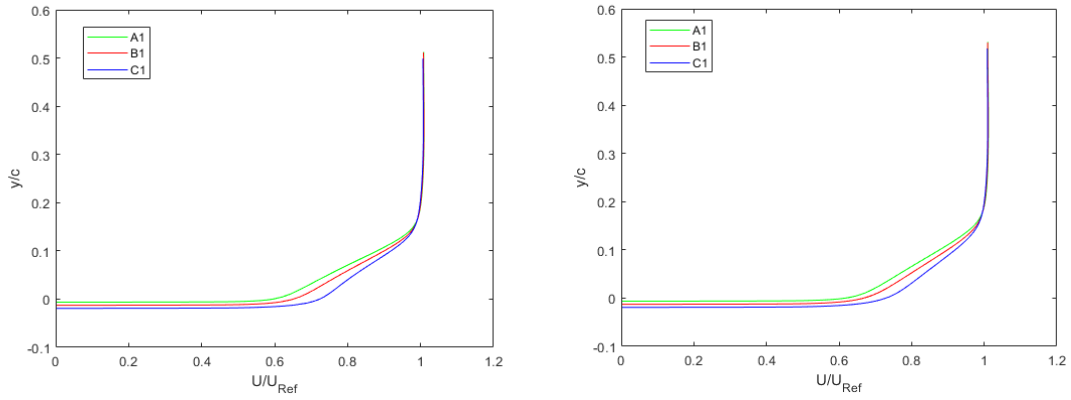

(g) (h)

Figure 6.9 (Continued): Wall-Jet Hump-Wake Downstream Velocity Profiles Grouped by U_J/U_S for Cases A1, B1, & C1; (a) x/c=1.1, (b) x/c=1.2, (c) x/c=1.3, (d) x/c=1.4, (e) x/c=1.5, (f) x/c=2.0, (g) x/c=2.5, (h) x/c=3.0

From a general perspective, raising the wall jet velocity increases the wake recovery rate, which is expected. Increasing wall jet slot height is also shown to increase the wake recovery rate, although the effects are not as drastic. An interesting note, seen most effectively in Figures 6.8a & 6.9a, is that with both wall jet velocity and slot height variations, the wall jet velocity is significantly decreased between x/c=1 and x/c=1.1 for the smallest slot height and lowest velocity cases. This is an early insight on the effectiveness of the momentum carried by the wall jet, where the higher velocities and slot heights carry more momentum and are much less affected by the wake.

6.3: Analysis of the Recirculation Zone

The general shape of the recirculation zone was looked at to visualize the overall effects of the wall jet in terms of reversed flow velocity reduction. The following plots (Figures 6.10 & 6.11) are derived from isosurfaces where the streamwise velocity is equal to zero, effectively outlining the perimeter of the negative streamwise velocities in the recirculation zone.

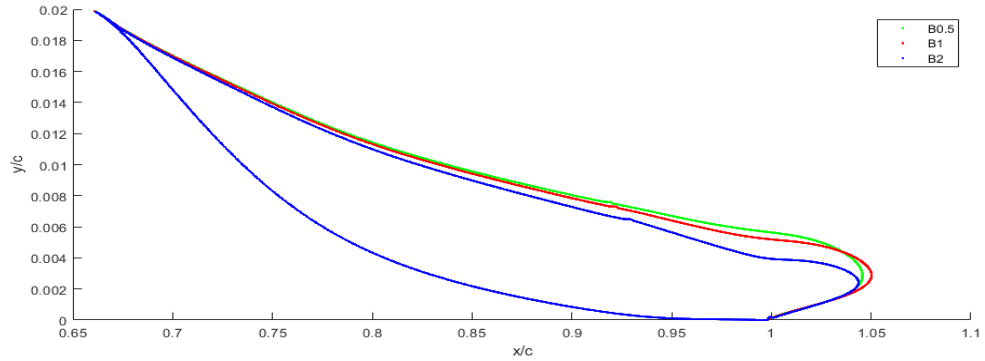

Figure 6.10: Wall-Jet Hump-Wake Recirculation Perimeter for Cases B0.5-B2

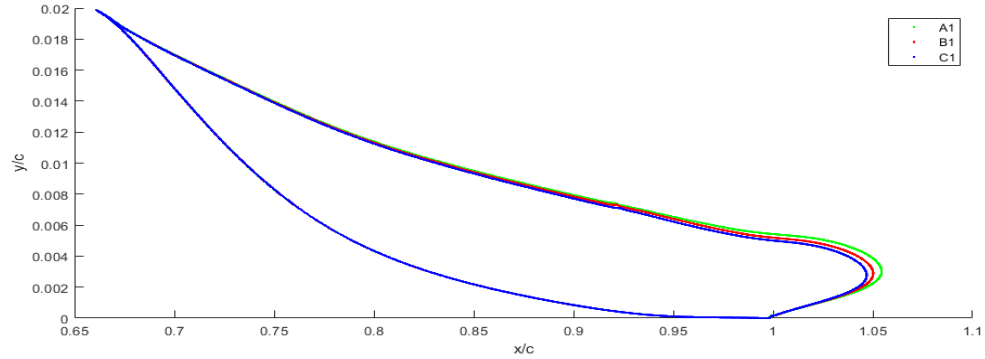

Figure 6.11: Wall-Jet Hump-Wake Recirculation Perimeter for Cases A1, B1, & C1

While the separation point is not clear from these figures, effects on the flow reversal line as well as the downstream “overhang” of the reversed flow region past the trailing edge are clear. It can be seen that the flow reversal line moves closer to the hump with both increasing wall jet slot height and velocity. It is also seen that this effect intensifies with downstream distance. However, an interesting note from Figure 6.10 is that there isn’t a uniform trend in the streamwise location of the end of the recirculation zone. While an increase in slot height gradually reduces this position, it appears that increasing the wall jet velocity toward that of the freestream, the recirculation zone is stretched out. Increasing the wall jet velocity past the freestream velocity

reduces the location of the maximum negative value. This phenomena will be investigated further later on.

Table 6.1: Recirculation Zone Streamwise Dimensions

Case	Separation Point (*x/c*)	Reattachment Point (*x/c*)	Streamwise Length of Reversed Flow at the Wall (*x/c*)
A0.5	0.6608	0.9974	0.3366
A1	0.6611	0.9980	0.3369
A2	0.6616	0.9980	0.3364
B0.5	0.6607	0.9980	0.3373
B1	0.6611	0.9982	0.3372
B2	0.6616	0.9982	0.3367
C0.5	0.6611	0.9979	0.3369
C1	0.6613	0.9979	0.3366
C2	0.6619	0.9982	0.3364

Table 6.1 shows the streamwise dimensions of the recirculation zone. Here, separation and reattachment points were determined by the inflection of the wall shear stress over the τ_w=0 axis. From here, it is clear that an increase in wall jet velocity moves the separation point of the bubble further downstream. Additionally, with the exception of case A1, the separation bubble streamwise span decreases with an increase in both slot height and wall jet velocity. Overall, an increase in either parameter is shown to slightly decrease the size of the recirculation zone.

6.4: Wall-Jet Hump-Wake Reynolds Stress Profiles

In an effort to explain the shifting of the recirculation zone, momentum transfer from the wall jet to the wake is investigated. Reynolds stresses can be a measure of turbulence momentum transfer, as they describe momentum flux [40]. Figure 6.12 below shows the Reynolds stress profiles for cases B0.5-B2.

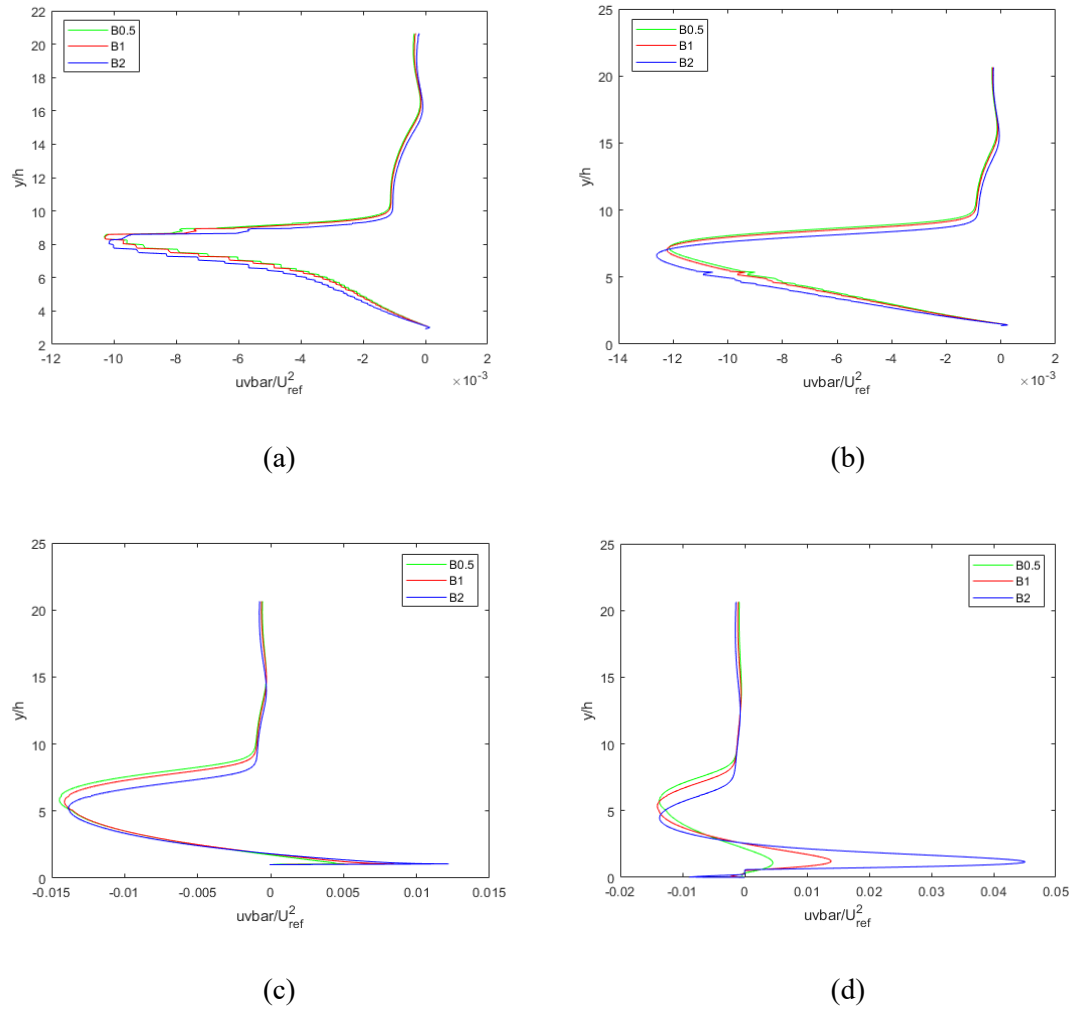

Figure 6.12: Wall-Jet Hump-Wake Reynolds Stress Profiles Grouped by *h* for Cases B0.5, B1, & B2; (a) *x/c*=0.8, (b) *x/c*=0.9, (c) *x/c*=1.0, (d) *x/c*=1.1, (e) *x/c*=1.2, (f) *x/c*=1.3, (g) *x/c*=1.4, (h) *x/c*=1.5

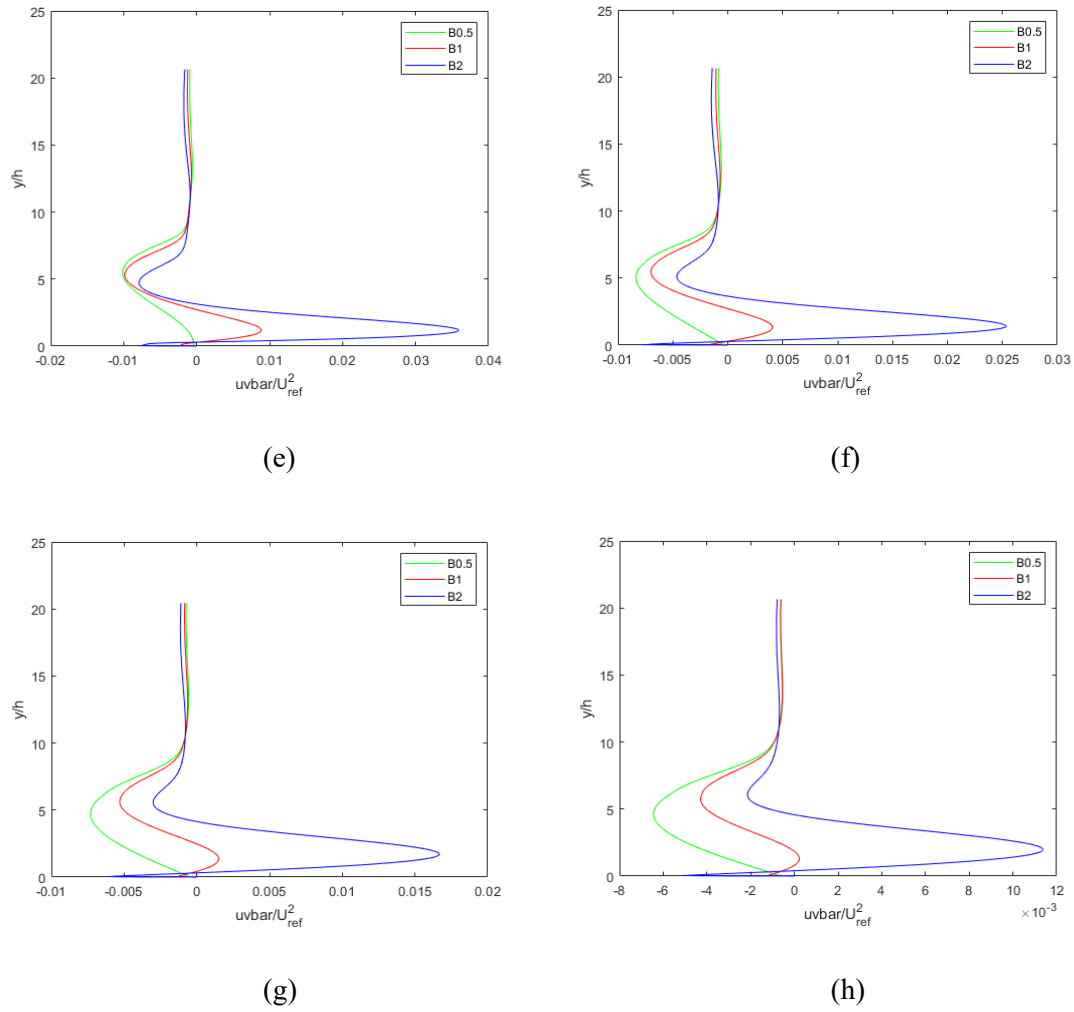

Figure 6.12 (Continued): Wall-Jet Hump-Wake Reynolds Stress Profiles Grouped by *h* for Cases B0.5, B1, & B2; (a) *x/c*=0.8, (b) *x/c*=0.9, (c) *x/c*=1.0, (d) *x/c*=1.1, (e) *x/c*=1.2, (f) *x/c*=1.3, (g) *x/c*=1.4, (h) *x/c*=1.5

The Reynolds stress profiles at *x/c*=0.8, 0.9, and 1.0 provide useful information on the changes in intensity of the recirculation zone with increasing velocity. At *x/c*=0.8 & 0.9, the minimum Reynolds stress (maximum deficit) becomes slightly more negative for increasing jet velocity. This indicates a more turbulent recirculation zone with increase in wall jet velocity. Additionally, the Reynolds stress profiles at these two positions move closer to the wall with increasing velocity, leading to the conclusion that the turbulence intensity of the recirculation is becoming

more concentrated toward the wall and reducing in effect near the outer wake layer with higher wall jet velocity. At x/c=1.0, the effects of the jet momentum at the trailing edge are seen very clearly. It is seen here that at the surface, the increase in wall jet velocity leads to a significantly higher Reynolds stress prediction. In fact, the magnitude of the Reynolds stress for the highest wall jet magnitude is almost of the same order of the lowest Reynolds stress in the wake region. It is evident here that the wall jet is shifting the bubble due to momentum transfer along the aft surface of the hump. Additionally, it is seen that the profiles are shifted in the streamwise direction, indicating that the momentum transfer is beginning to drive the flow in the streamwise direction.

Downstream of the trailing edge, the momentum transfer from the wall jet to the wake region is much more evident. At x/c=1.1, Reynolds stresses are the highest at the peak velocity of the wall jet, and increasing velocity is seen to significantly increase the Reynolds stress profile across the entire wall jet. From x/c=1.2 downstream, it is clear that the momentum transfer of the wall jet is driving the flow and increasing the wake recovery rate as more momentum is transferred in the wall-normal direction. For an increase in velocity, the Reynolds stresses are more positive at any point in the bulk flow of the wall jet and the wake region all the way up to approximately y/h=10, where the data collapses, indicating more positive momentum transfer across the profiles for increased wall jet velocity. The negative peak in Reynolds stresses near the wall is much more negative for a higher velocity, which is sensible considering the wall is not moving.

Overall, the general trends for turbulent momentum transfer with increasing wall jet velocity are present with increase in slot height, although some differences are present (see Figure 6.13).

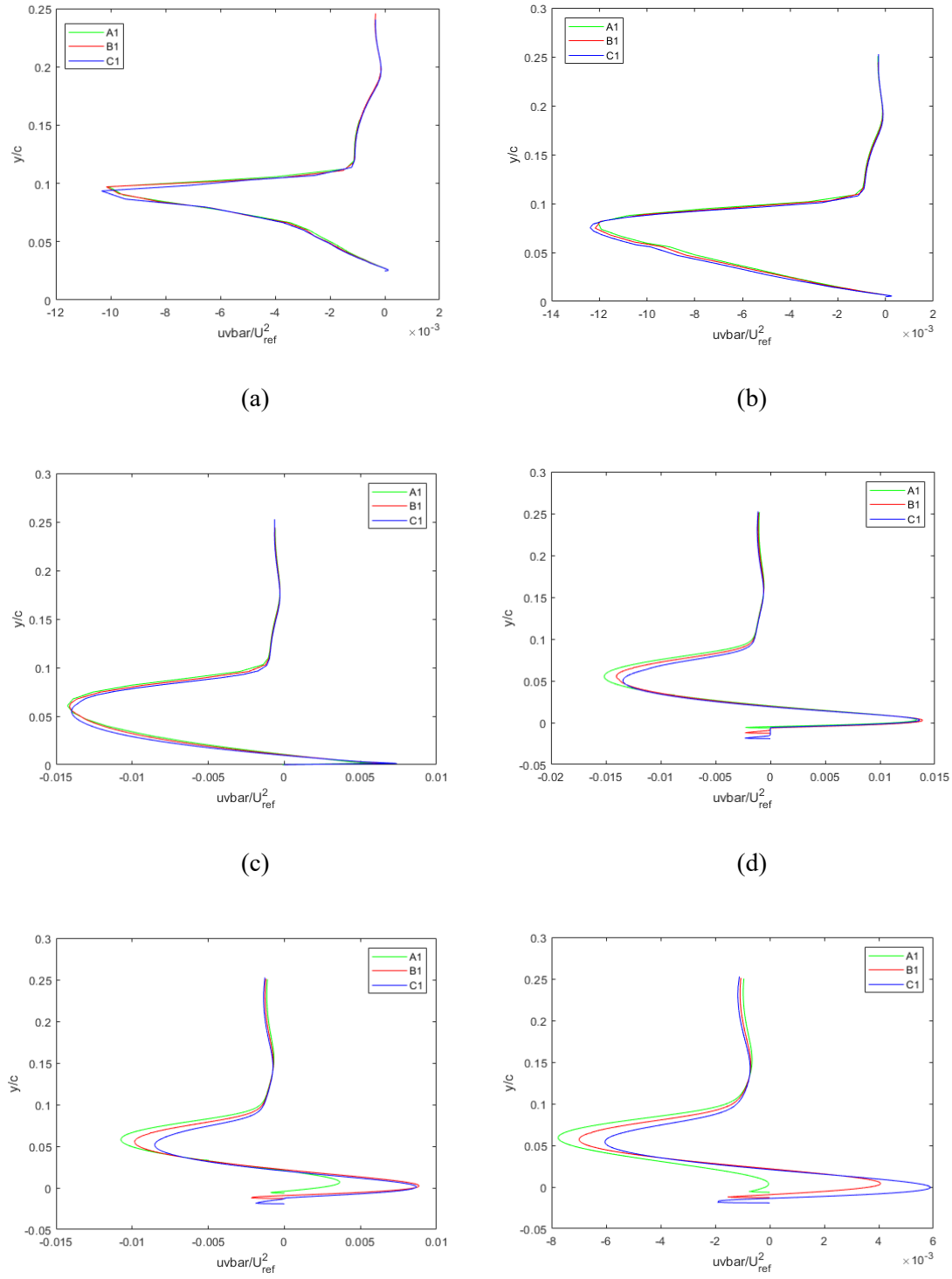

Figure 6.13: Wall-Jet Hump-Wake Reynolds Stress Profiles Grouped by U_J/U_S for Cases A1, B1, & C1; (a) x/c=0.8, (b) x/c=0.9, (c) x/c=1.0, (d) x/c=1.1, (e) x/c=1.2, (f) x/c=1.3, (g) x/c=1.4, (h) x/c=1.5

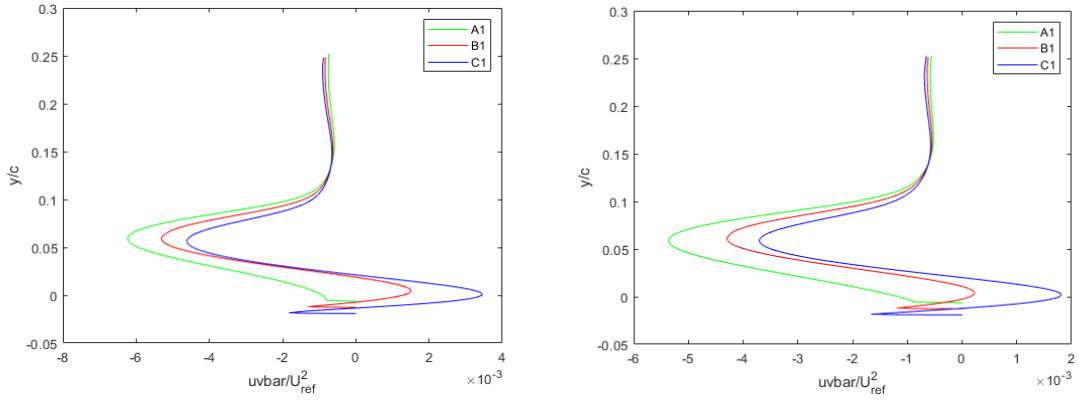

(g) (h)

Figure 6.13 (Continued): Wall-Jet Hump-Wake Reynolds Stress Profiles Grouped by U_J/U_S for Cases A1, B1, & C1; (a) x/c=0.8, (b) x/c=0.9, (c) x/c=1.0, (d) x/c=1.1, (e) x/c=1.2, (f) x/c=1.3, (g) x/c=1.4, (h) x/c=1.5

It is first noted that the profiles along the hump surface and downstream differ much less with respect to slot height than with respect to velocity, indicating that the increase in slot height has less of an effect on momentum transfer upstream. More importantly, at x/c=1.1, it is seen that with increase in slot height, the minimum Reynolds stress in the recirculation zone increases positively with increased slot height, whereas with increasing velocity the minimum is hardly changed. This indicates that increasing slot height more uniformly transfers momentum in the wall normal direction immediately after the slot,whereas much of the momentum transfer differences with increasing wall jet velocity are seen within the wall jet and the mixing layer between it and the wake. This is most likely due to a sharper velocity gradient in this mixing layer with increasing wall jet velocity, resulting in much of the momentum consumption to be in the streamwise direction.

6.5: Recirculation Zone Flow Visualization

Now that it has been shown that the recirculation zone is being repositioned and changed in size due to changes in the wall jet's slot height and velocity, it is appropriate to provide a

broader view of the recirculation zone to view the overall effects of the wall jet on the entire zone. Figure 6.14 shows the convoluted streamlines in the vicinity of the recirculation zone.

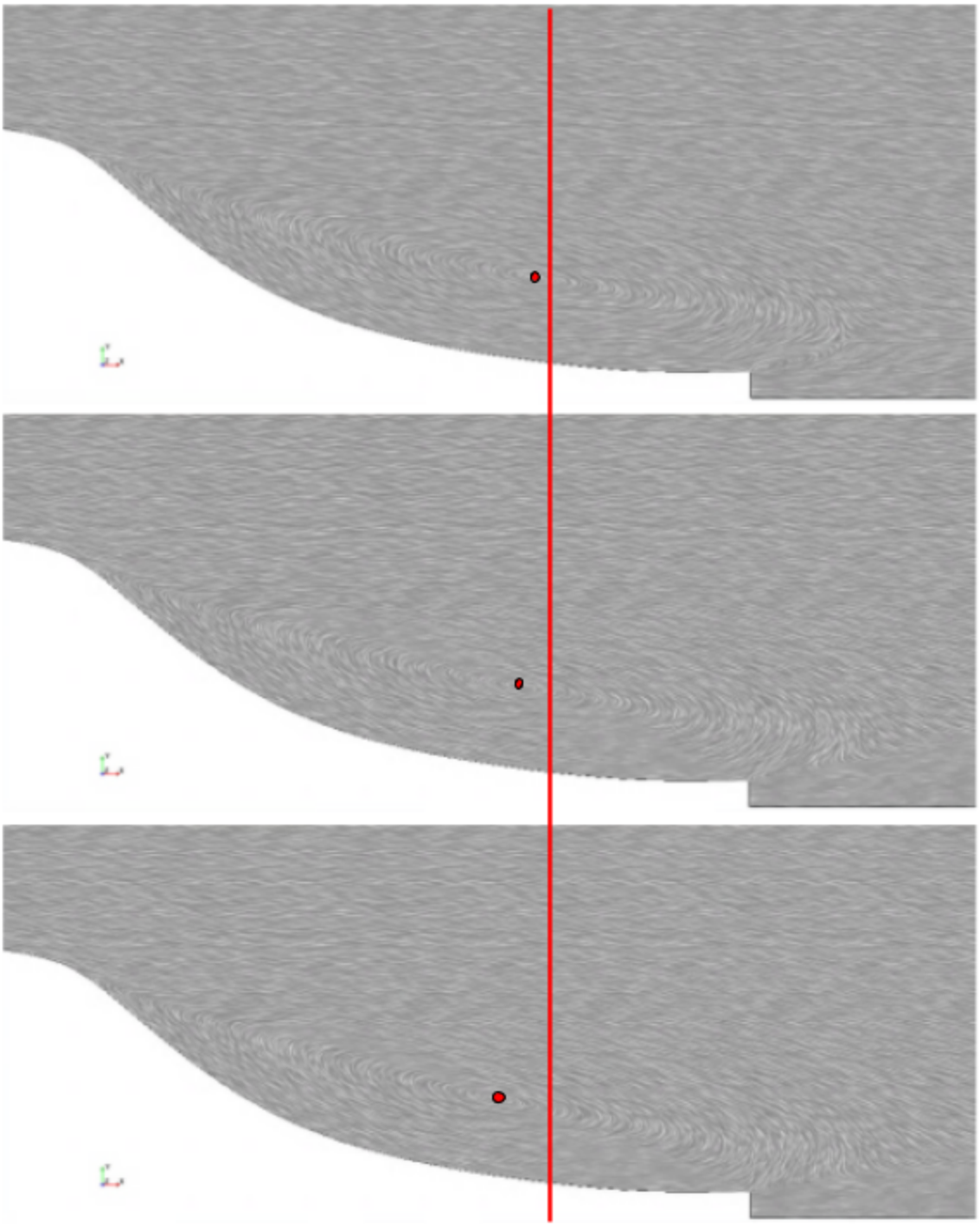

Figure 6.14: Convoluted Streamlines for Cases B0.5-B2; Top B0.5, Middle B1, Bottom B2

It is clear that the “eye” of the recirculation zone is being moved forward (toward the leading edge) with increasing jet velocity. While this trend is also followed for increase in wall jet slot height, the shift is much smaller (Figure 6.15).

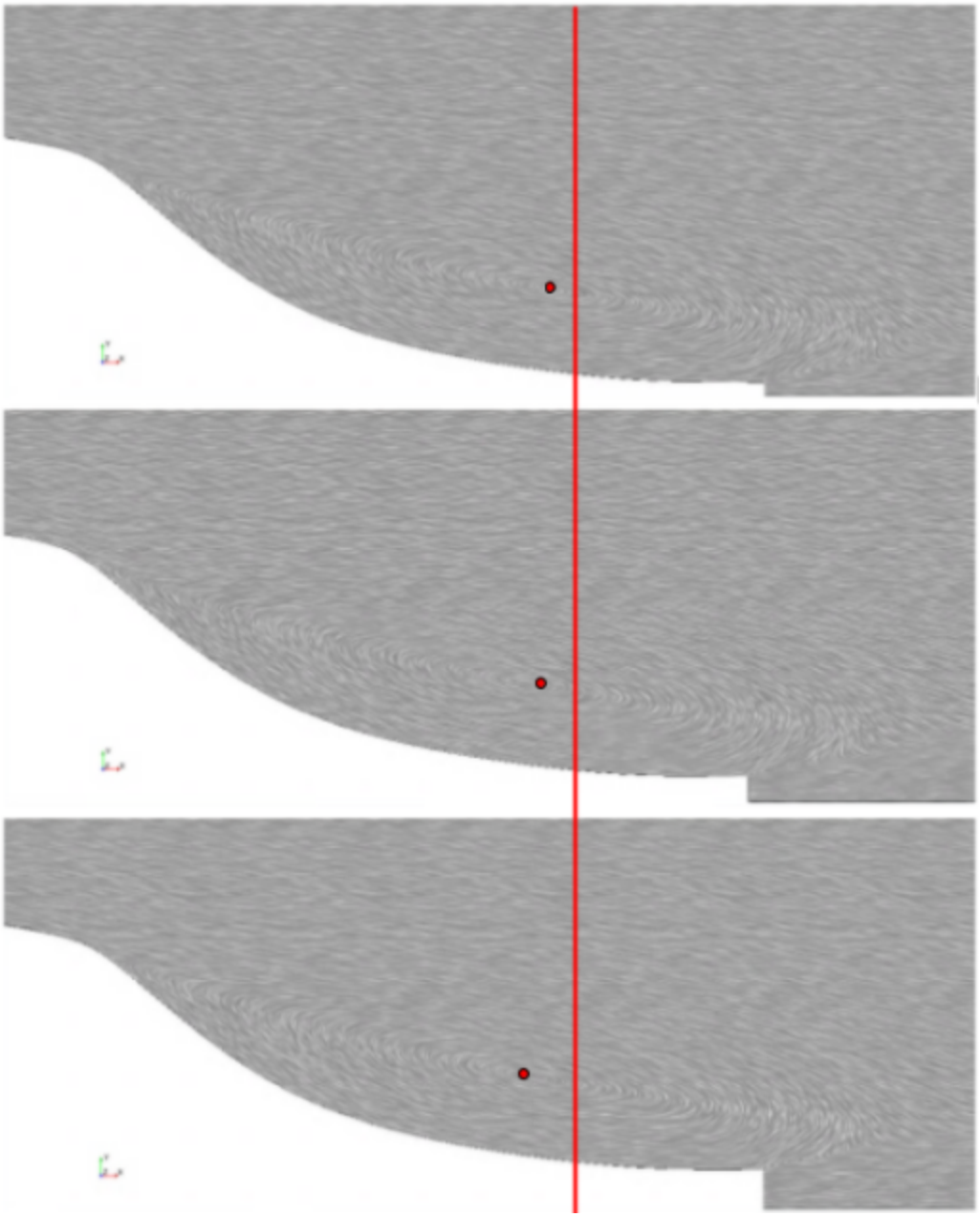

Figure 6.15: Convoluted Streamlines for Cases A1, B1, & C1; Top A1, Middle B1, Bottom C1

To show the changes in the velocity field due to the changes in wall jet flow, delta *U* scenes between cases B0.5 and B2 were created, seen below in Figure 6.16. Here, it must be noted that due to differing grids and differing domain sizes between cases where the wall jet slot height was varied, delta scenes could not be created because the *y* coordinates for each grid differed. However, since all outlined trends seen for increase in wall jet velocity are also followed for changes in wall jet slot height, it is assumed that the same trends noted in the delta scenes for changing wall jet velocity are similar to those for changing wall jet slot height.

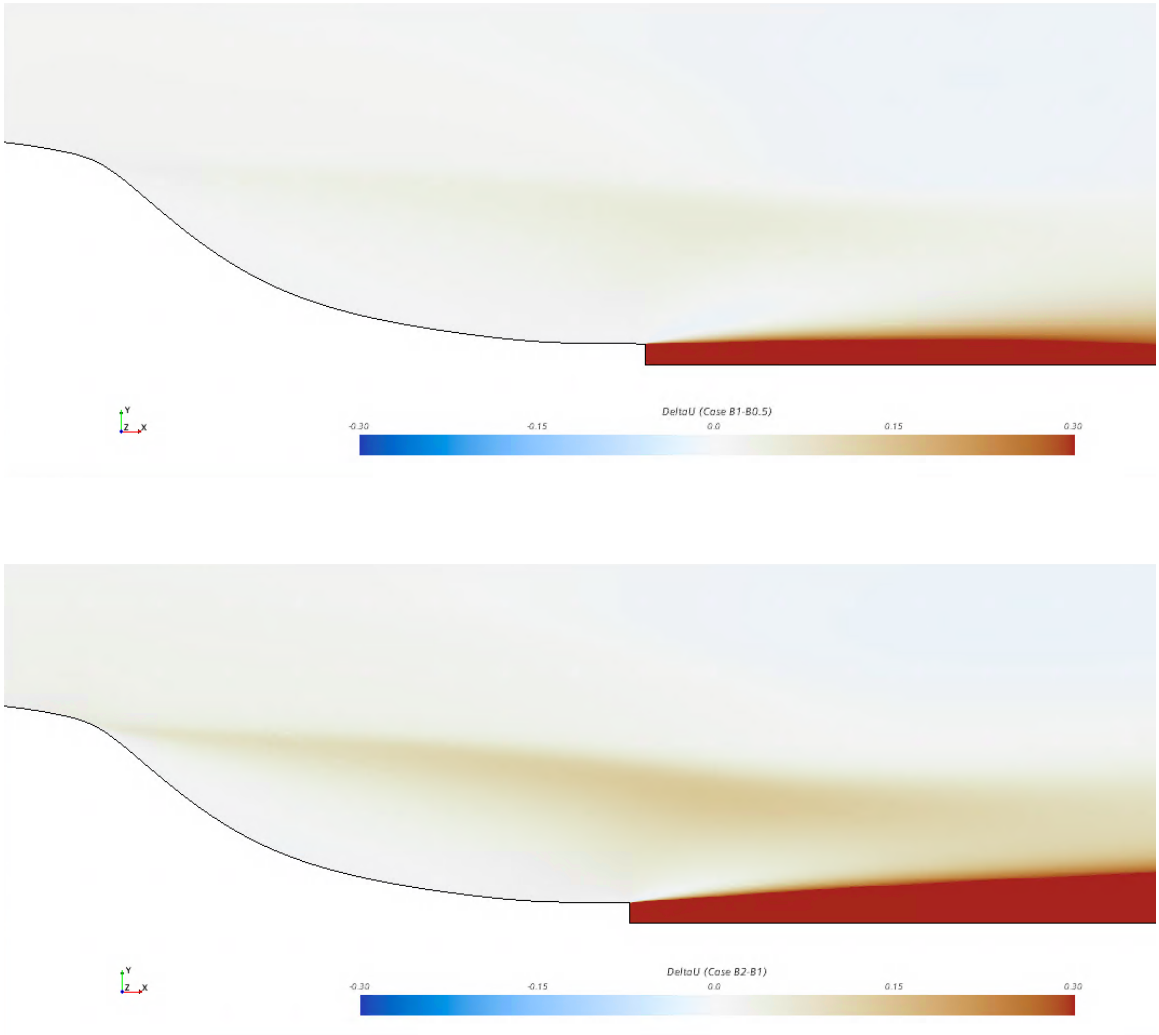

Figure 6.16: Delta *U* Scenes for Cases B0.5-B2; Top B0.5, Middle B1, Bottom B2

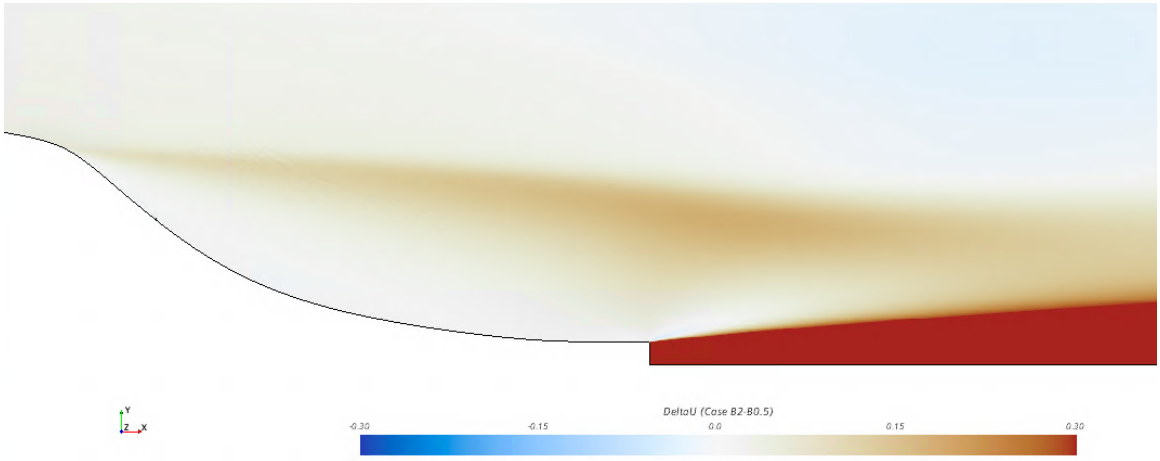

Figure 6.16 (Continued): Delta *U* Scenes for Cases B0.5-B2; Top B0.5, Middle B1, Bottom B2

It is noted that the recirculation zone near the hump surface is largely unchanged. In respect to increasing wall jet velocity ,it is also seen that with increasing downstream distance from the wall jet, the increased wall jet's velocity becomes more influential on the wake flow above. The resultant increased velocity in the above wake region at these downstream locations is seen to positively influence the velocity in the upstream direction along the outer layer of the wake via momentum transfer, all the way to the top of the hump and beyond. However, it is clear that there is a barrier between the wall jet and the wake flow in the vicinity of the wall jet slot. It is plausible to conclude that the velocity streamlines are converging downstream of this barrier, causing the outer wake to accelerate.

Before investigating the present barrier, it is also important to consider energy losses, as it is seen that the velocity in the recirculation zone is mostly unaffected by increase in either wall jet slot height or wall jet velocity, leading to speculation that this barrier may also affect the pressure in the recirculation zone. Figure 6.17 shows the delta C_P scenes for the recirculation zone.

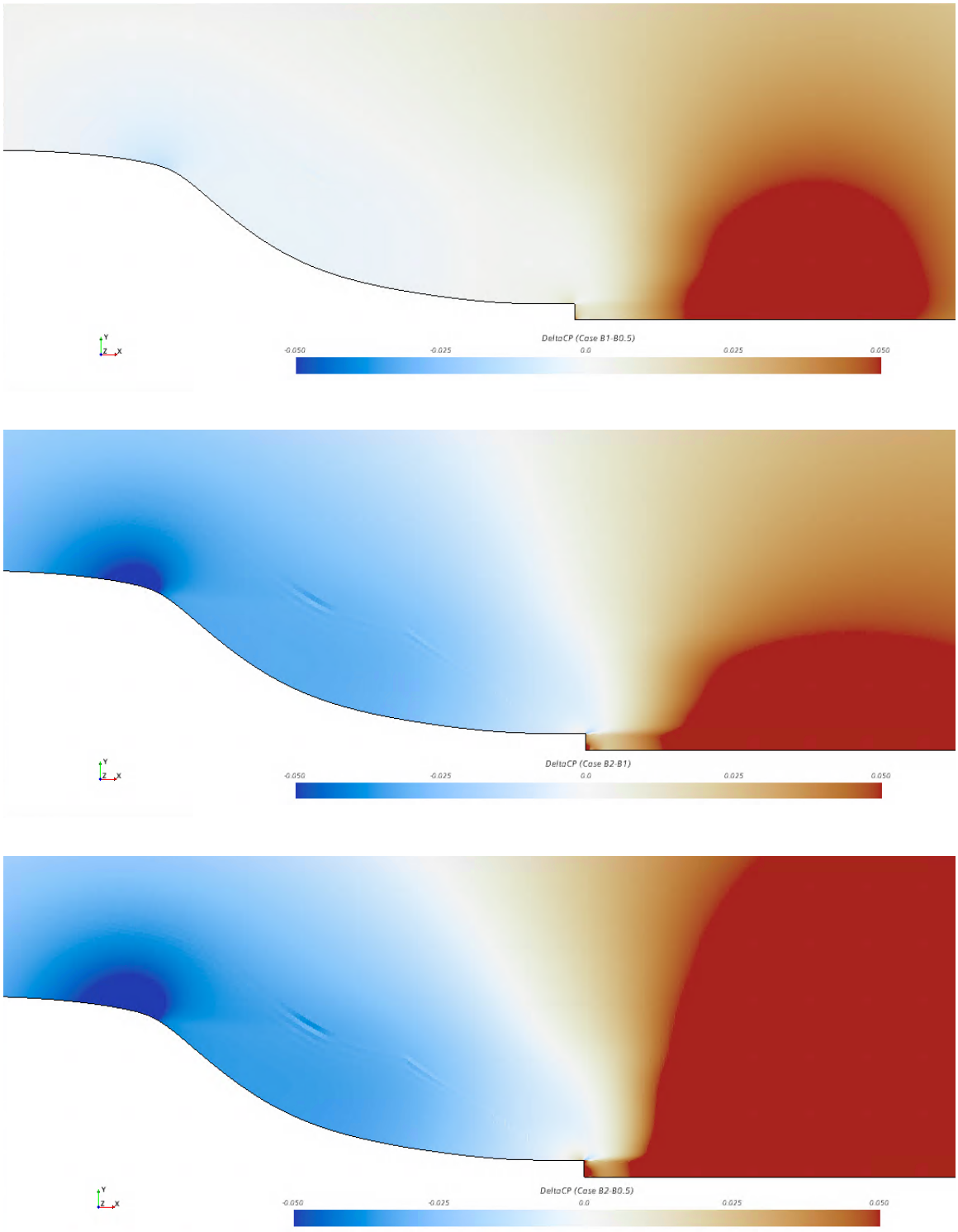

Figure 6.17: Delta C_p Scenes for Cases B0.5-B2; Top B0.5, Middle B1, Bottom B2

As expected, the low pressure region in the vicinity of the separation point grows with increasing wall jet velocity. It was already shown that pre-separation velocity near the hump surface increases with increasing wall jet velocity, resulting in a delayed separation point and lower pressure. However, it is seen that in the recirculation zone, the pressure decreases with an increase in wall jet velocity, which directly indicates an energy loss here. It is also noted that an increase in wall jet velocity increases the adverse pressure gradient, most prominent in the region slightly downstream of the wall jet slot. Due to the sharp increase in pressure with increased wall jet velocity downstream of the slot, it is evident that there is another mechanism acting in the vicinity of the jet slot. Figures 6.18 & 6.19 show the vorticity magnitude for the cases of focus in this chapter, revealing the barrier in the near-wall jet region.

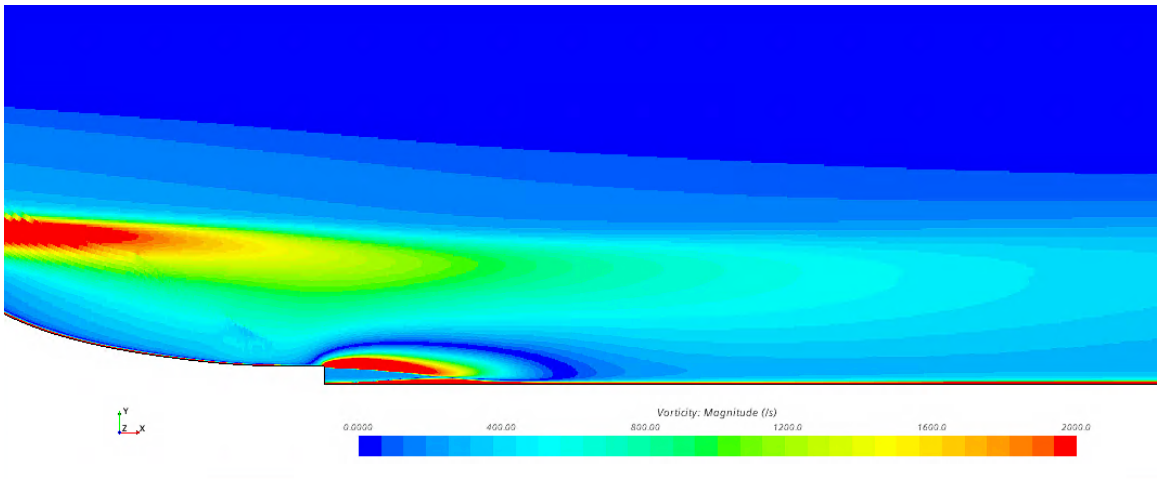

Figure 6.18: Vorticity Magnitude Scenes for Cases B0.5-B2; Top B0.5, Middle B1, Bottom B2

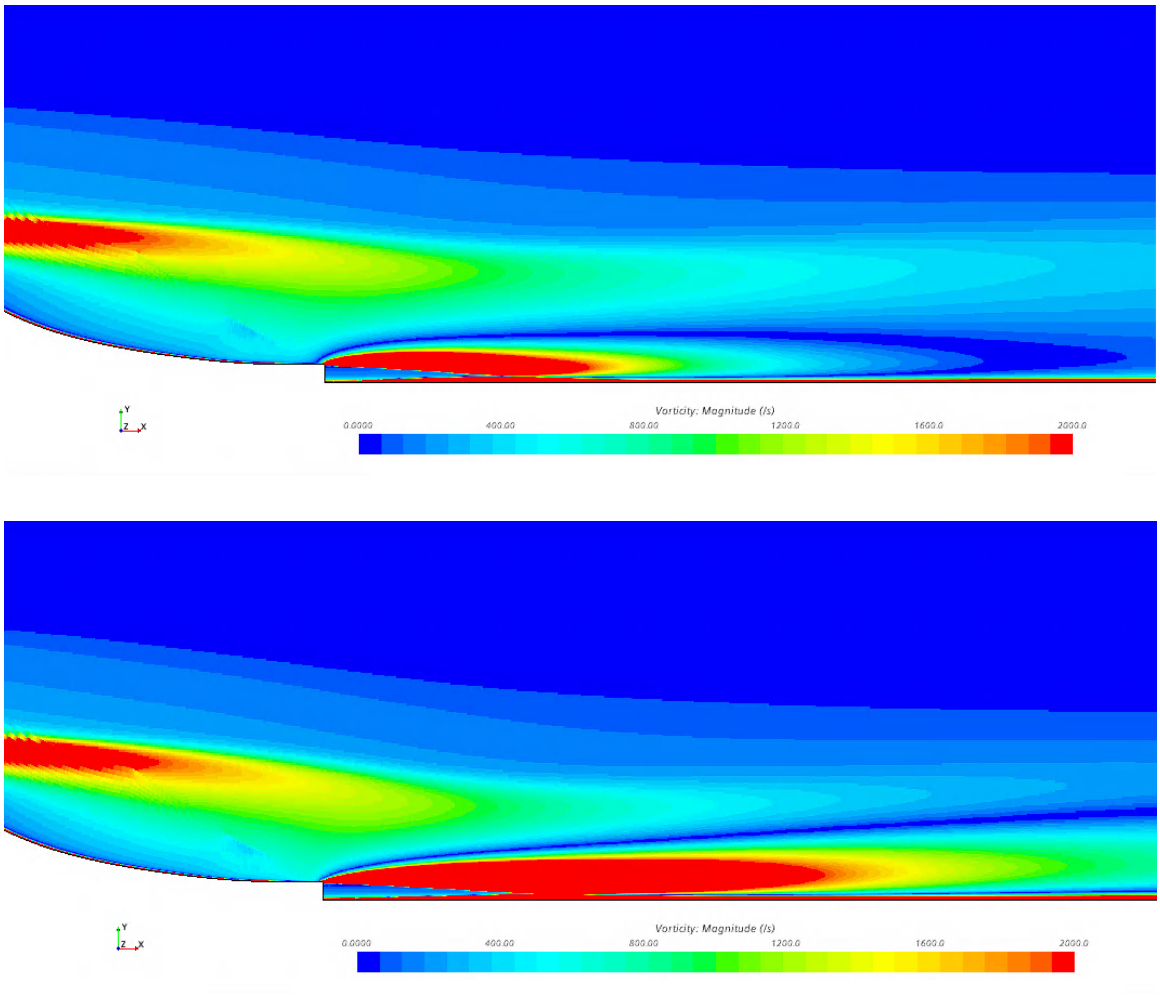

Figure 6.18 (Continued): Vorticity Magnitude Scenes for Cases B0.5-B2; Top B0.5, Middle B1, Bottom B2

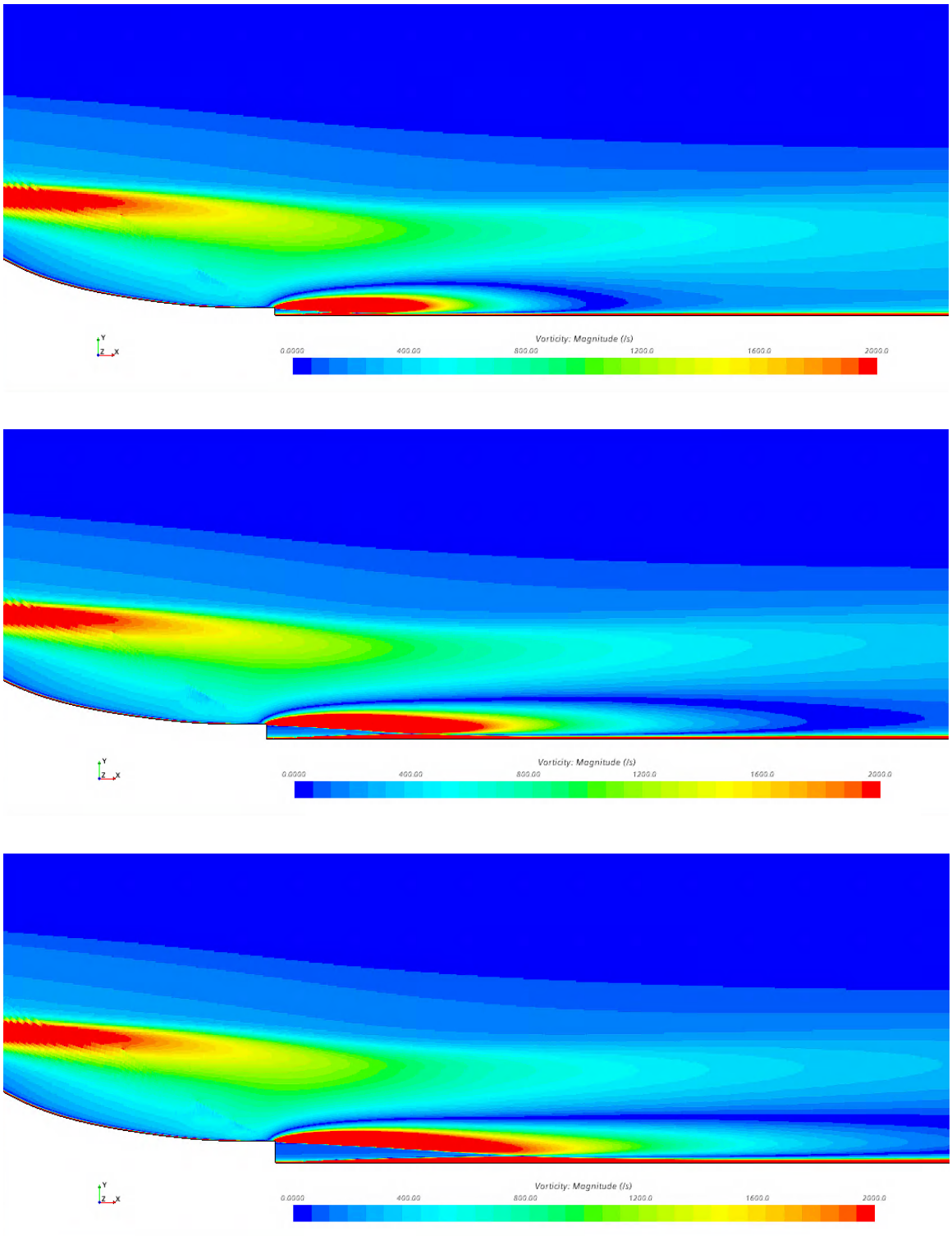

Figure 6.19: Vorticity Magnitude Scenes for Cases A1, B1, & C1; Top A1, Middle B1, Bottom C1

The first noticeable flow feature from the vorticity scenes is the sharp and prominent zero-vorticity barrier around the wall jet. The presence of this alone shows evidence of vortex induced drag from the induced wall jet flow. Additionally, it is noted that this barrier clearly increases in size with an increase in wall jet velocity or slot height, thus presumably increasing vortex induced drag (this will be covered in the proceeding section). However, before proceeding, it is important to recall the increase in downstream reattachment of the recirculation zone with an increase in wall jet slot height and wall jet velocity. It is seen from figures 6.18 and 6.19 that for an increase in either parameter, the vortex barrier is shifting further downstream, indicating that the recirculation zone expands more in the streamwise direction before interacting with the wall jet velocity flow field for an increase in either parameter.

6.6: Analysis of Drag Coefficient

Now that the effects of the wall jet on the turbulence and mean flow characteristics of the hump induced wake have been investigated and explained, the effects of the wall jet on overall aerodynamic performance can be evaluated. Below, in Table 6.2, the total drag coefficient as well as the form and skin friction components is presented.

Table 6.2: Drag Coefficients for Each Case

Case	Total Drag Coefficient	Pressure Component	Shear Component
A0.5	0.1694	0.1448	0.02466
A1	0.1770	0.1523	0.02471
A2	0.2026	0.1775	0.02508
B0.5	0.1736	0.1488	0.02472
B1	0.1815	0.1567	0.02476
B2	0.2095	0.1843	0.02521
C0.5	0.1815	0.1567	0.02480
C1	0.1868	0.1619	0.02482
C2	0.2131	0.1878	0.02526

It can be seen from Table 6.2 that the drag coefficient for the hump is largely dominated by form drag, which is typical of bluff bodies, considering the pressure drag component is a magnitude larger than the shear component. The major trend seen in the table is that for both increasing slot height and increasing jet velocity, the total drag as well as both components increases. While this is expected from the above findings, a detailed look at both components is required for further discussion.

6.6.1: Skin Friction Contribution to Total Drag

The normalized skin friction coefficient can be used to visualize the mechanism governing the total skin friction drag in Table 6.2.

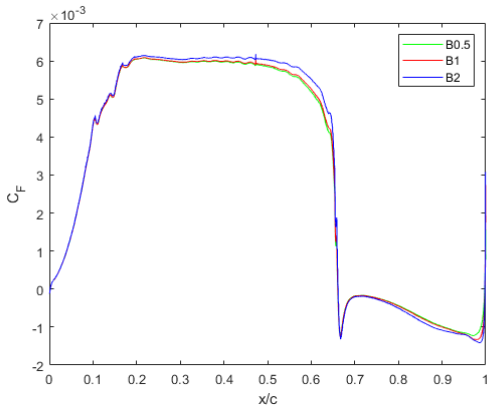

Figure 6.20: Wall-Jet Hump-Wake Skin Friction Coefficient Across the Hump for Cases B0.5-B2

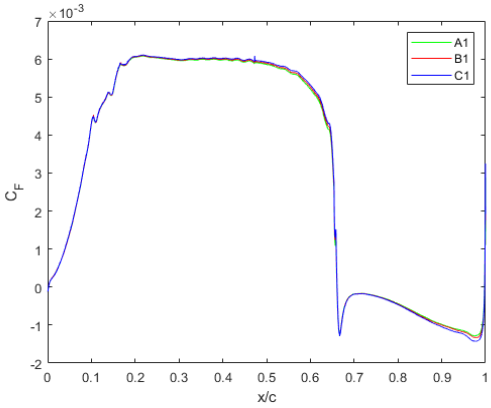

Figure 6.21: Wall-Jet Hump-Wake Skin Friction Coefficient Across the Hump for Cases A1, B1, & C1

Figures 6.20 & 6.21 show the skin friction coefficients for cases B0.5-B2 as well as cases A1, B1, & C1.. Starting at *x/c*=0 and moving downstream, all cases show a positive and increasing C_F as the flow climbs over the forebody of the hump and recovers from the high pressure, low velocity point at the leading edge. The flow quickly grows positively (increasing drag) along the fore side of the hump, following the hump's curvature and lessening in the gradient as the hump begins to plateau. This is the result of the velocity deficit caused near the

leading edge recovering until the re-establishing underlying boundary layer flow becomes more prominent. This is better visualized with a streamwise velocity field (Figure 6.22 below).

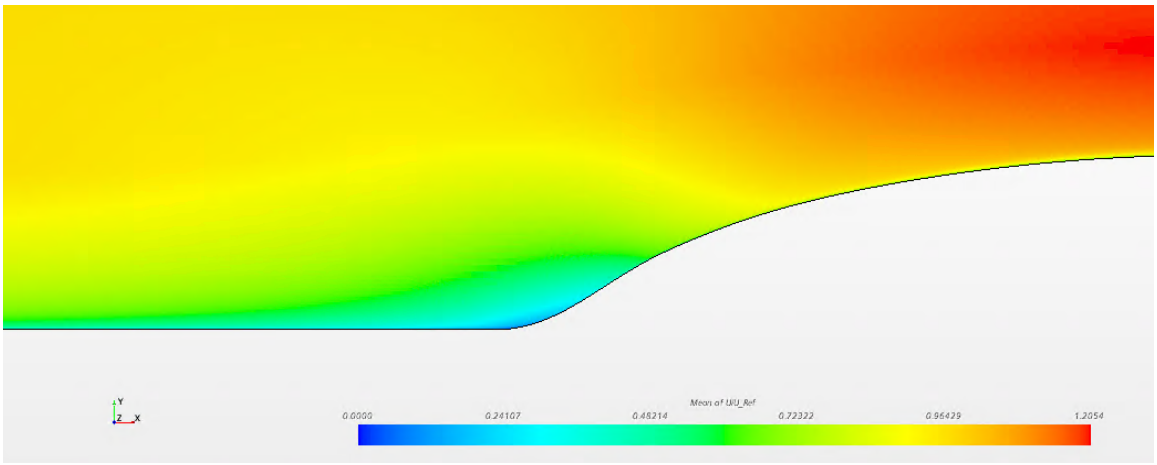

Figure 6.22: Wall-Jet Hump-Wake Leading Edge Velocity Field, Case B1

At about x/c=0.22, the skin friction coefficient plateaus and remains relatively close to constant while slowly decreasing (the pressure is now reducing with increased downstream distance). At about x/c~0.57, the skin friction coefficient sharply plumits, becoming negative at about 0.66, indicating the separation point. This negative coefficient quickly moves toward zero until x/c~0.71, where it slowly begins to regain negativity up to a point very near the trailing edge. This positive gradient of the skin friction coefficient immediately after separation is explained by [33], who show that the streamlines of the reversed flow near the separation point are converging and thus accelerating in the counter-flow direction. Once the flow nears the trailing edge, the skin friction coefficient again becomes positive at the reattachment point and abruptly rises as the flow reattaches and effects of the wall jet's momentum become prominent, resulting in an increase in skin friction drag.

As expected, the variations in C_F are most notable along the top of the hump and near the trailing edge, where the geometry represents more of a flat plate than a bluff body. Along the top, the variation between cases grows with streamwise distance all the way to *x/c*=0.65. In regards to the effects of slot height, it is seen that an increase in this parameter also increases the skin friction at any given point from *x/c*=0.2 to *x/c*=0.65 with respect to the lower slot height. This is the effect of higher velocity along the top of the hump for increase in slot height, previously shown. From this point up to slightly after *x/c*=0.8, the variation in skin friction coefficient between cases is negligible. After *x/c*=0.8, the highest slot height produces the lowest skin friction coefficient, indicative of a more intense recirculation zone, previously covered. The same trends outlined above are seen for increasing velocity, although the effects are more prominent. The overall increase in skin friction drag with increasing velocity can be contributed to the fact that the increase in C_F with an increasing jet velocity along the top of the hump is much larger in magnitude, outweighing the lower coefficient at the trailing edge.

6.6.2: Pressure Contribution to Total Drag

The pressure drag on the hump can be visualized using plotted values of the normalized pressure coefficient along the hump. As opposed to C_F, C_P acts normal to the surface. Therefore, areas where C_P is more influential are also areas where C_F is less influential. The general profile of C_P along the hump is similar for all cases, so as with the skin friction analysis, this analysis will begin with a general end-to-end walkthrough of the structure of the profile, using Figures 6.23 & 6.24 below as reference.

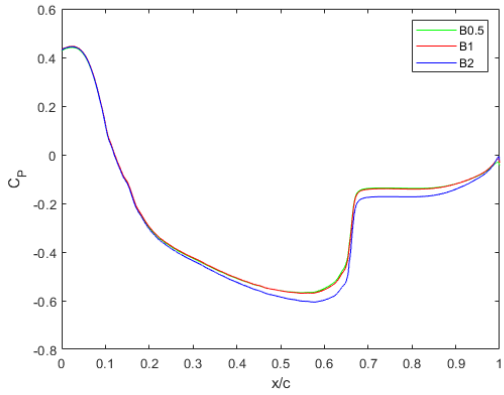

Figure 6.23: Wall-Jet Hump-Wake Pressure Coefficient Across the Hump for Cases B0.5-B2

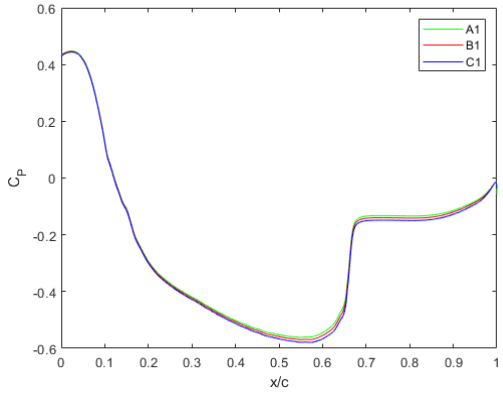

Figure 6.24: Wall-Jet Hump-Wake Pressure Coefficient Across the Hump for Cases A1, B1, & C1

Beginning at x/c=0, the pressure is positive and under an adverse pressure gradient as the effects of the high pressure zone at the leading edge are still recovering. Immediately after the leading edge, the pressure gradient becomes strongly favorable and the pressure coefficient becomes negative at approximately x/c=0.01. The gradient relaxes in coordination with the hump curvature. At x/c=0.6, the gradient becomes adverse and abruptly intensifies at the separation point. From here, the pressure gradient plateaus at roughly x/c=0.68 then slowly begins to accelerate adversely again. This is a result of the sharp downward slope here as discussed in

[GREENBLATT]. There exists a very small region immediately before the trailing edge of the hump (Figure 6.24) where the gradient becomes favorable.

As with the skin friction distribution, pressure coefficient distribution follows the same trends for increase in both jet slot height and jet velocity. Additionally, the variation for velocity increase is much more notable. Along the top of the hump, the pressure coefficient is the lowest for the highest shot height and highest jet velocity, which is expected considering the previously noted delayed separation point for an increase in either parameter. This is also seen after separation along the aft portion of the hump where the flow is reversed. Due to the large energy loss in the recirculation zone with increase in slot height or velocity of the wall jet, the pressure drag is much higher for lower slot height and wall jet velocity.

6.6.3: Accumulated Drag Coefficient

A more general way to determine the location of the drag variations is an accumulated force plot, seen below in Figures 6.25 & 6.26.

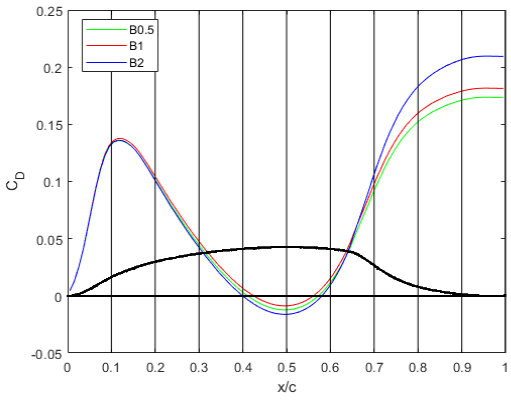

Figure 6.25: Wall-Jet Hump-Wake Accumulated Drag Coefficient Across the Hump for Cases B0.5-B2

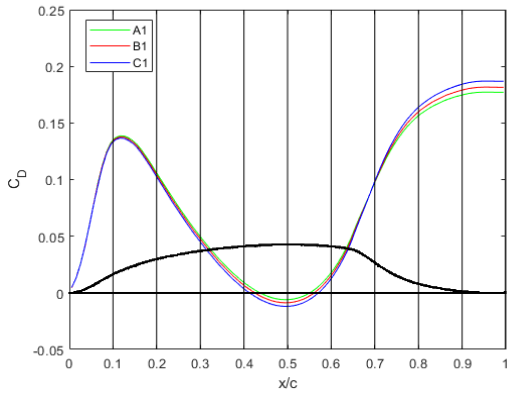

Figure 6.26: Wall-Jet Hump-Wake Accumulated Drag Coefficient Across the Hump for Cases A1, B1, & C1

The first observation made is that effects of the wall jet, while very small, can be seen as far upstream as x/c=0.1. Additionally, between here and roughly x/c=0.5, it is seen that the delay in separation for increasing slot height and jet velocity gradually reduces the accumulated drag force coefficient. After x/c=0.5, the three accumulated C_D curves begin to converge as the separation point is approached, followed by a sharp spike in C_D in the recirculation zone. As explained before, due to higher energy loss with increased wall jet velocity and slot height, the three curves diverge between x/c=0.7 & 0.9, where the higher slot height and higher jet velocity result in a sharper increase in C_D.

At this point, it has been shown that the separation bubble reduction from higher velocity and slot height is clearly counterproductive in the reduction of drag over the hump, as the smaller recirculation zone is much more intense. The major contributor is pressure and the largest deviations in drag coefficient predictions is seen between x/c=0.7 and x/c=0.9. Even so, it is important to note that drag is highly independent on the geometry of the body of interest. Therefore, while the drag characteristics of the hump geometry have been presented in this work,

these findings can not be applied in a canonical sense, hence it is not valid to conclude that a higher wall jet slot or wall jet velocity will always increase the drag on any given body.

6.7: Comparison of Variation in Wall Jet Slot Height Versus Wall Jet Velocity

The dissection and analysis of the effects of the waljet on the hump wake has been explored in detail. It has been shown that both a higher jet slot height and a higher velocity can effectively reduce the size of the recirculation zone and also move the zone further forward in the streamwise direction. The mechanisms driving this phenomena are the increase in momentum of the induced wall jet flow for increase in either h or U_J/U_S affecting the outer layer of the wake, coupled with the growing vortex barrier around the wall jet for increase in either parameter. The shifting of the recirculation zone was shown to have a non-desirable effect on the drag coefficient. However, the question of which parameter, velocity or slot height, has more of an effect on the flow characteristics of the wall-jet hump-wake has not yet been addressed. It is difficult to relate the two because the influential factor of momentum increase at the jet inlet is different for increasing wall jet velocity and increasing slot height. For a higher wall jet velocity, the momentum increase is very well pronounced at the mixing layer between the wake and the wall jet, and the wall normal velocity gradient is much steeper. In the case of increasing slot height, much of the momentum growth is absorbed into the bulk wall jet stream, as the cross sectional area is much higher. Essentially, for two given inlet slots, if the height of one slot is decreased and the velocity increased such that the total momentum across both slots equates, the momentum per fluid particle will be overall higher across the inlet for the the smaller slot and higher velocity case, resulting in more momentum immediately at the shear layer. To show this, cases B1 and A2 will be briefly compared, as the Reynolds number based on the jet slot is 11,654 for each. Figure 6.27 below is a comparison of the convoluted streamline visualization scenes for cases B1 and A2.

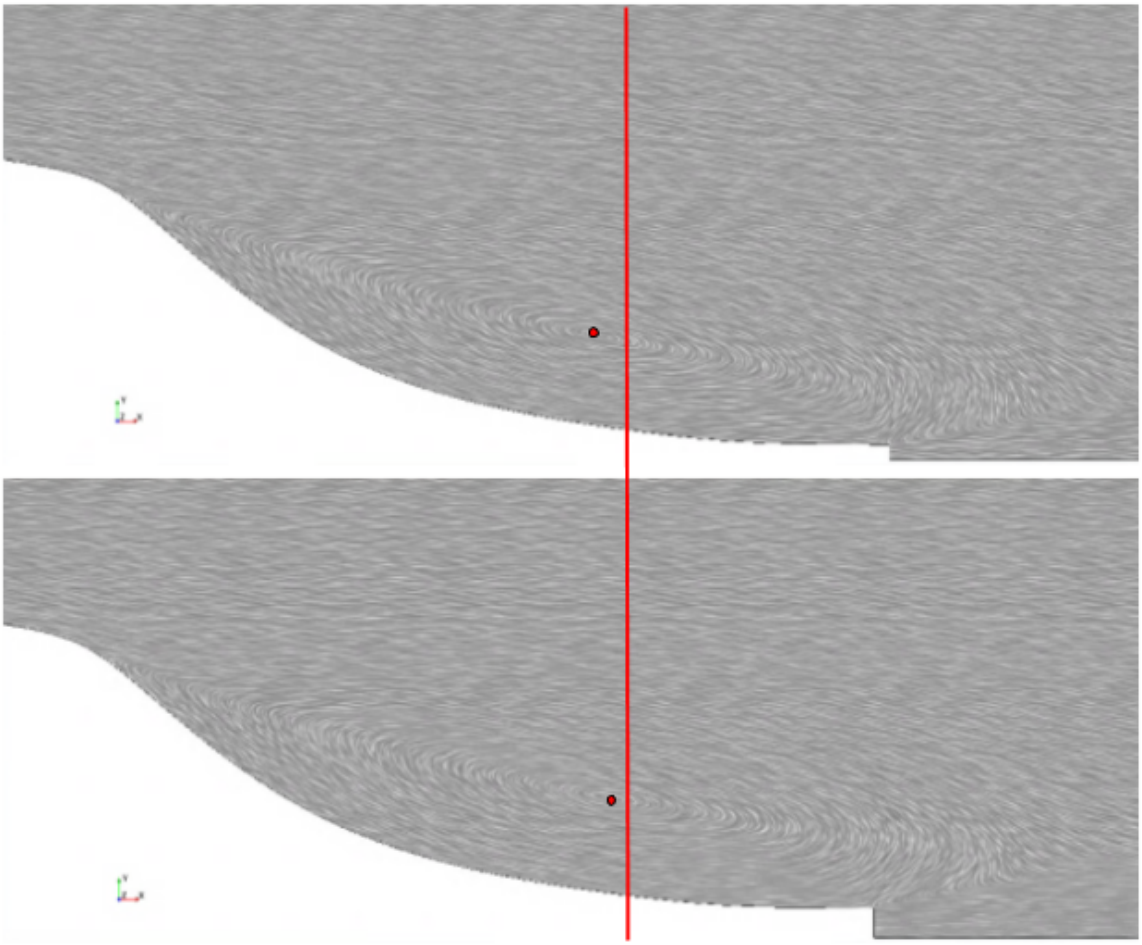

Figure 6.27: Convoluted Streamlines for Cases A2 & B1; Top A2, Bottom B1

Looking at the convoluted streamlines, it can be seen that the higher velocity case moves the eye of the bubble more forward toward the leading edge. Additionally considered is the other major mechanism influencing the recirculation zone; the vortex barrier (Figure 6.28).

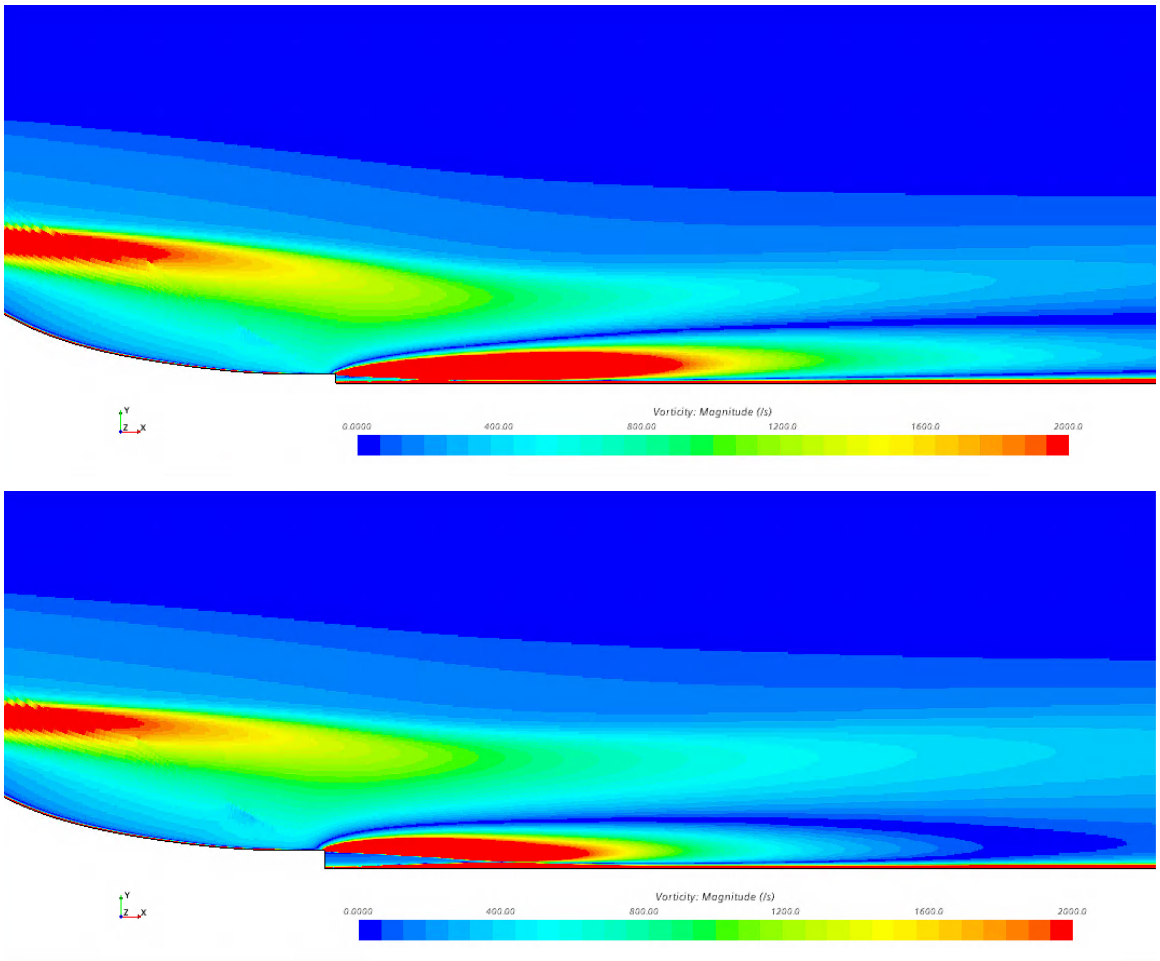

Figure 6.28: Vorticity Magnitude Scenes for Cases A2 & B1; Top A2, Bottom B1

It is seen that for constant *Re*, a higher wall jet velocity and lower slot height results in a much larger barrier, becoming much more influential on the induced drag. Aside from these two visualizations,referring to Table 6.2 shows that for constant *Re*, the higher wal jet velocity case results in a higher drag coefficient. It has also been seen throughout chapter six that all mean flow and turbulence characteristics are much more sensitive to change in wall jet velocity, leading to the conclusion that based solely on a constant Reynolds number of the wall jet inlet slot, it is clear that an increase in velocity is more influential than an increase in slot height.

CHAPTER 7: CONCLUDING REMARKS

Overall, this work provided a comprehensive, step by step process for exploring the wall-jet hump-wake flow configuration, following the framework outlined in the introduction. Major flow characteristics of the wall-jet hump-wake were identified and outlined, followed by a validation case study for each. Within the case studies, multiple RANS turbulence models were compared, resulting in a best fit model that had the ability to most accurately predict each flow. Following the validation and model selection process, simulations for the wall-jet hump-wake were constructed and scrutinized to form a good understanding of the effects of the wall jet on the hump induced wake.

The validation cases all produced workable results, but many factors and unknowns contributed to error. For example, the plots and data for [21], used as the validation case for the wall jet with a co-flowing stream, were very difficult to decipher and it is speculated that a degree of accuracy was lost in this stage. However, this was among the few experimental works to choose from for this flow configuration. While the wall jet was the best of the validation cases in terms of overall model accuracy, inlet flow conditioning may have been able to provide better results and fix the flow underdevelopment. Regarding the hump wake validation case, it is clear that the slot used for separation control in [16] and [22] was modelled incorrectly in these simulations. The work presented herein modeled the slot as a wall, as this was the simplest way to resolve a quality prism layer extrusion along the hump. However, results show large error at the slot location for both skin friction and pressure coefficients due to this. Additionally, It was noted in [22] that the Spalart-Allmaras turbulence model predicted better results for the hump wake than the k-ω model, but due to time constraints and very poor results of the wall jet and wall jet in a co-flowing stream cases for the Spalart-Allmara model, this model was not included in the

turbulence models presented for this thesis. Perhaps if time permitted, the Spalart-Allmara model could have been adjusted to produce better results than the six models presented.

As a last note on the validation cases, it is clear from the results for a multitude of tested turbulence and mean flow quantities for a range of different flow configurations that there is indeed no best model. The results in chapter four provide a striking contrast in the “best fit” for even the same flow configuration, only varying the quantity being scrutinized. Due to the large number of turbulence models tested and the multiple flow configurations, this work provides a staple example of one of the most valuable lessons in CFD modeling; there is no best turbulence model. That being said, it was a very challenging decision to make in selecting the model to use for the final simulations.

In regard to the wall-jet hump-wake flow configuration, many interesting findings were uncovered, which can be beneficial to many future works, specifically those involving flows around a road vehicle. The most eminent findings within this work were the effects of the wall jet on the recirculation zone. It was observed that increasing either studied parameter, slot height or wall jet velocity, resulted in a smaller recirculation zone. Additionally, it was found that the recirculation zone shifted forward toward the leading edge with a change in either parameter. The mechanisms driving the repositioning and resizing of the recirculation zone were uncovered to be a coupled momentum transfer along the outer layer of the wake from the induced wall jet flow with a vortex barrier near the wall jet slot. Effects of the momentum transfer were seen across approximately 90% of the hump’s body, based on the accumulated force plots as well as plots for C_P and C_F. Drag coefficients were also looked at in detail in this work, and it was found that for the specific hump wake geometry, the changes made to the wall jet that reduced the size of the recirculation zone also increased the drag coefficient, although it was explained that drag can not be applied here in a canonical sense. Thus, dependant on the specific geometry, these findings

may still present themselves as useful in respect to reducing drag via increased upstream momentum transfer from the wall jet. Finally, it was shown that increasing the wall jet velocity had more of an effect on the recirculation zone than increasing the slot height.

Aside from more accurate investigations of the wall-jet hump-wake canonical flow, it is also now feasible to take the findings derived from this work and apply them to a real-world application, such as a road vehicle model. As discussed in Chapter 1, a great focus on road vehicle aerodynamics is dedicated to drag reduction. Studies on the wall-jet hump-wake herein have shown significant effects on the recirculation zone with adjustments in the wall jet inlet characteristics. Additionally, effects were seen far upstream of the separation point, almost along the entire top of the hump geometry. The increase in wall jet velocity or slot height was shown to have positive effects on reducing drag along the top of the hump (before separation), as the pressure gradient here became more favorable and reached further toward the trailing edge with increased wall jet velocity and slot height. However, drag coefficients in the recirculation zone for each case showed a high dependence on the vortical structure created by the wall jet and it's interaction with the recirculation zone. The development of the recirculation zone and it's specific position in relation to the wall jet will differ drastically for different vehicle geometries, leading to the conclusion that the increase in drag due to increase in wall jet velocity or slot height may not be as consistent of a trend as the lower drag along the top of the body for different geometries. In summary, it was shown that the increase in wall jet velocity or slot height resulted in a lower drag along the top of the hump, a delayed separation point, and a smaller recirculation zone, all of which are very desirable and valuable effects in the overall scheme to reduce drag. The only counter-intuitive finding was the shielding of the wall jet effects in the recirculation zone near the hump wall by the wall jet vortex, which led to an increase in the drag coefficient.

The wall-jet hump-wake simulations presented within this work form a very elementary view of the flow configuration. Not only are the simulations run using RANS turbulence models, but they are also all run only in 2D. While the results presented above provide a good general structure of this flow configuration, future work should consider using higher order accuracy models, such as Detached Eddy Simulations or Large Eddy Simulations to further explore the vortex induced drag seen in this work. Perhaps an experiment is even feasible to be constructed.

BIBLIOGRAPHY

[1] Abe, K., T. Kondoh, and Y. Nagano. "A new turbulence model for predicting fluid flow and heat transfer in separating and reattaching flows—I. Flow field calculations." *International journal of heat and mass transfer* 37, no. 1 (1994): 139-151.

[2] Ayech, Syrine Ben Haj, Sabra Habli, Nejla Mahjoub Saïd, Hervé Bournot, and George Le Palec. "Effect of the coflow stream on a plane wall jet." *Heat and Mass Transfer* 50, no. 12 (2014): 1685-1697.

[3] Bradshaw, P. G. E. E., and M. T. Gee. *Turbulent wall jets with and without an external stream*. Vol. 22, no. 008. ARC, 1960.

[4] Brown, James. "Shock wave impingement on boundary layers at hypersonic speeds: computational analysis and uncertainty." In *42nd AIAA Thermophysics Conference*, p. 3143. 2011.

[5] Campbell, James Franklin. "Turbulent wall jet in a coflowing stream." (1975).

[6] Dejoan, A., and M. A. Leschziner. "Large eddy simulation of a plane turbulent wall jet." *Physics of Fluids* 17, no. 2 (2005): 025102.

[7] Durbin, Paul A. "Near-wall turbulence closure modeling without “damping functions”." *Theoretical and computational fluid dynamics* 3, no. 1 (1991): 1-13.

[8] Durbin, Paul A. "Separated flow computations with the k-epsilon-v-squared model." *AIAA journal* 33, no. 4 (1995): 659-664.

[9] Ehirim, O. H., K. Knowles, and A. J. Saddington. "A Review of Ground-Effect Diffuser Aerodynamics." *Journal of Fluids Engineering* 141, no. 2 (2019).

[10] Eriksson, J. G., R. I. Karlsson, and J. Persson. "An experimental study of a two-dimensional plane turbulent wall jet." *Experiments in fluids* 25, no. 1 (1998): 50-60.

[11] Fernholz, H. H., and D. Warnack. "The effects of a favourable pressure gradient and of the Reynolds number on an incompressible axisymmetric turbulent boundary layer. Part 1. The turbulent boundary layer." *Journal of Fluid Mechanics* 359 (1998): 329-356.

[12] Franck, Jennifer Ann. "Large-eddy simulation of flow separation and control on a wall-mounted hump." PhD diss., California Institute of Technology, 2009.

[13] Franck, Jennifer A., and Tim Colonius. "Compressible large-eddy simulation of separation control on a wall-mounted hump." AIAA journal 48, no. 6 (2010): 1098-1107.

[14] Fu, Chen, Mesbah Uddin, and Alex Curley. "Insights derived from CFD studies on the evolution of planar wall jets." *Engineering Applications of Computational Fluid Mechanics* 10, no. 1 (2016): 44-56.

[15] George, William K., Hans Abrahamsson, Jan Eriksson, Rolf I. Karlsson, Lennart Löfdahl, and Martin Wosnik. "A similarity theory for the turbulent plane wall jet without external stream." *Journal of Fluid Mechanics* 425 (2000): 367-411.

[16] Greenblatt, David, Keith B. Paschal, Chung-Sheng Yao, Jerome Harris, Norman W. Schaeffler, and Anthony E. Washburn. "Experimental investigation of separation control part 1: baseline and steady suction." *AIAA journal* 44, no. 12 (2006): 2820-2830.

[17] Greenblatt, D., Paschal, K. B., Yao, C.-S., Harris, J., "Experimental Investigation of Separation Control Part 2: Zero Mass-Flux Oscillatory Blowing," AIAA Journal, Vol. 44, No. 12, 2006, pp. 2831-2845, http://arc.aiaa.org/doi/abs/10.2514/1.19324.

[18] Guilmineau, E., G. B. Deng, A. Leroyer, P. Queutey, M. Visonneau, and J. Wackers. "Assessment of hybrid RANS-LES formulations for flow simulation around the Ahmed body." *Computers & Fluids* 176 (2018): 302-319.

[19] Jensen, Karl Karl Eugene. "Aerodynamic undertray design for formula SAE." (2010).

[20] Jones, W. P., and BrnE Launder. "The calculation of low-Reynolds-number phenomena with a two-equation model of turbulence." *International Journal of Heat and Mass Transfer* 16, no. 6 (1973): 1119-1130.

[21] Kacker, S. C., and J. H. Whitelaw. "The turbulence characteristics of two-dimensional wall-jet and wall-wake flows." (1971): 239-252.

[22] Langley Research Center Workshop. “CFD Validation of Synthetic Jets and Turbulent Separation Control, Case 3.” (2004) Accessed 4/5/2020, <https://cfdval2004.larc.nasa.gov/case3.html>

[23] Launder, B. E., and Wolfgang Rodi. "The turbulent wall jet." *Progress in Aerospace Sciences* 19 (1979): 81-128.

[24] Launder, B. E., and W. Rodi. "The turbulent wall jet measurements and modeling." *Annual review of fluid mechanics* 15, no. 1 (1983): 429-459.

[25] Laurence, D. R., J. C. Uribe, and S. V. Utyuzhnikov. "A robust formulation of the v2− (f) model." *Flow, Turbulence and Combustion* 73, no. 3-4 (2005): 169-185.

[26] Lyons, Daniel C., Leonard J. Peltier, Frank J. Zajaczkowski, and Eric G. Paterson. "Assessment of DES models for separated flow from a hump in a turbulent boundary layer." *Journal of fluids engineering* 131, no. 11 (2009).

[27] Manceau, Rémi, and Kemal Hanjalić. "Elliptic blending model: A new near-wall Reynolds-stress turbulence closure." *Physics of Fluids* 14, no. 2 (2002): 744-754.

[28] Menter, Florianr. "Zonal two equation kw turbulence models for aerodynamic flows." In *23rd fluid dynamics, plasmadynamics, and lasers conference*, p. 2906. 1993.

[29] Menter, Florian R. "Review of the shear-stress transport turbulence model experience from an industrial perspective." *International journal of computational fluid dynamics* 23, no. 4 (2009): 305-316.

[30] Menter, Florian R., Pavel E. Smirnov, Tao Liu, and Ravikanth Avancha. "A one-equation local correlation-based transition model." *Flow, Turbulence and Combustion* 95, no. 4 (2015): 583-619.

[31] Naqavi, Iftekhar Z., Paul G. Tucker, and Yan Liu. "Large-eddy simulation of the interaction of wall jets with external stream." *International journal of heat and fluid flow* 50 (2014): 431-444.

[32] Naqavi, I. Z., and P. G. Tucker. "Large-Eddy Simulation of the Interaction of Wall Jets with External Stream." In *Direct and Large-Eddy Simulation IX*, pp. 259-266. Springer, Cham, 2015.

[33] Naughton, J. W., Viken, S. A., Greenblatt, D., "Skin-Friction Measurements on the NASA Hump Model," AIAA Journal, Vol. 44, No. 6, 2006, pp. 1255-1265, http://arc.aiaa.org/doi/abs/10.2514/1.14192.

[34] Rodi, Wolfgang. "Experience with two-layer models combining the k-epsilon model with a one-equation model near the wall." In *29th Aerospace sciences meeting*, p. 216. 1991.

[35] Sagol, Ece, Marcelo Reggio, and Adrian Ilinca. "Assessment of two-equation turbulence models and validation of the performance characteristics of an experimental wind turbine by CFD." *ISRN Mechanical Engineering* 2012 (2012).

[36] Schumann, Ulrich. "Realizability of Reynolds-stress turbulence models." *The Physics of Fluids* 20, no. 5 (1977): 721-725.

[37] Shih, Tsan-Hsing, Jiang Zhu, and John L. Lumley. "A new Reynolds stress algebraic equation model." *Computer methods in applied mechanics and engineering* 125, no. 1-4 (1995): 287-302.

[38] Shih, Tsan-Hsing, William W. Liou, Aamir Shabbir, Zhigang Yang, and Jiang Zhu. "A new k-ϵ eddy viscosity model for high Reynolds number turbulent flows." *Computers & fluids* 24, no. 3 (1995): 227-238

[39] STAR CCM+ Users Manual. http://www.cd-adapco.com/products/star-ccm/documentation

[40] Tennekes, Hendrik, and John L. Lumley. *A first course in turbulence*. MIT press, 2018.

[41] Uddin, M., A. Pollard, and J. Braly. "Large eddy simulation of 3D Square Wall jets." In *12th Annual Conference of the CFD Society of Canada*. 2004.

APPENDIX

Table A.1: Wall Jet Validation Case Boundary Conditions

Domain Top	Domain Outlet	Domain Bottom	Domain Inlet	Jet Inlet
Pressure Outlet	Pressure Outlet	Wall	Wall	Velocity Inlet

Table A.2: Wall Jet in a Co-Flowing Stream Validation Case Boundary Conditions

Domain Top	Domain Outlet	Domain Bottom	Splitter Plane	Jet Inlet	Stream Inlet
Symmetry Plane	Pressure Outlet	Wall	Wall	Velocity Inlet	Velocity Inlet

Table A.3: NASA Hump Wake Validation Case Boundary Conditions

Domain Top	Domain Outlet	Upstream Wall	Hump	Downstream Wall	Domain Inlet
Wall	Pressure Outlet	Wall	Wall	Wall	Velocity Inlet

Table A.4: Wall-Jet Hump-Wake Validation Case Boundary Conditions

Domain Top	Domain Outlet	Upstream Wall	Hump	Downstream Wall	Domain Inlet	Jet Slot
Pressure Outlet	Pressure Outlet	Wall	Wall	Wall	Velocity Inlet	Velocity Inlet

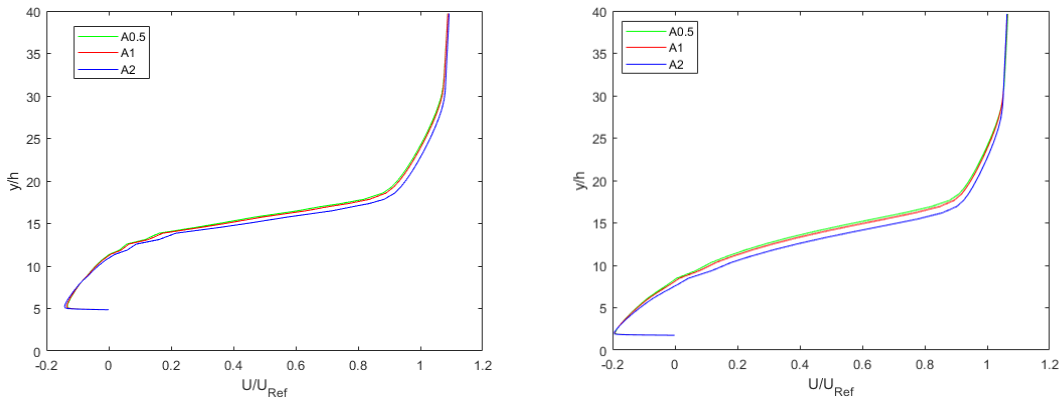

(a) (b)

Figure A.1: Wall-Jet Hump-Wake Velocity Profiles Grouped by *h* for Cases A0.5-A2; (a) *x/c*=0.8, (b) *x/c*=0.9, (c) *x/c*=1.0, (d) *x/c*=1.1, (e) *x/c*=1.2, (f) *x/c*=1.3, (g) *x/c*=1.4, (h) *x/c*=1.5, (i) *x/c*=2.0, (j) *x/c*=2.5, (k) *x/c*=3.0

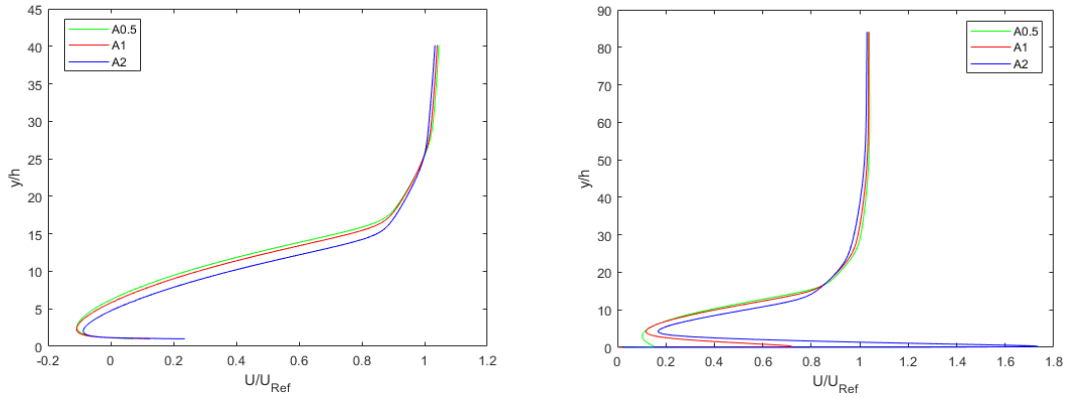

(c) (d)

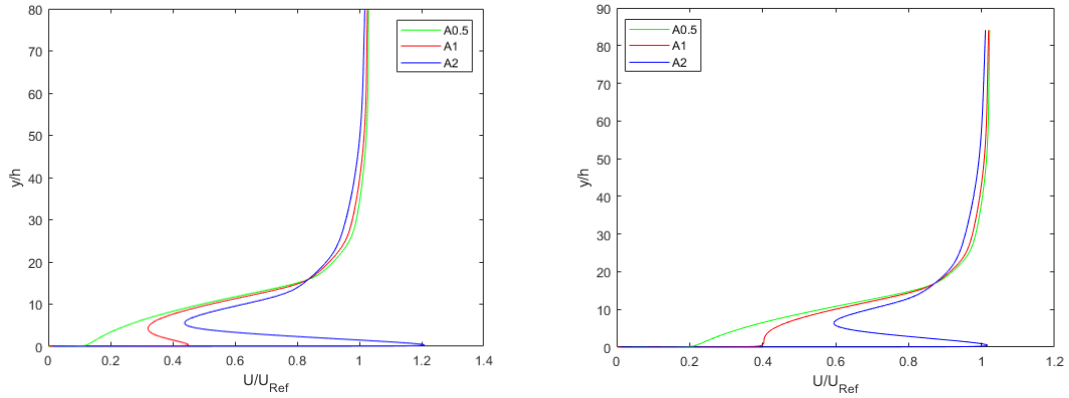

(e) (f)

Figure A.1 (Continued): Wall-Jet Hump-Wake Velocity Profiles Grouped by *h* for Cases A0.5-A2; (a) *x/c*=0.8, (b) *x/c*=0.9, (c) *x/c*=1.0, (d) *x/c*=1.1, (e) *x/c*=1.2, (f) *x/c*=1.3, (g) *x/c*=1.4, (h) *x/c*=1.5, (i) *x/c*=2.0, (j) *x/c*=2.5, (k) *x/c*=3.0

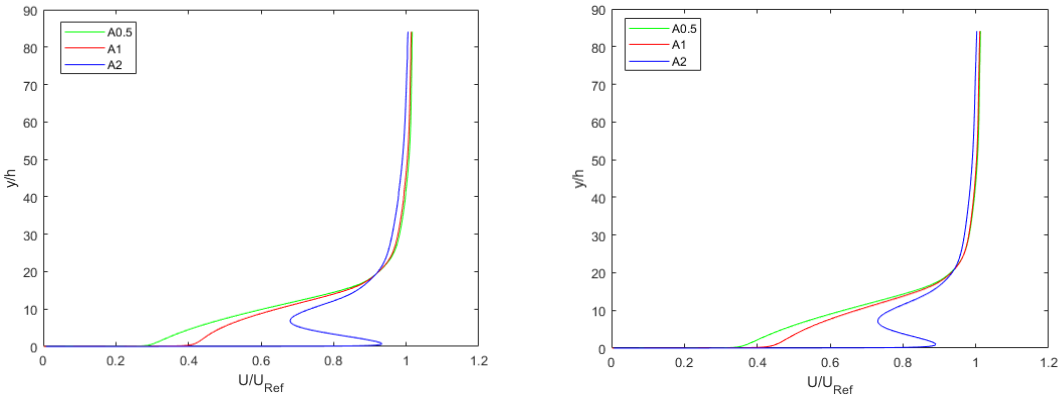

(g) (h)

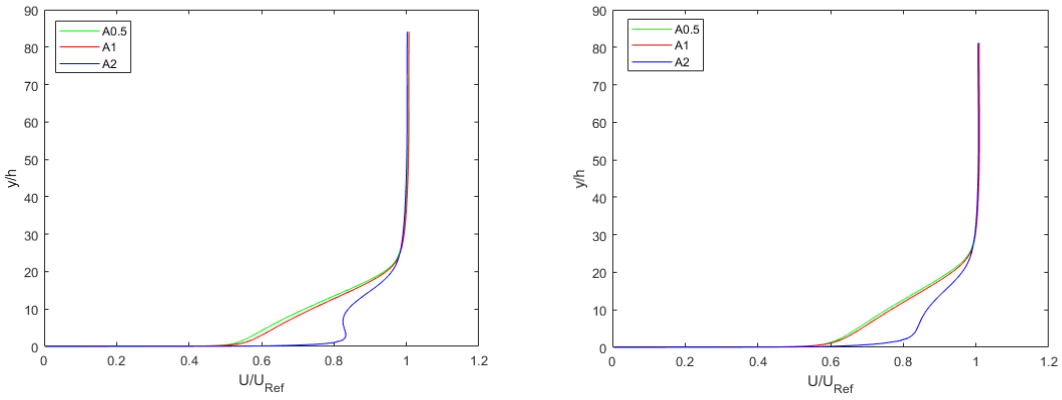

(i) (j)

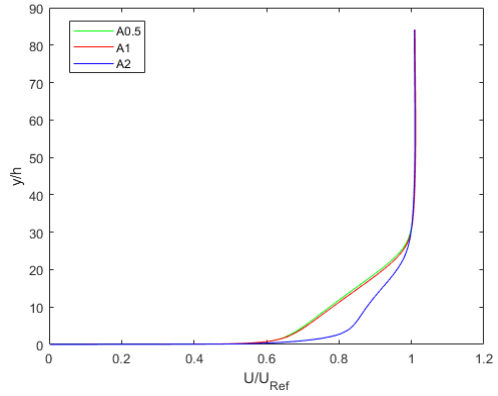

(k)

Figure A.1 (Continued): Wall-Jet Hump-Wake Velocity Profiles Grouped by *h* for Cases A0.5-A2; (a) *x/c*=0.8, (b) *x/c*=0.9, (c) *x/c*=1.0, (d) *x/c*=1.1, (e) *x/c*=1.2, (f) *x/c*=1.3, (g) *x/c*=1.4, (h) *x/c*=1.5, (i) *x/c*=2.0, (j) *x/c*=2.5, (k) *x/c*=3.0

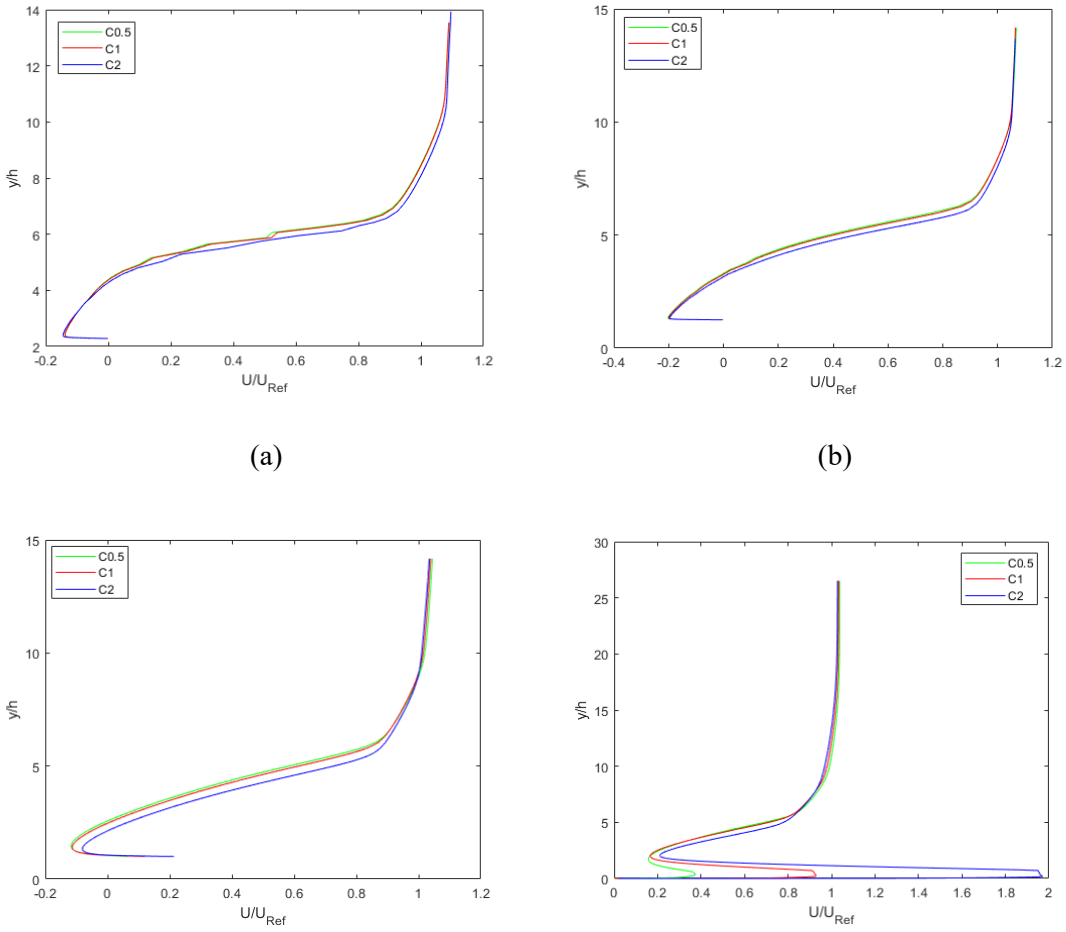

Figure A.2: Wall-Jet Hump-Wake Velocity Profiles Grouped by *h* for Cases C0.5-C2; (a) *x/c*=0.8, (b) *x/c*=0.9, (c) *x/c*=1.0, (d) *x/c*=1.1, (e) *x/c*=1.2, (f) *x/c*=1.3, (g) *x/c*=1.4, (h) *x/c*=1.5, (i) *x/c*=2.0, (j) *x/c*=2.5, (k) *x/c*=3.0

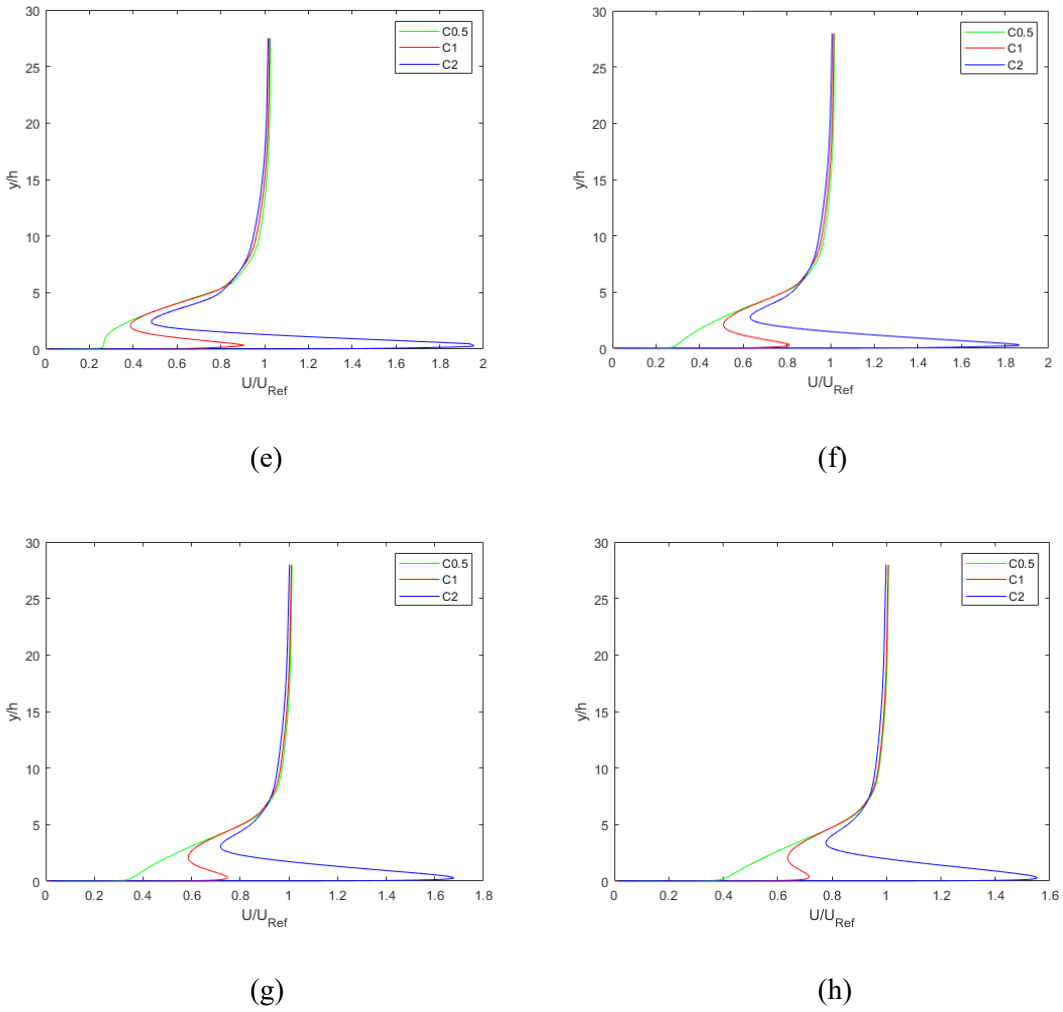

Figure A.2 (Continued): Wall-Jet Hump-Wake Velocity Profiles Grouped by *h* for Cases C0.5-C2; (a) *x/c*=0.8, (b) *x/c*=0.9, (c) *x/c*=1.0, (d) *x/c*=1.1, (e) *x/c*=1.2, (f) *x/c*=1.3, (g) *x/c*=1.4, (h) *x/c*=1.5, (i) *x/c*=2.0, (j) *x/c*=2.5, (k) *x/c*=3.0

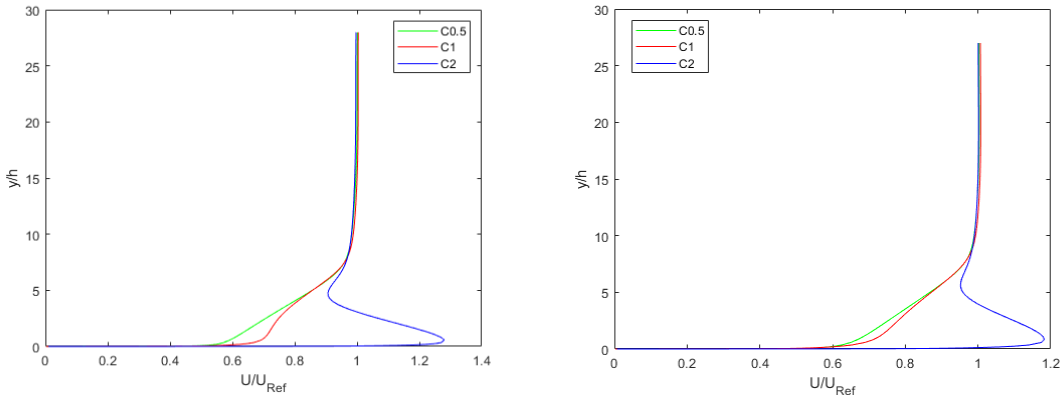

(i) (j)

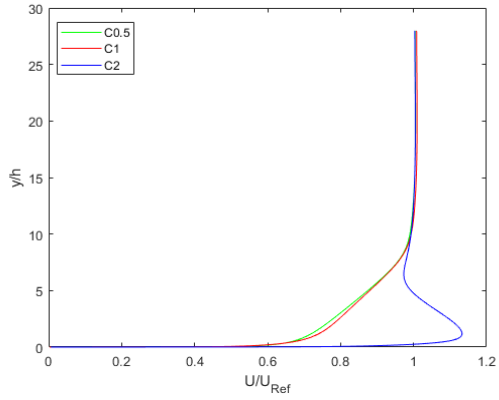

(k)

Figure A.2 (Continued): Wall-Jet Hump-Wake Velocity Profiles Grouped by *h* for Cases C0.5-C2; (a) *x/c*=0.8, (b) *x/c*=0.9, (c) *x/c*=1.0, (d) *x/c*=1.1, (e) *x/c*=1.2, (f) *x/c*=1.3, (g) *x/c*=1.4, (h) *x/c*=1.5, (i) *x/c*=2.0, (j) *x/c*=2.5, (k) *x/c*=3.0

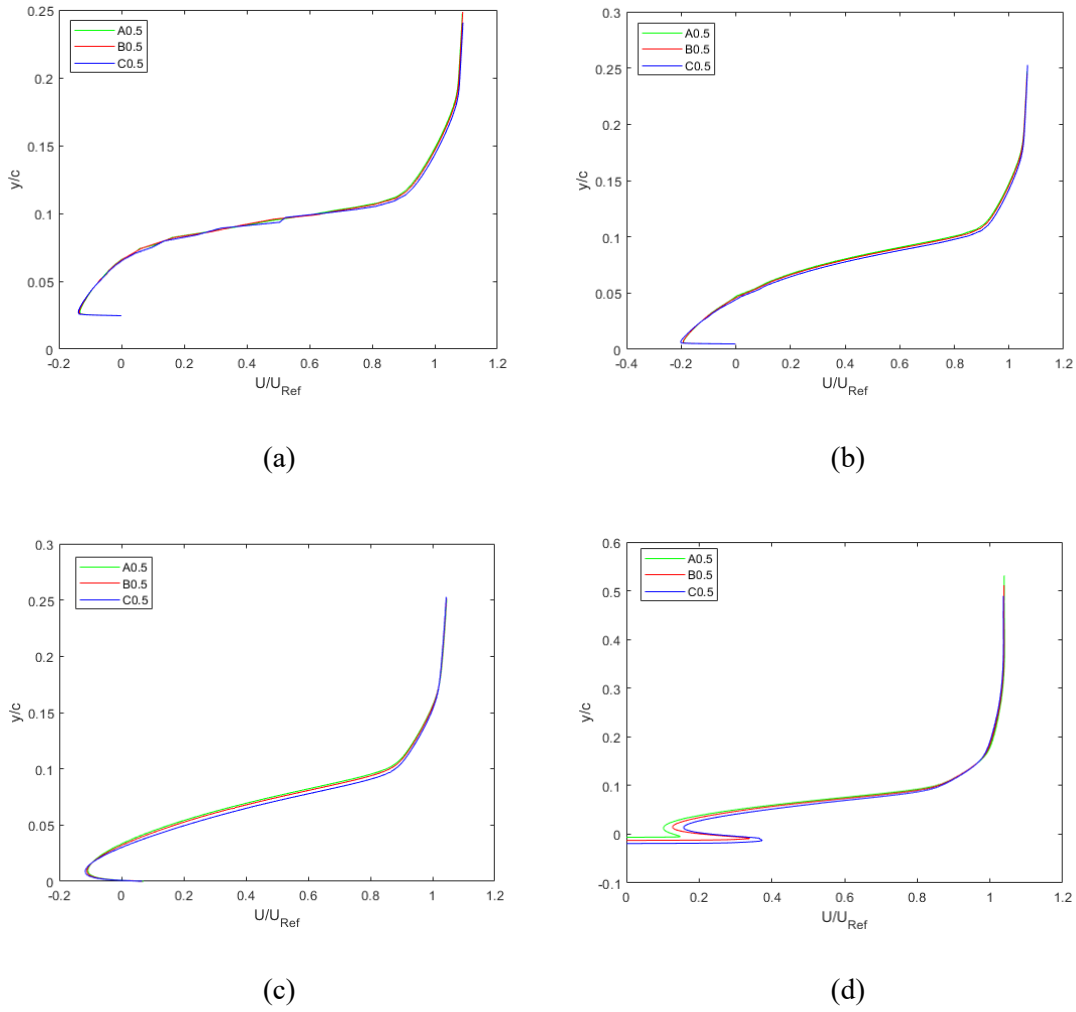

Figure A.3: Wall-Jet Hump-Wake Velocity Profiles Grouped by U_J/U_S for Cases A0.5, B0.5, & C0.5; (a) x/c=0.8, (b) x/c=0.9, (c) x/c=1.0, (d) x/c=1.1, (e) x/c=1.2, (f) x/c=1.3, (g) x/c=1.4, (h) x/c=1.5, (i) x/c=2.0, (j) x/c=2.5, (k) x/c=3.0

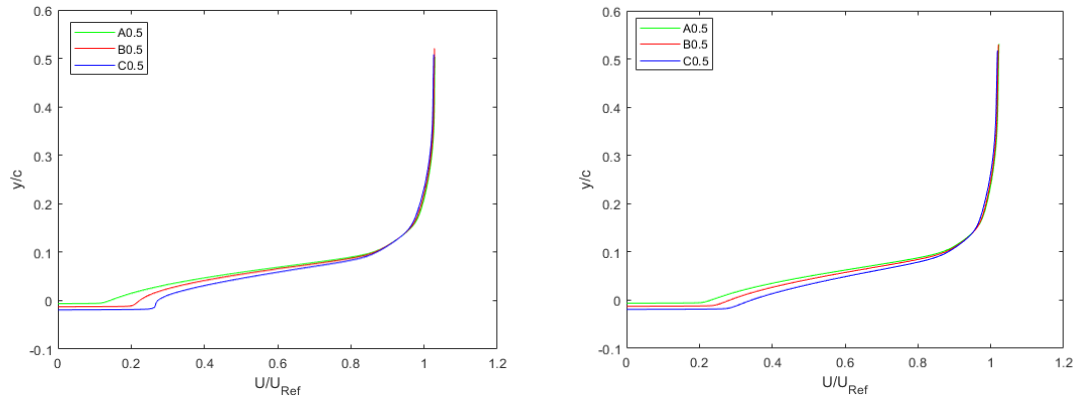

(e) (f)

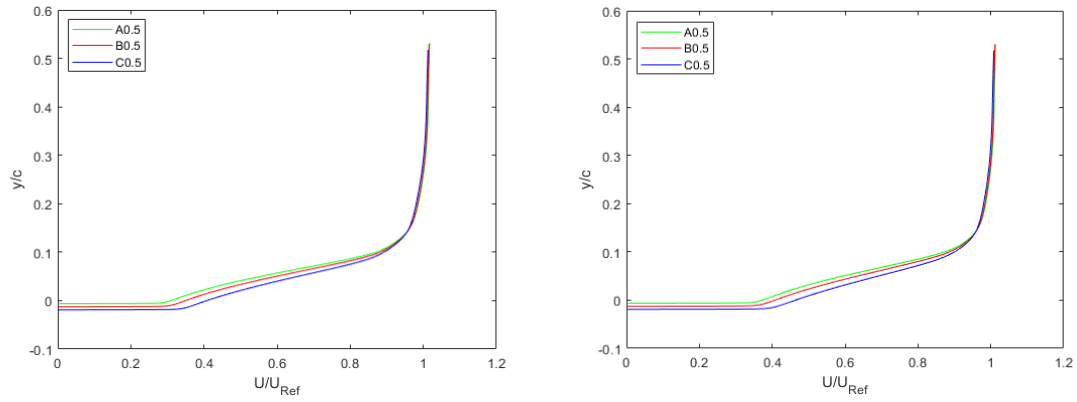

(g) (h)

Figure A.3 (Continued): Wall-Jet Hump-Wake Velocity Profiles Grouped by U_J/U_S for Cases A0.5, B0.5, & C0.5; (a) x/c=0.8, (b) x/c=0.9, (c) x/c=1.0, (d) x/c=1.1, (e) x/c=1.2, (f) x/c=1.3, (g) x/c=1.4, (h) x/c=1.5, (i) x/c=2.0, (j) x/c=2.5, (k) x/c=3.0

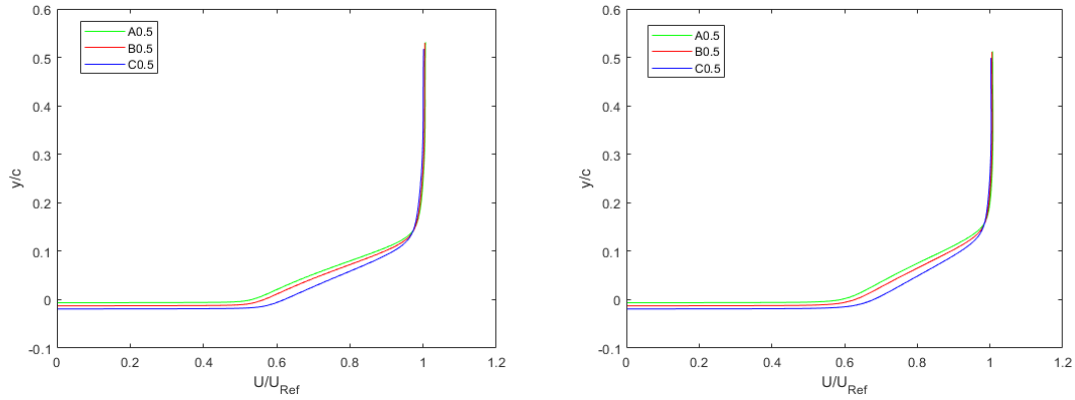

(i) (j)

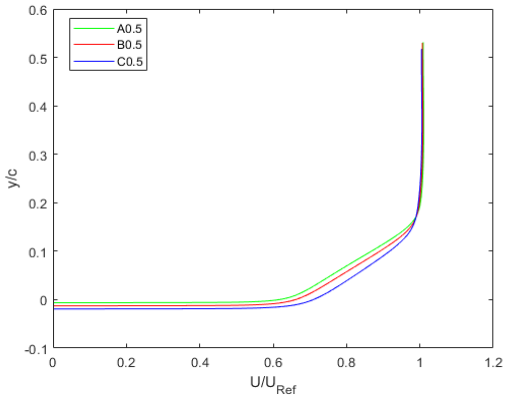

(k)

Figure A.3 (Continued): Wall-Jet Hump-Wake Velocity Profiles Grouped by U_J/U_S for Cases A0.5, B0.5, & C0.5; (a) *x/c*=0.8, (b) *x/c*=0.9, (c) *x/c*=1.0, (d) *x/c*=1.1, (e) *x/c*=1.2, (f) *x/c*=1.3, (g) *x/c*=1.4, (h) *x/c*=1.5, (i) *x/c*=2.0, (j) *x/c*=2.5, (k) *x/c*=3.0

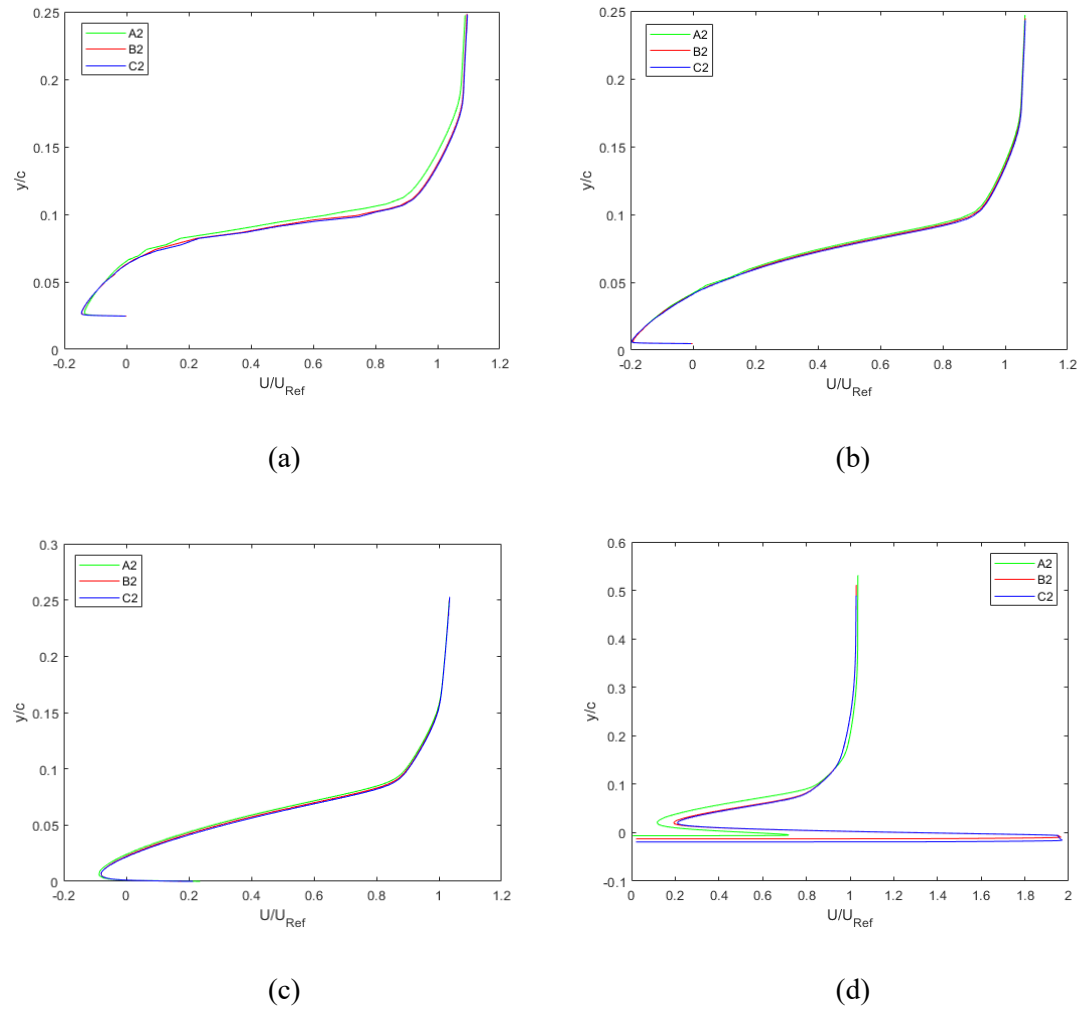

Figure A.4: Wall-Jet Hump-Wake Velocity Profiles Grouped by U_J/U_S for Cases A2, B2, & C2; (a) x/c=0.8, (b) x/c=0.9, (c) x/c=1.0, (d) x/c=1.1, (e) x/c=1.2, (f) x/c=1.3, (g) x/c=1.4, (h) x/c=1.5, (i) x/c=2.0, (j) x/c=2.5, (k) x/c=3.0

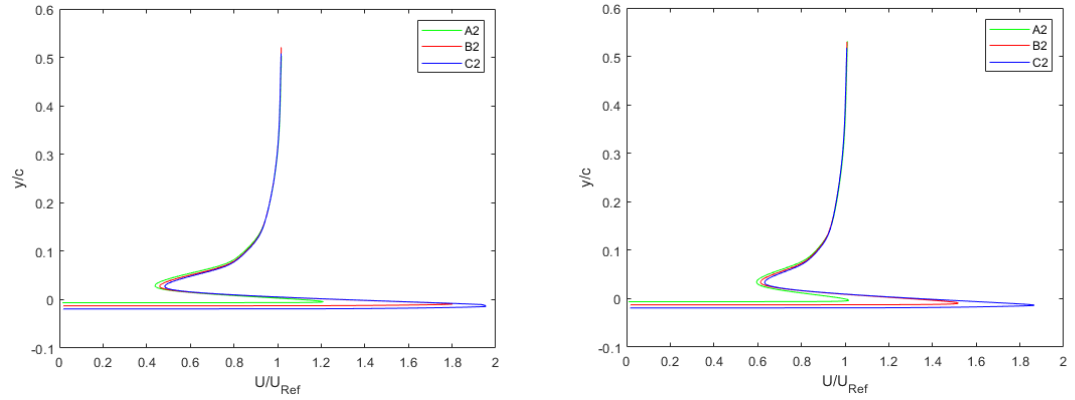

(e) (f)

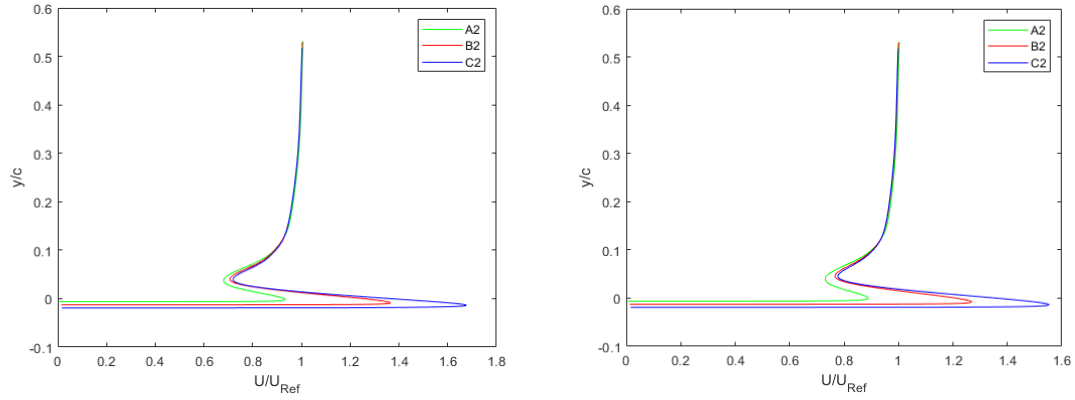

(g) (h)

Figure A.4 (Continued): Wall-Jet Hump-Wake Velocity Profiles Grouped by U_J/U_S for Cases A2, B2, & C2; (a) x/c=0.8, (b) x/c=0.9, (c) x/c=1.0, (d) x/c=1.1, (e) x/c=1.2, (f) x/c=1.3, (g) x/c=1.4, (h) x/c=1.5, (i) x/c=2.0, (j) x/c=2.5, (k) x/c=3.0

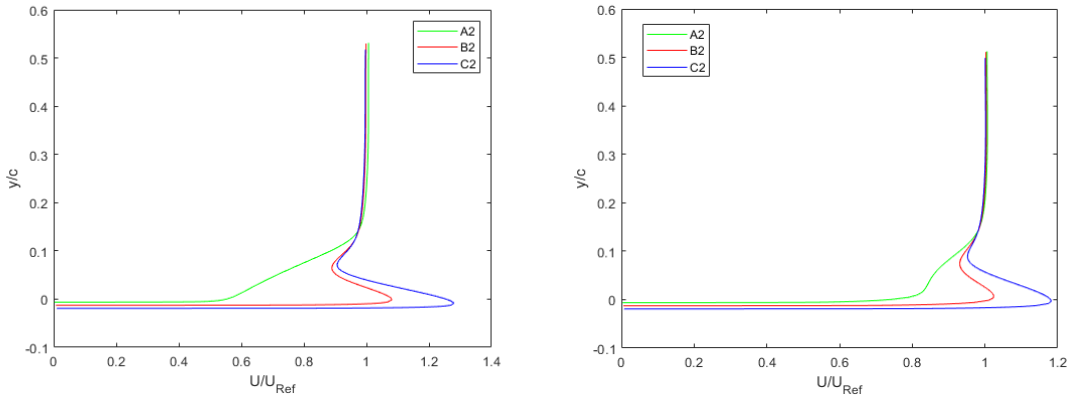

(i) (j)

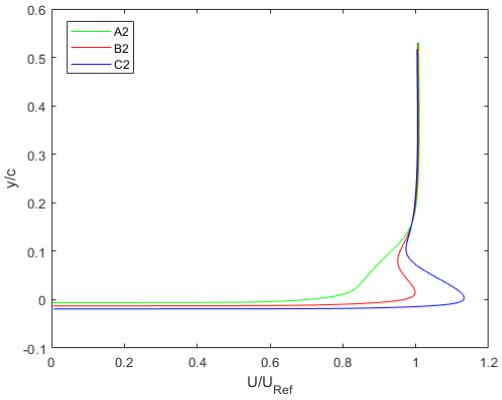

(k)

Figure A.4 (Continued): Wall-Jet Hump-Wake Velocity Profiles Grouped by U_J/U_S for Cases A2, B2, & C2; (a) *x/c*=0.8, (b) *x/c*=0.9, (c) *x/c*=1.0, (d) *x/c*=1.1, (e) *x/c*=1.2, (f) *x/c*=1.3, (g) *x/c*=1.4, (h) *x/c*=1.5, (i) *x/c*=2.0, (j) *x/c*=2.5, (k) *x/c*=3.0

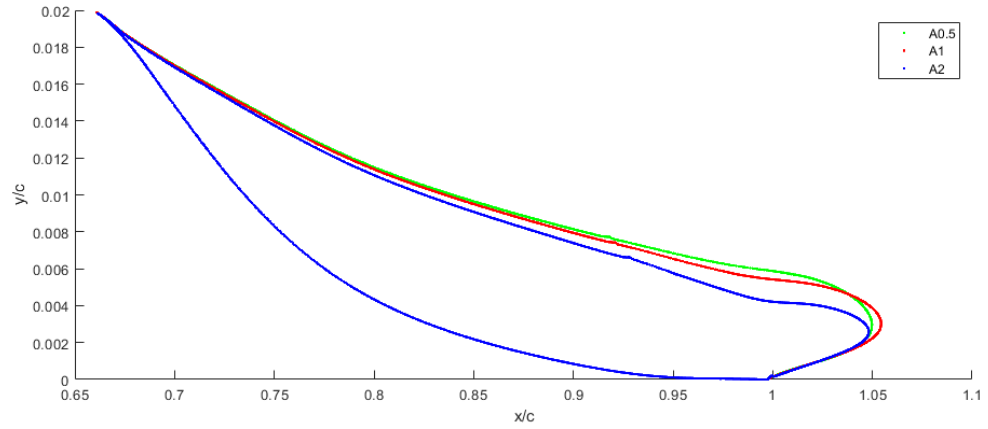

Figure A.5: Wall-Jet Hump-Wake Recirculation Perimeter for Cases A0.5-A2

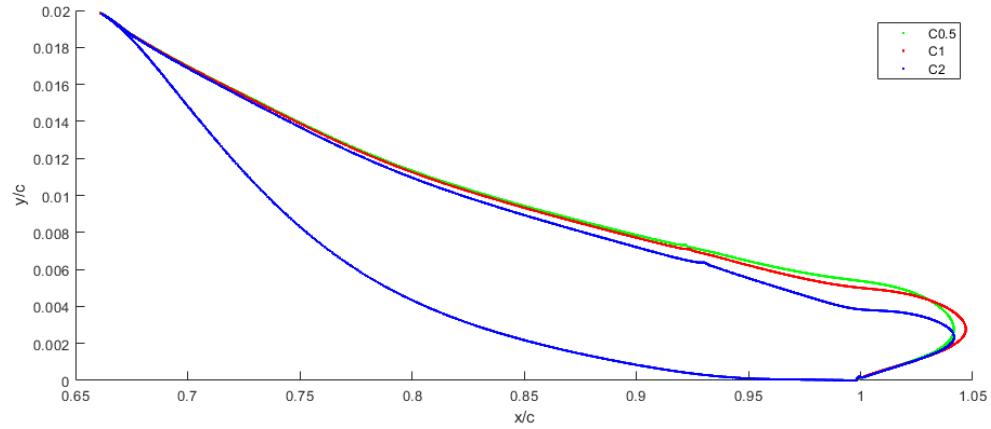

Figure A.6: Wall-Jet Hump-Wake Recirculation Perimeter for Cases C0.5-C2

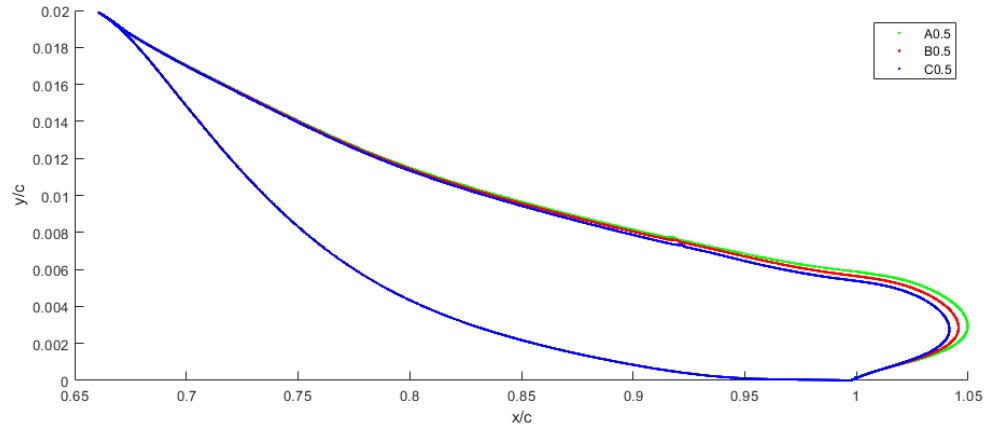

Figure A.7: Wall-Jet Hump-Wake Recirculation Perimeter for Cases A0.5-C0.5

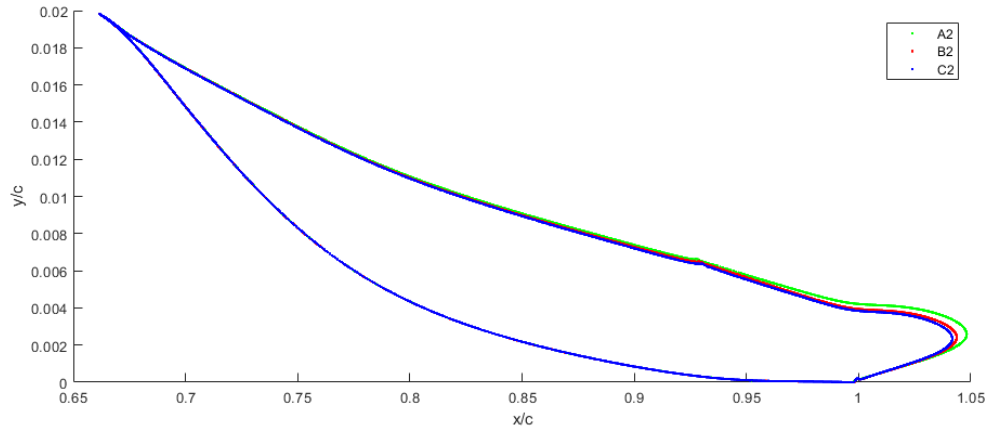

Figure A.8: Wall-Jet Hump-Wake Recirculation Perimeter for Cases A2-C2

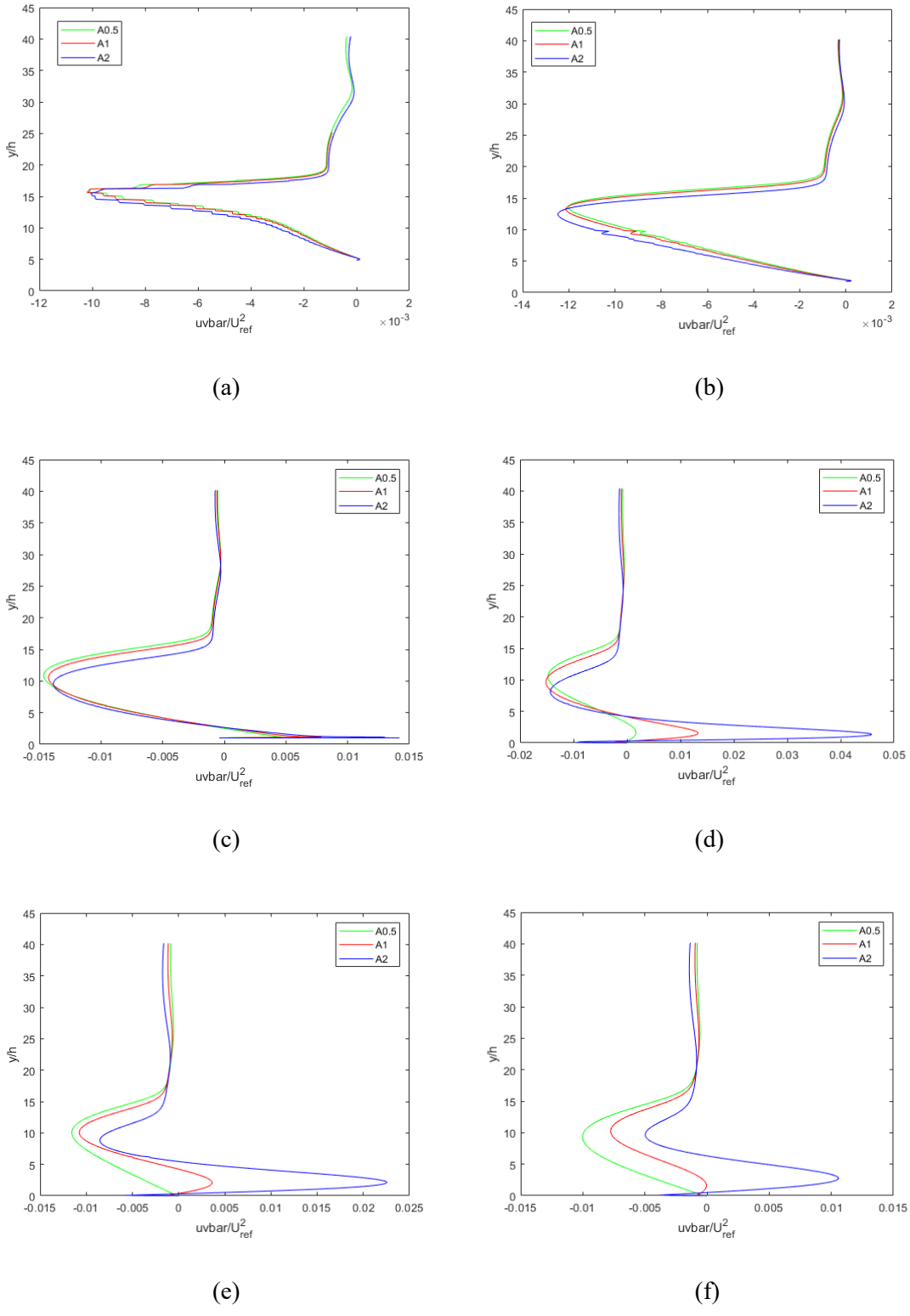

Figure A.9: Wall-Jet Hump-Wake Reynolds Stress Profiles Grouped by *h* for Cases A0.5, A1, & A2; (a) *x/c*=0.8, (b) *x/c*=0.9, (c) *x/c*=1.0, (d) *x/c*=1.1, (e) *x/c*=1.2, (f) *x/c*=1.3, (g) *x/c*=1.4, (h) *x/c*=1.5

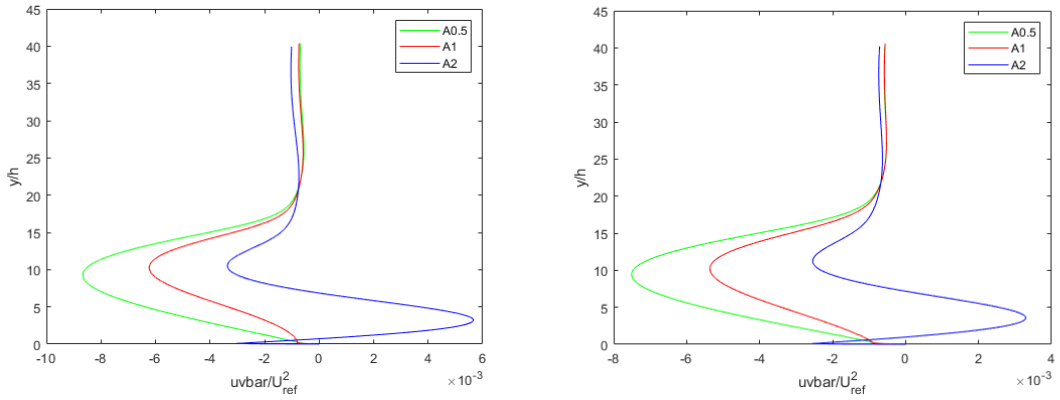

(g) (h)

Figure A.9 (Continued): Wall-Jet Hump-Wake Reynolds Stress Profiles Grouped by *h* for Cases A0.5, A1, & A2; (a) *x/c*=0.8, (b) *x/c*=0.9, (c) *x/c*=1.0, (d) *x/c*=1.1, (e) *x/c*=1.2, (f) *x/c*=1.3, (g) *x/c*=1.4, (h) *x/c*=1.5

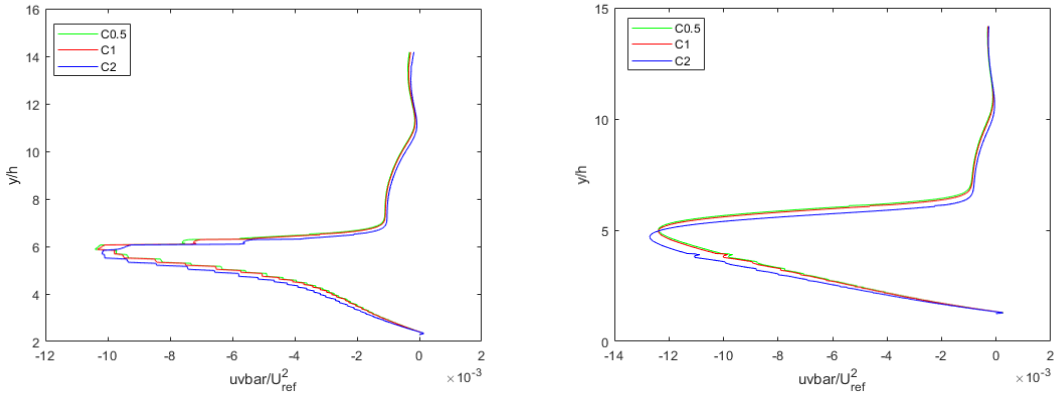

(a) (b)

Figure A.10: Wall-Jet Hump-Wake Reynolds Stress Profiles Grouped by *h* for Cases C0.5, C1, & C2; (a) *x/c*=0.8, (b) *x/c*=0.9, (c) *x/c*=1.0, (d) *x/c*=1.1, (e) *x/c*=1.2, (f) *x/c*=1.3, (g) *x/c*=1.4, (h) *x/c*=1.5

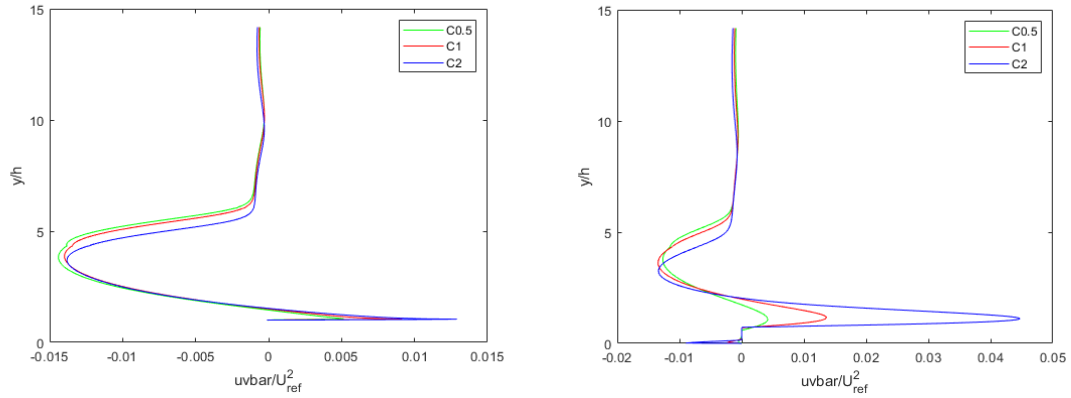

(c) (d)

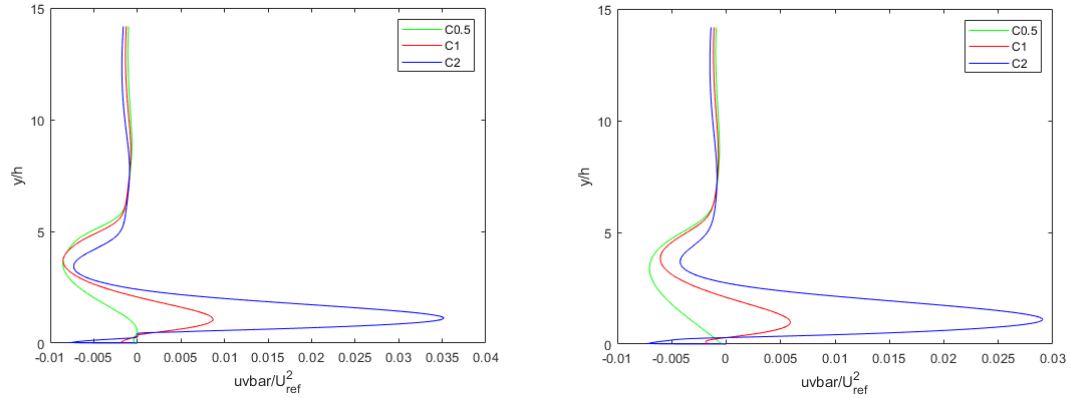

(e) (f)

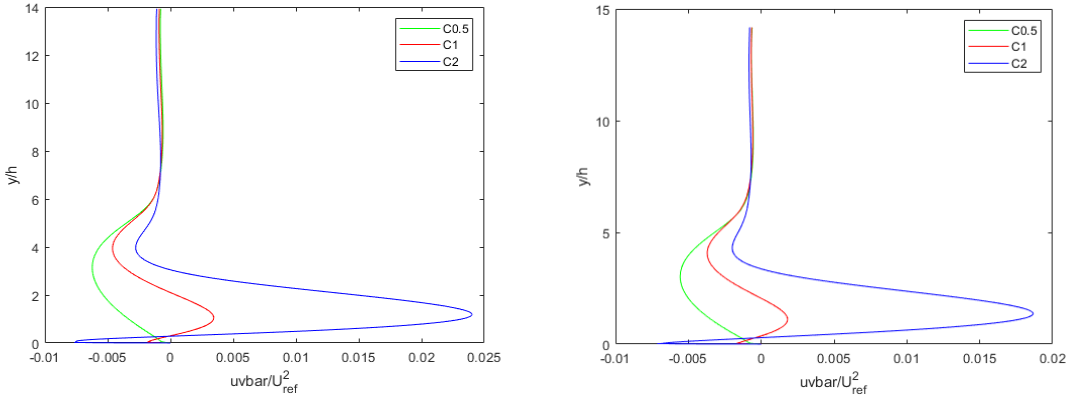

(g) (h)

Figure A10 (Continued): Wall-Jet Hump-Wake Reynolds Stress Profiles Grouped by *h* for Cases C0.5, C1, & C2; (a) *x/c*=0.8, (b) *x/c*=0.9, (c) *x/c*=1.0, (d) *x/c*=1.1, (e) *x/c*=1.2, (f) *x/c*=1.3, (g) *x/c*=1.4, (h) *x/c*=1.5

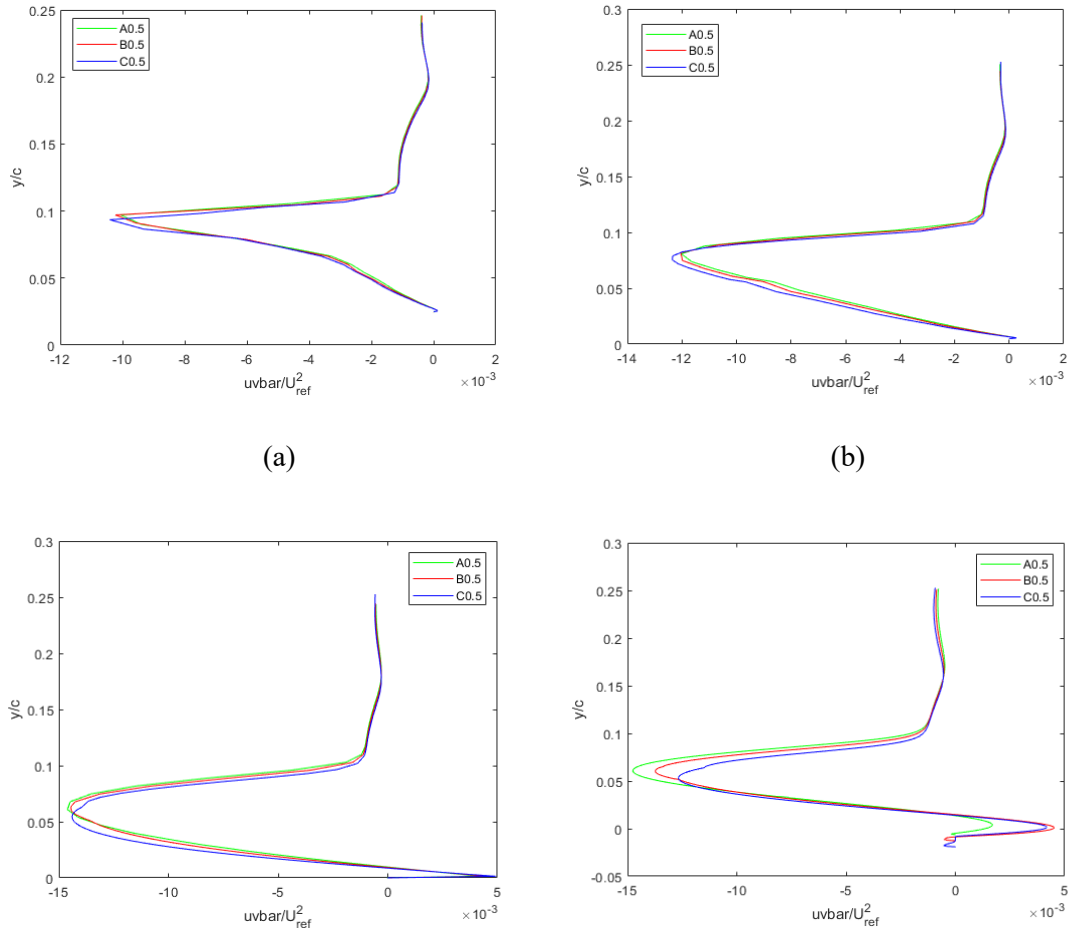

Figure A.11: Wall-Jet Hump-Wake Reynolds Stress Profiles Grouped by U_f/U_S for Cases A0.5, B0.5, & C0.5; (a) x/c=0.8, (b) x/c=0.9, (c) x/c=1.0, (d) x/c=1.1, (e) x/c=1.2, (f) x/c=1.3, (g) x/c=1.4, (h) x/c=1.5

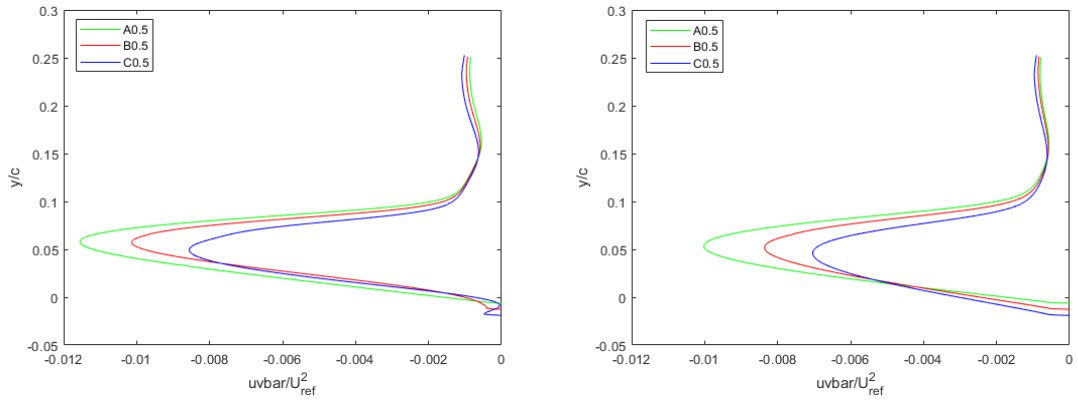

(e) (f)

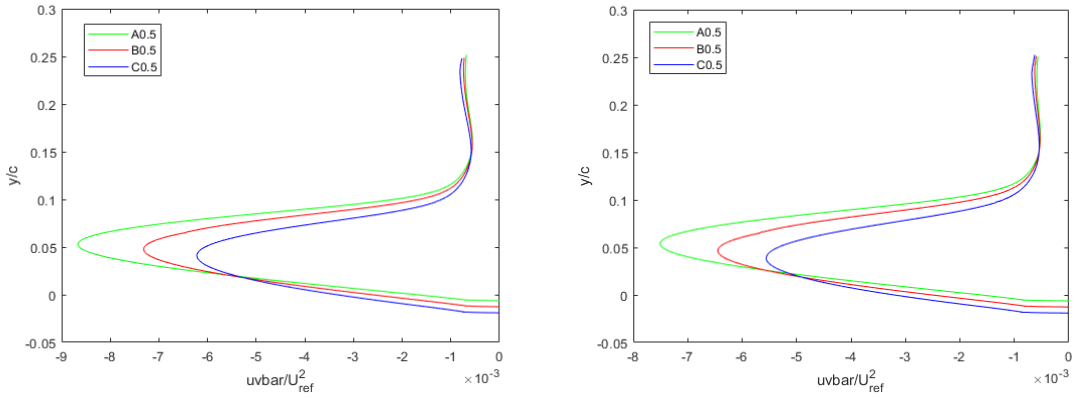

(g) (h)

Figure A.11 (Continued): Wall-Jet Hump-Wake Reynolds Stress Profiles Grouped by U_J/U_S for Cases A0.5, B0.5, & C0.5; (a) x/c=0.8, (b) x/c=0.9, (c) x/c=1.0, (d) x/c=1.1, (e) x/c=1.2, (f) x/c=1.3, (g) x/c=1.4, (h) x/c=1.5

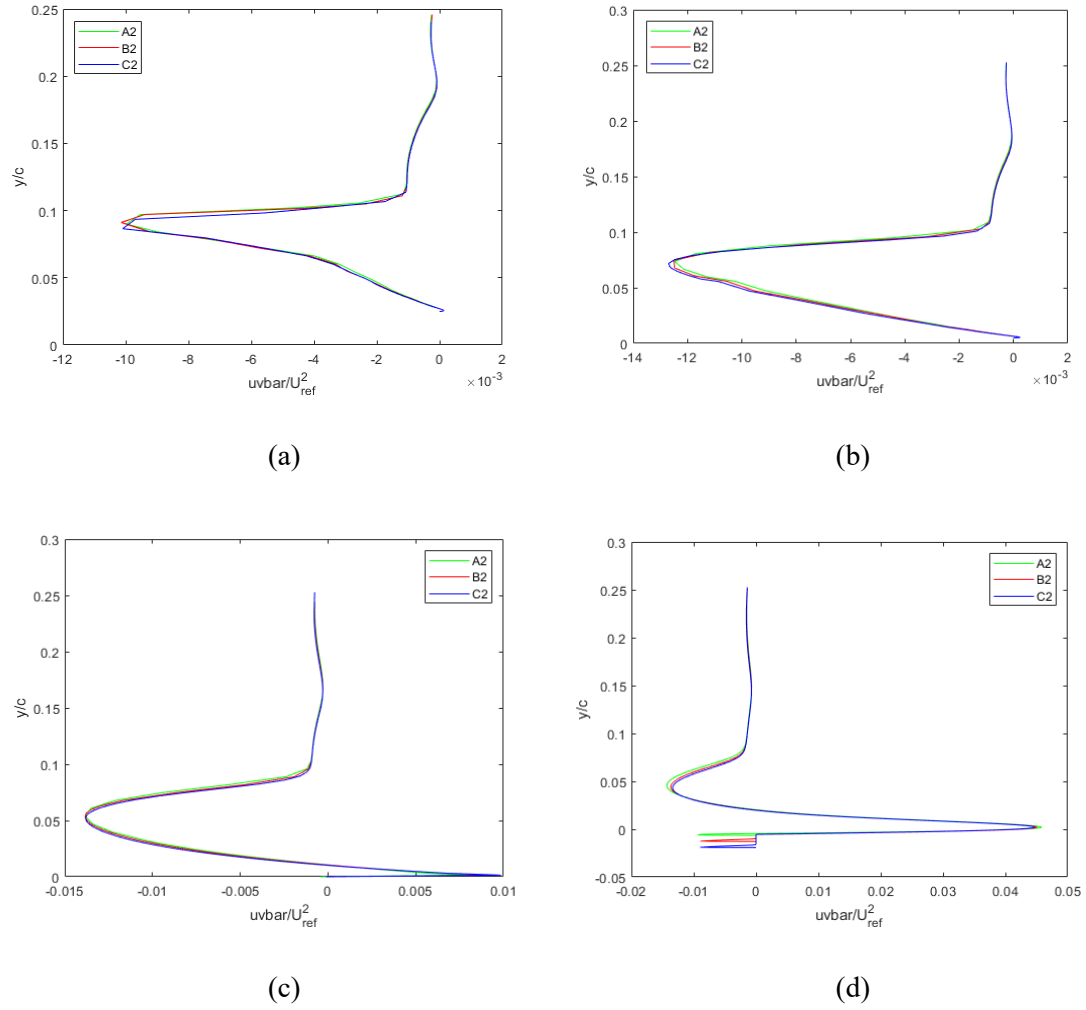

Figure A.12: Wall-Jet Hump-Wake Reynolds Stress Profiles Grouped by U_J/U_S for Cases A2, B2, & C2; (a) x/c=0.8, (b) x/c=0.9, (c) x/c=1.0, (d) x/c=1.1, (e) x/c=1.2, (f) x/c=1.3, (g) x/c=1.4, (h) x/c=1.5

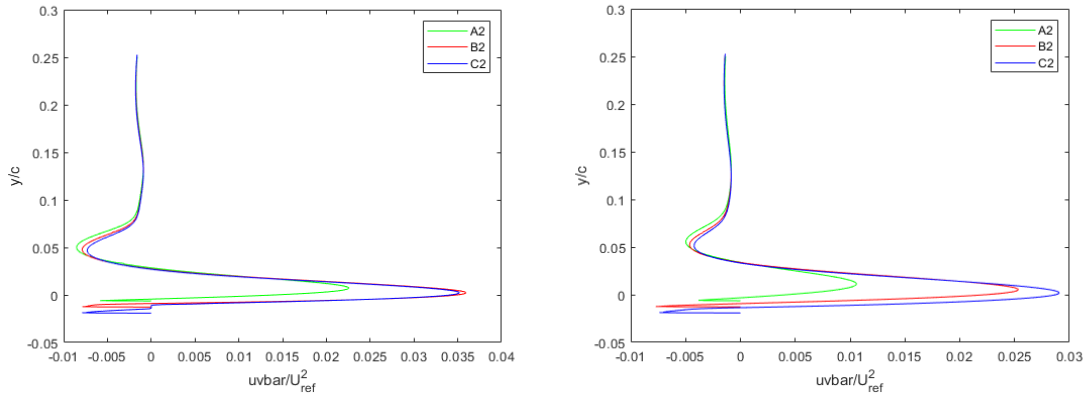

(e)

(f)

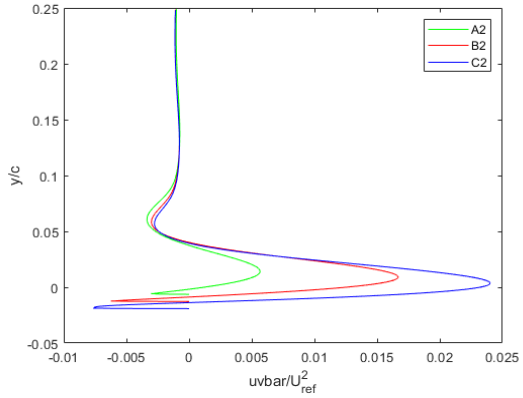

(g)

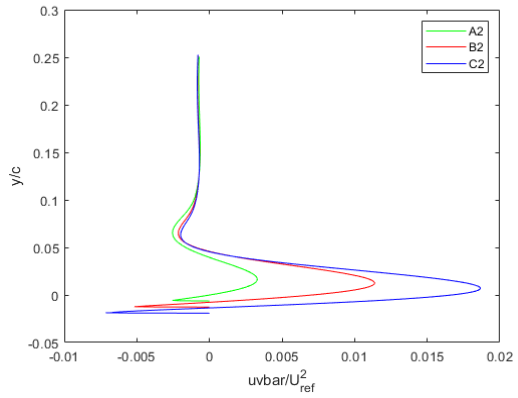

(h)

Figure A.12 (Continued): Wall-Jet Hump-Wake Reynolds Stress Profiles Grouped by U_J/U_S for Cases A2, B2, & C2; (a) x/c=0.8, (b) x/c=0.9, (c) x/c=1.0, (d) x/c=1.1, (e) x/c=1.2, (f) x/c=1.3, (g) x/c=1.4, (h) x/c=1.5

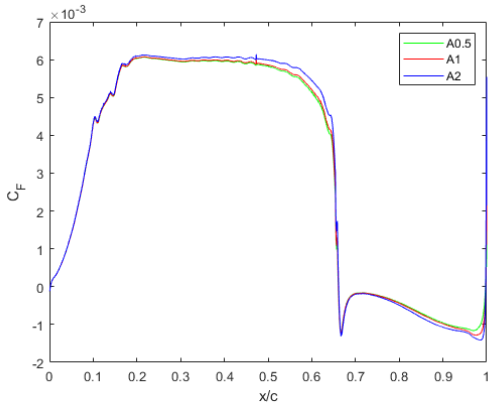

Figure A.13: Wall-Jet Hump-Wake Skin Friction Coefficient Across the Hump for Cases A0.5-A2

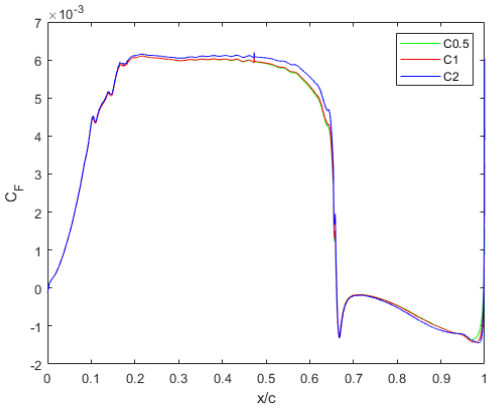

Figure A.14: Wall-Jet Hump-Wake Skin Friction Coefficient Across the Hump for Cases C0.5-C2

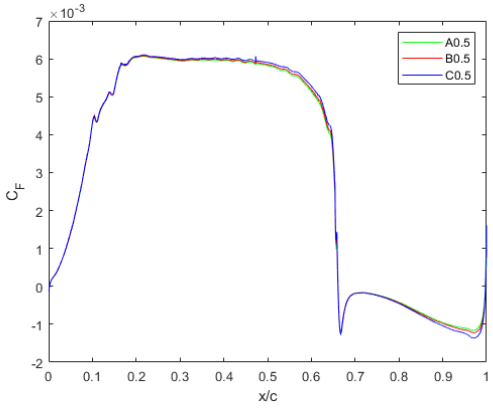

Figure A.15: Wall-Jet Hump-Wake Skin Friction Coefficient Across the Hump for Cases A0.5-C0.5

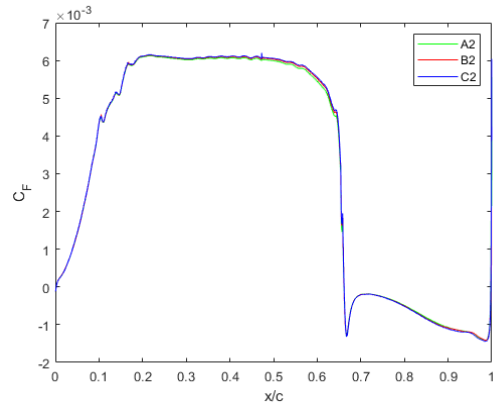

Figure A.16: Wall-Jet Hump-Wake Skin Friction Coefficient Across the Hump for Cases A2-C2

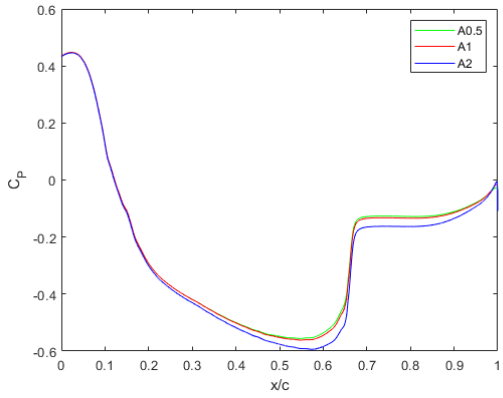

Figure A.17: Wall-Jet Hump-Wake Pressure Coefficient Across the Hump for Cases A0.5-A2

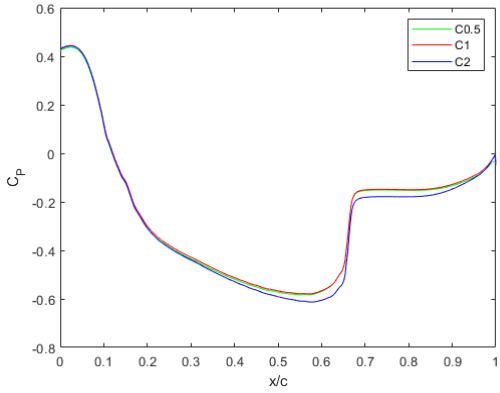

Figure A.18: Wall-Jet Hump-Wake Pressure Coefficient Across the Hump for Cases C0.5-C2

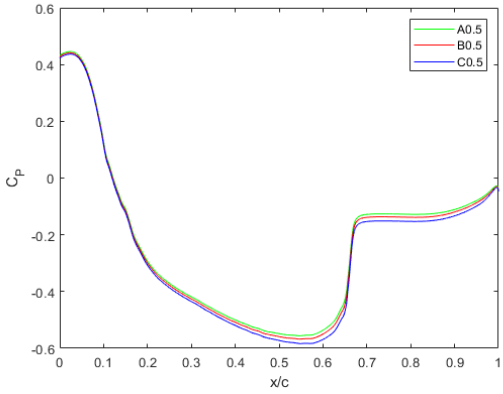

Figure A.19: Wall-Jet Hump-Wake Pressure Coefficient Across the Hump for Cases A0.5-C0.5

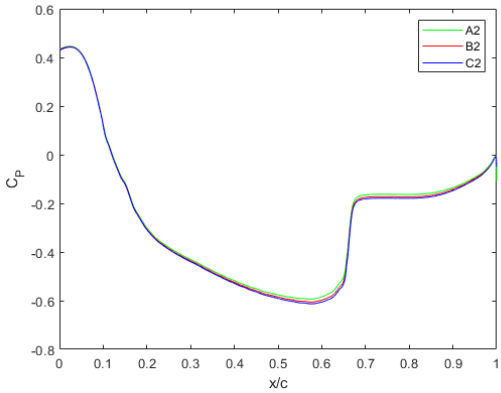

Figure A.20: Wall-Jet Hump-Wake Pressure Coefficient Across the Hump for Cases A2-C2

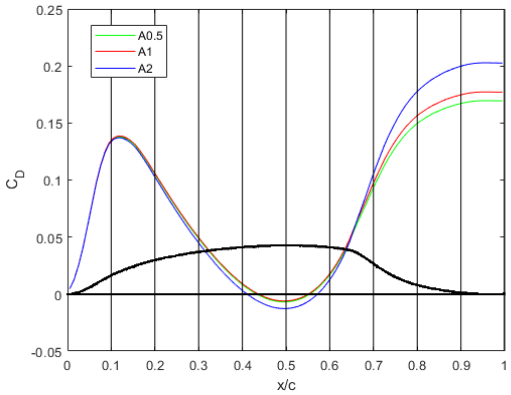

Figure A.21: Wall-Jet Hump-Wake Accumulated Drag Coefficient Across the Hump for Cases A0.5-A2

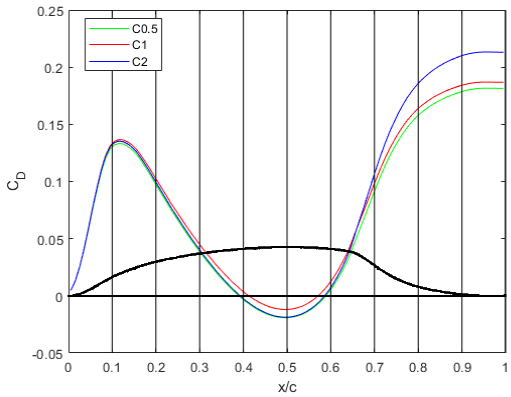

Figure A.22: Wall-Jet Hump-Wake Accumulated Drag Coefficient Across the Hump for Cases C0.5-C2

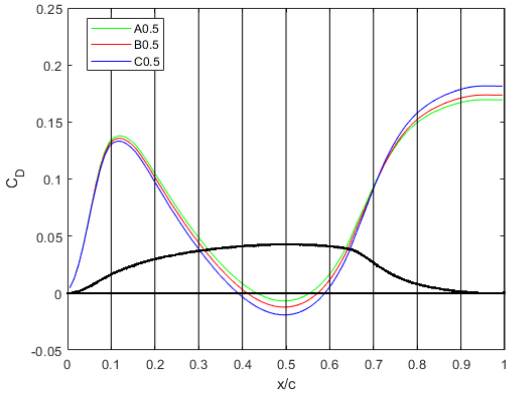

Figure A.23: Wall-Jet Hump-Wake Accumulated Drag Coefficient Across the Hump for Cases A0.5-C0.5

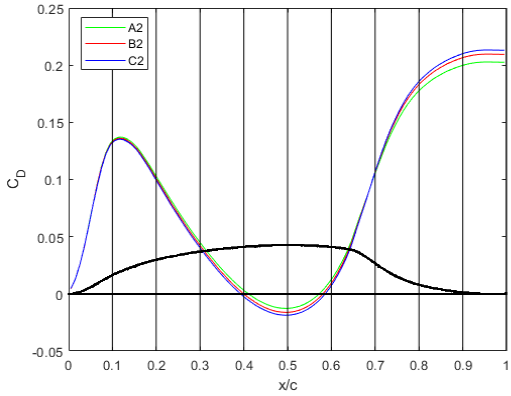

Figure A.24: Wall-Jet Hump-Wake Accumulated Drag Coefficient Across the Hump for Cases A2-C2